

**SCHRIFTENREIHE DES HZB · EXAMENSARBEITEN**

**Anomalous Small Angle X-ray  
Scattering (ASAXS) analysis  
of nanocrystals in glass  
ceramics: structure and  
composition**

Vikram Singh Raghuwanshi  
Dissertation

Abteilung Mikrostruktur- und Eigenspannungsanalyse

Juli 2012

HZB-B 35

### **Berichte des Helmholtz-Zentrums Berlin (HZB-Berichte)**

Das Helmholtz-Zentrum Berlin für Materialien und Energie gibt eine Serie von Berichten über Forschungs- und Entwicklungsergebnisse oder andere Aktivitäten des Zentrums heraus. Diese Berichte sind auf den Seiten des Zentrums elektronisch erhältlich. Alle Rechte an den Berichten liegen beim Zentrum außer das einfache Nutzungsrecht, das ein Bezieher mit dem Herunterladen erhält.

### **Reports of the Helmholtz Centre Berlin (HZB-Berichte)**

The Helmholtz Centre Berlin for Materials and Energy publishes a series of reports on its research and development or other activities. The reports may be retrieved from the web pages of HZB and used solely for scientific, non-commercial purposes of the downloader. All other rights stay with HZB.

ISSN 1868-5781

doi: <http://dx.doi.org/10.5442/d0029>

**Anomalous Small Angle X-ray Scattering (ASAXS)**  
**analysis of nanocrystals in glass ceramics:**  
**structure and composition**

**vorgelegt von**  
**Vikram Singh Raghuwanshi**  
**aus Bhopal (Indien)**

der Fakultät III-Prozesswissenschaften  
der Technischen Universität Berlin  
zur Erlangung des akademischen Grades  
Doktor der Naturwissenschaften  
-Dr. rer. nat.-

genehmigte Dissertation

Promotionsausschuss:

Vorsitzender: Prof. Dr. Walter Reimers  
Gutachter: Prof. Dr. John Banhart  
Gutachter: Prof. Dr. Klaus Rademann  
Gutachter: Prof. Dr. Christian Rüssel

Tag der wissenschaftlichen Aussprache: 31.5.2012



*Dedicated to:*

*All the relations to whom I am connected*



## **ABSTRACT**

The aim of the present work is a quantitative analysis of nanocrystallites with respect to their structures and compositions. This analysis will be done for all involved phases (crystalline and amorphous) of two different nanoglass ceramics by using anomalous small angle X-ray scattering (ASAXS) as a main method. Properties of glass ceramics depend on size, size distribution, volume fraction and on the composition of the formed nanocrystals and the remaining glass matrix.

Glass ceramics that contain nano-scale magnetic crystals showing special magnetic properties have many future applications. ASAXS investigations on these glass ceramics containing magnetic nanoparticles show the formation of a  $Mn_xFe_{3-x}O_4$  crystalline phase during heat treatment. The nanoparticles are surrounded by a thin layer enriched with  $SiO_2$ . Furthermore, the ratio of Fe and Mn atoms in the nanosized crystals is determined by ASAXS. The investigations show that the crystal composition changes from magnetite ( $Fe_3O_4$ ) towards the Jacobsite phase ( $MnFe_2O_4$ ) with increasing annealing time. SANS investigations with polarized neutrons prove the existence of spherical core-shell like structures. SANS also demonstrates that the nanoparticles are magnetic and the surface near region is magnetically disturbed. A so called magnetic dead layer is formed. Such a nanocrystal is surrounded by a nonmagnetic shell region.

Barium fluoride ( $BaF_2$ ) based nanocrystals doped with rare earth elements in silicate glasses are potential materials for various photonic applications such as optical amplifiers or fiber lasers. Energy filtering TEM studies imply that in glass ceramic containing nanosized crystals of  $BaF_2$  a shell like region surrounding the crystals exists that is enriched with  $SiO_2$ . ASAXS investigations on these samples confirm the formation of such layers enriched with  $SiO_2$ . Furthermore, these investigations provide quantitative information about the composition of the layer and the residual glass matrix and their temperature dependent composition changes.

In the present work, it will be shown how ASAXS combined with other investigation methods is able to provide quantitative information on structure and compositions of nanoparticles in multiphase systems. The two investigated glass ceramics belong to this group of multiphase systems.



## ZUSAMMENFASSUNG

Das Ziel der vorliegenden Arbeit ist eine quantitative Analyse von Nanokristallen in Bezug auf deren Struktur und Zusammensetzung. Diese Analyse wird von allen beteiligten Phasen (kristallin und amorph) von zwei verschiedenen Nano-Glaskeramiken mit Hilfe der anomalen Röntgenkleinwinkelstreuung (ASAXS) als wichtigste Methode durchgeführt. Die Eigenschaften der Glaskeramiken sind von der Größe, der Größenverteilung, der Volumenverteilung und der Zusammensetzung der gebildeten Nanokristalle sowie der restlichen Glasmatrix abhängig.

Glaskeramiken, die magnetische Kristalle im Nanometerbereich enthalten, und damit spezielle magnetische Eigenschaften haben, versprechen viele zukünftige Anwendungen. Die ASAXS-Untersuchungen dieser Glaskeramiken mit magnetischen Nanopartikeln weisen die Bildung einer kristallinen Phase ( $Mn_xFe_{3-x}O_4$ ) bei der Wärmebehandlung nach. Diese Nanopartikel sind durch eine dünne Schicht die mit  $SiO_2$  angereichert ist umgeben. Ferner wird das Verhältnis von Fe- zu Mn-Atomen in den nanometergroßen Kristallen durch ASAXS bestimmt. Die Untersuchungen zeigen, dass sich die Kristallstruktur ändert und die Zusammensetzung sich von Magnetit ( $Fe_3O_4$ ) in Richtung der Jacobsite Phase ( $MnFe_2O_4$ ) mit zunehmender Wärmebehandlungszeit ändert. SANS Untersuchungen mit polarisierten Neutronen weisen nach, dass sich eine Kern-Schale-Struktur gebildet hat, Weiterhin weist SANS nach, dass die Nanopartikel magnetisch sind sowie deren oberflächennahe Schicht magnetisch gestört ist, d.h. eine sogenannte dünne magnetische Totschicht wird ausgebildet. Umgeben ist solch ein Nanokristall von einer nichtmagnetischen Hüllenregion.

Nanokristalle, wie  $BaF_2$  in Silikat-Gläsern in Anwesenheit von seltenen Erden, sind potenzielle Materialien für verschiedene photonische Anwendungen wie optische Verstärker oder Faserlaser. TEM-Studien mit Energie-Filterung implizieren, dass in einer Glaskeramik, die nanometergroße Kristalle aus  $BaF_2$  enthält, sich eine Region rund um die Kristalle bildet, die mit  $SiO_2$  angereichert ist. ASAXS Untersuchungen an diesen Proben bestätigen die Bildung einer solchen Schicht, die mit  $SiO_2$  angereichert ist. Darüber hinaus bieten diese Untersuchungen quantitative Informationen über die Zusammensetzung der Hüllen-Schicht und der Restglasmatrix sowie deren temperaturabhängigen Zusammensetzungsänderungen.

In dieser Arbeit wird gezeigt wie ASAXS in Kombination mit anderen hier verwendeten Untersuchungsmethoden in der Lage ist, quantitative Informationen über Struktur und Zusammensetzung von Nanopartikeln in mehrphasigen Systemen zu liefern. Die beiden hier untersuchten Glaskeramiken gehören zu diesen mehrphasigen Systemen.



# TABLE OF CONTENTS

<i>Abstract</i>	I
<i>Zusammenfassung</i>	III
<b>1. Introduction</b>	<b>1</b>
1.1 Motivation	1
1.2 Objective	3
<b>2. Glass and Ceramics</b>	<b>5</b>
2.1 Introduction to glass-ceramics	5
2.2 Importance of glass-ceramics	5
2.3 Properties of glass-ceramics	6
2.4 Preparation of inorganic glass	9
2.5 Thermodynamics of glass	11
2.6 Nucleation of glass	13
<b>3. Small Angle Scattering</b>	<b>17</b>
3.1 Scattering	17
3.2 Small Angle X-ray Scattering (SAXS)	20
3.3 Anomalous Small Angle X-ray Scattering (ASAXS)	25
3.4 Energy dependent scattering contrast	27
3.5 Small Angle Neutron Scattering (SANS)	29
3.6 Polarized Small Angle Neutron Scattering (polarized SANS)	32
<b>4. Experimental</b>	<b>35</b>
4.1 SAXS and ASAXS at BESSY II	35
4.1.1 Beamline description	35
4.1.2 Data reduction/SASREDTOOL	38
4.2 SANS at ILL	41
4.2.1 Description of the beamline D22	41
4.2.2 Data reduction/GRASP	42
<b>5. Crystallization of magnetic <math>Mn_xFe_{3-x}O_4</math> nanocrystals in silicate glasses</b>	<b>43</b>
5.1 Motivation	43
5.2 Glass preparation	44
5.3 Sample characterization using electron microscopy and X-ray diffraction	45
5.4 SAXS study of heat treated sample series	50
5.5 Investigation of magnetic nanostructure using polarized SANS	56

5.6	ASAXS study at the absorption edge of Fe and Mn	64
5.7	Kinetics of phase formation as studied in situ	70
5.8	Discussion of the formation of magnetic nanoparticles	75
<b>6.</b>	<b>BaF<sub>2</sub> nanocrystals formation in transparent glass ceramics</b>	<b>77</b>
6.1	Motivation	77
6.2	Glass preparation	78
6.3	Sample Characterization	79
6.4	SAXS Results	83
6.5	ASAXS studies	86
6.6	Discussion of the structure model of BaF <sub>2</sub>	92
<b>7.</b>	<b>Summary and Outlook</b>	<b>95</b>
	<i>Appendix</i>	97
	<i>References</i>	99
	<i>Abbreviations</i>	107
	<i>Publications</i>	109
	<i>Acknowledgement</i>	111
	<i>Declaration</i>	113

# 1. Introduction

## 1.1 Motivation

Glasses play a vital role in the progress of society. They are used in various fields of daily life and play an important role for the industry. Applications of glasses are very wide and different. Therefore, different glasses have to fulfil a variety of different properties. As an example, window glasses should be transparent and thermal isolating. Glass is defined as an amorphous solid lacking of long range periodic atomic structure. A glass has a region of glass transformation behaviour and gradually softens to a molten state on heating [1]. The properties of glasses and glass ceramics are determined by their chemical composition and also by nanophases that could be formed. The development of such nanosized heterogeneities is influenced by the tendency of glasses to undergo a crystallization or segregation process. Such processes can often be influenced by definite temperature treatments. The phase separated glasses will be named as glass ceramics if at least the separated phase is crystalline. Nanoglass ceramics can have superior properties such as high mechanical strength and impact resistance but they can have also outstanding functionality. In particular, so called ultratransparent glass-ceramics containing metal fluoride nanocrystals sized between 5 and 100nm possess a huge application potential since rare-earth-doped metal fluoride nanocrystals feature significantly enhanced optical fluorescence, luminescence and upconversion [2-6]. Nanoglass ceramics containing nanosized magnetite or bariumhexaferrite crystals feature interesting magnetic properties because the crystals are well dispersed in the glass matrix and the magnetism (superparamagnetic or ferrimagnetic) depends on their sizes and on the application temperature.

Nowadays, strong research efforts are going on to develop new glass ceramics featuring new properties. Therefore methods to investigate such nanostructures are necessary. The electron microscopy method is an often used direct method that gives local pictures out of small volumes. Moreover, small angle scattering methods (SAS) allow analysing particle sizes, size distributions and volume fractions. This method is a non-destructive integral averaging analytical method that gives averaged structural parameters out of the whole sample volume the beam penetrates. Therefore the method gives structural parameters with a high statistical significance because the method averages usually over more than  $10^{14}$  nanosized objects.

The properties of nanostructured materials are depending on the chemical composition of the components and not only on their size shape and distribution. The compositions of nanophases can be determined with local non-destructive methods like energy dispersive X-ray spectroscopy (EDX) or with energy filtering TEM. An advantage of these methods is that the data evaluation and interpretation is relative fast and easy. But it can happen in case of nanosized objects that the signal contains in parts the environment so that the composition analyses are often cannot be quantitative.

The only method that allows obtaining an integral averaged composition analysis of nanosized structures is the anomalous small angle X-ray scattering (ASAXS) method. The method employs the anomalous dispersions of the atomic scattering amplitude near the absorption edge of an element containing in the sample. This anomalous dispersion effect results in a definite variation of the scattering contrasts and allows analysing composition fluctuations between nanosized structures.

Small angle neutron scattering with polarized neutrons (SANS) is an outstanding method that allows characterizing and distinguishing magnetic nanostructures from nonmagnetic structures [7, 8]. SANS with polarized neutrons is a method of choice if the nanostructure of magnetic nanoparticles have to be analysed. Their composition analysis requires the application of ASAXS.

In the frame of this work the structure and chemical composition of two glass ceramics will be analysed quantitatively. First a nanosized magnetic phase containing glass ceramics will be investigated. It is known up to now by using microscopic methods (SEM, TEM) and by diffraction (XRD) that the particles are spherical in shape and they contain of a mixed phase of Iron and Manganese oxides [9]. It is up to now not clarified, which are the ratio of Fe and Mn in the magnetic crystal. Will be this Fe to Mn ratio changes during the growth process? Furthermore, it is not clear whether a shell like region will be formed surrounding the particle or not?

Second a transparent silicate glass ceramic system containing the BaF<sub>2</sub> nanoparticle is chosen [10]. This transparent glass ceramic is usable for photonic application. It was observed that the nanocrystal growth inhibited by a mechanism that could not explained by the known theories of growth and ripening [11]. Energy filtering TEM investigations revealed a SiO<sub>2</sub> enriched shell is formed that surrounds the particles and acts as barrier for further crystal growth [12]. It is not quantitative known how the shell is composed and also the size distribution of the formed BaF<sub>2</sub> crystals has to be investigated.

## 1.2 Objective

In the frame of this work the structural parameters (shape, size and volume fraction) of the nanoparticles and its compositions of two different glass ceramics should be determined quantitatively by anomalous small angle X-ray scattering.

Firstly, magnetic nanoparticles embedded in a glass ceramic of composition  $13.6\text{Na}_2\text{O}-62.9\text{SiO}_2-8.5\text{MnO}-15.0\text{Fe}_2\text{O}_{3-x}$  and secondly, a  $\text{BaF}_2$  nanoparticle containing transparent glass ceramic of composition  $69.6\text{SiO}_2-15.0\text{K}_2\text{O}-7.5\text{Al}_2\text{O}_3-1.9\text{Na}_2\text{O}-4\text{BaF}_2-2\text{BaO}$  have been chosen for this purpose. In both glass ceramics, the formation of nanocrystals will take place during annealing.

The main objective in case of the magnetic glass ceramic is to clarify, whether a core shell like structure is formed. ASAXS combined with SANS (polarized neutrons) can help to decide the structural model and to determine the structure of magnetic nanoparticles. The objective also includes obtaining quantitatively the composition of other existing amorphous phases (shell regions) and the residual glass matrix. In case of the  $\text{BaF}_2$  crystal forming glass ceramic the growth stop and its structural reason will be studied by ASAXS. The common aim in both materials is to analyze the nanostructures in multiphase systems.



## 2. Glass and Ceramics

### 2.1 Introduction to glass-ceramics

Glass-ceramics have a huge contribution in the growth of civilization, because of its properties like transparency, lustre (or shine), and durability [1]. They are hard, brittle, and stand up against the environment conditions such as effects of wind, rain or sun. Glass and ceramics are widely used for making household utensils and also having other industrial applications. The origin of the word *glass* is the Latin term *glasum* used to refer to a lustrous and transparent or translucent body. Glassy substances are also called *vitreous*, originating from the word *vitrum*, again denoting a clear, transparent body. Glass is known to be a non-crystalline material, has no long-range order of positioning of its molecules and they exhibits glass transition when heated towards the liquid state [13-16]. Glass-ceramics are materials formed by crystallization of base glass. Glass does not have a sharp melting point like a crystal and they soften and flow at higher temperatures. Any material, like inorganic, organic or metallic formed by any technique and which exhibits glass transformation behaviour is termed as a glass.

### 2.2 Importance of glass-ceramics

Most of the glass-ceramics are hard, chemically inert, transparent, refractory and poor conductors of heat and electricity, which makes them suitable for many applications [17,18]. Nowadays, glass-ceramics can be tailored to meet an exact need of applications. Machinery has been developed for precise, continuous manufacture of glass sheet, tubing, containers, and a host of other products [13]. Glass and ceramics are used in beverage containers, window panes, automobile, windshields, pipelines, cookware, building blocks, heat insulation, telephone poles, electronic devices, and the nose cones of spacecraft [19,20]. The major disadvantage of glass-ceramics is their brittle nature, which acquire tiny cracks and results in breakage of materials. Glass-ceramics materials such as barium ferrite or nickel zinc ferrites are used in manufacturing stronger magnetic field magnets, which are less weighted and cost efficient. Some glass-ceramics such as lanthanum zirconate titanate have electro-optic properties, which mean variation in transmitting light by applying variable voltages, which is useful for memory-storage devices [17,18].

In the 1970's, optical fibers were developed for use as "light pipes" in laser communication systems [21]. These pipes maintain the brightness and intensity of light being transmitted over long distances. Glass fibers are the extremely fine fibers, which are made up of glass materials. The glass fibers are so small (typically diameter 100 $\mu$ m) that more of them fit into a cable of a given sizes. The glass fibers are not susceptible to electromagnetic interference, so the signal is clearer [16,22]. Finally, the information carried on optical fibers can be modulated at very high frequencies, so many more simultaneous transmissions, e.g. telephone conversations are possible. Communication by light rather than electricity required the development of suitable light sources as well as extremely pure, ultra transparent glass fibers.

Glass-ceramics also have importance in field of medicine, e.g. used in fabricating artificial bones and crowns for the damaged teeth and many other medical applications [23-26]. Glass-ceramics of certain kinds are also used as materials for storing radioactive wastes for long times [27].

### 2.3 Properties of glass-ceramics

Applications of glass-ceramics in different fields, depends on various properties of glasses such as mechanical, chemical, optical, thermal, electrical and magnetic properties. The properties of glass-ceramics can be tailored by modifying the compositions and fabrication techniques. Some of the important properties of glass-ceramics are discussed below.

#### *Mechanical Properties*

In glass-ceramics, the atomic arrangements are more or less random. Hence, the physical properties of glass-ceramics are, in general, isotropic like those of liquids. Like glass and ceramics, glass-ceramics are brittle materials that exhibit elastic behaviour up to the strain that causes fracture [28]. Due to the formations of crystalline microstructures in glass-ceramics, they have higher strength, toughness, abrasion and elasticity. Plastic deformation may occur at extremely high-point loading and involves a considerable amount of bond bending rather than the large-scale dislocation motion or grain boundary sliding.

#### *Viscosity*

Viscosity is a property of the liquid state, which describe its flow due to externally applied stresses. Viscosity is the reciprocal of fluidity and it is inversely proportional to the

temperature. Viscosity of glass-ceramics increases with network connectivity. Dependence of the viscosity on temperature plays an important role in determining, how easily a product is formed for any melt. When the viscosity is high at the melting temperature of crystalline phase and increases rapidly with decreasing temperature, in both cases glasses are formed easily. Determination of viscosity helps in forming bubble-free, homogenous, stress free glass-ceramic used to form commercial applications.

#### *Thermal properties*

Many commercial glass-ceramics have importance due to their thermal properties such as low thermal expansion coupled with high thermal stability and thermal shock resistance. When heat is given to a body, thermal expansion shows the relative change in a given dimensions of body. Thermal expansion is important in determining the suitability of using a variety of materials particularly involving a glass-ceramic in a restrained condition. When glass-ceramic components are suddenly goes to a rapid temperature change, due to there low thermal conductivity tensile stress leads to glass fracture. The resistance to sudden temperature change is called ***thermal shock resistance*** or ***thermal endurance***. This property is determined primarily by the thermal expansion coefficient and the thickness dimension of the product in the direction of the heat flow. The expansion and the contraction due to thermal energy is an important consideration for product design [29,31].

#### *Electrical Properties*

Electrical properties of glass-ceramics are important for their applications in electrical and electronic industries. A substance is electrically conducting when free electrons or ions within it flow on applying electrical potential. Since the ionic motion is the dominant diffusion phenomenon in glass-ceramics, ions are responsible for the charge carriers. Electronic conduction is possible in the glass-ceramics, which contain transition metals such as Fe, Mn and V displaying multivalency. Electronic conduction is predominant in elemental glasses, such as silicon, germanium, and the chalcogenides, where it is responsible for the semiconductor properties, and suitable for the modern electronic industries [32,33]. In general, glass-ceramics have such a high resistivity that they are used as insulators. The dielectric properties of glass-ceramics are depending on the nature of crystal phase and on the amount and composition of the residual glass [28]. The homogeneous, grained character of glass-ceramics leads high dielectric breakthrough strengths, and can be used as high voltage insulators or condensers.

### *Chemical Properties*

The chemical durability of glass-ceramics is depending on the crystals and the residual glass. Due the chemical durability glass-ceramics are preferred materials in variety of applications such as window glasses, in chemical laboratory etc. In spite of this, acids and alkali solution attack glass in different way. Hydrofluoric acid affects any type of silicate glass, while other acids attack only slightly. Water corrosion acts at slower rate in normal environment but at high temperatures, water corrosion can be significant. Glass-ceramics having low alkali residual glasses, such as b-quartz and b-spodumene, have excellent chemical durability and corrosion resistance [28].

### *Magnetic Properties*

There are wide ranges of magnetic glass-ceramic materials which exhibit ferromagnetism, ferrimagnetism or superparamagnetism behaviour. Glass-ceramic magnets are usually composed by transition metals doping, they have applications in making inductors, speaker magnets, magnetic resonance imaging (MRI) etc. Ferrite is generally a used term for the whole range of such magnetic materials. Many glass-ceramics compounds containing transition metals are crystallize in spinel structure or inverse spinel structure, which are associated with the magnetic behavior [34].

### *Optical Properties*

Nowadays, optical properties of glass-ceramic are of interest in field of science and in the industrial applications. The properties of glass-ceramic include refraction, reflection and transmission of light and also the dependency of the wavelength to those properties. Transparency (or *absorption* as its inverse) is one of the most important properties of glass for its application. When light passes through the glass-ceramic (wide band gap) insulator, the energy of light is not sufficient to excite the electronic energy states and not being absorbed by them. Transparency of material depends on the crystal size, size distribution, refractive index between crystals and glass matrix. Excellent transparency can be achieved, when the size of the crystals are not of the order of the wavelength of the light. Dispersion characterizes how the refractive index of a particular glass varies with wavelength. This is clearly an important specification for optical glasses. When the wavelength of light is absorbs and creates an electronic transition in the visible spectrum range in the electronic states, due to which the glass appeared colored.

## 2.4 Preparation of inorganic glass

Inorganic glasses are the materials which are formed by fusion of inorganic compounds such as silicates, potassium, sodium, calcium and other inorganic oxides. Manufacturing of inorganic glass requires three major components; *Network former*, *Intermediates* and *Modifiers*.

The major component in formation of any glass is the network former which serves as a primary source for the glass structure. These components are generally termed as glass formers, or glass forming oxides in many oxide glasses. Mainly, the network formers such as Si, Ge have an ability to form a highly cross-linked network of chemical bonds. The network former serves as the basis for the generic name used for the glass. For example in the glass where the network former is silica is called as silicate glass, when boric oxide and silica are acts a network former then glasses are termed as borosilicate glasses. The major glass former are silica ( $\text{SiO}_4$ ), boric oxide ( $\text{B}_2\text{O}_3$ ) and phosphoric oxide ( $\text{P}_2\text{O}_5$ ) [1]. Intermediates are those materials used in formation of glass which acts as both network formers and modifiers. For example titanium, aluminium, zirconium, beryllium, magnesium, zinc etc are generally used as an intermediate. Some compounds such as alumina, which acts a network former in aluminates glasses and also it acts as a property modifiers in many silicate glasses [1].

Adding certain materials during glass formation which alter the network structure or the properties of glasses are termed as glass modifiers or property modifiers. There are compounds that have tendency to donate anions to the network, and the cations occupy “holes” in the disordered structure. These conditions cause the formation of nonbridging anions, or anions that are connected to only one network-forming cation [32]. Modifiers generally have cations with low charge-to-radius ratios ( $Z/r$ ), for example alkali or alkaline-earth ions. Colorants and fining agents are used to control the color of the final glass and to promote the removal of bubbles from the melt.

According to Zachariasen, [18] glass is a substance which can form extended three dimensional networks lacking periodicity with an energy content comparable with that of the corresponding crystal network. From these conditions, Zachariasen suggested four rules for selecting the oxides  $\text{A}_m\text{O}_n$ , that tend to form glasses. The rules are follows as:

1. The oxygen is linked to no more than two atoms of A.
2. Coordination of the oxygen about A is small: 3 or 4.
3. Oxygen polyhedra share corners, and not edges or faces.
4. At least three corners are shared.

The main rule in formation of glasses is a distribution of M–A–M angles, where M is a cation and A is an anion. Silicates are one of the most important constituents of glasses. Rigid silicon oxygen tetrahedron structure is the main building blocks for both amorphous and crystalline phase of silicates in glass-ceramics, where Si and O both are present in the three dimensional tetrahedral network. Both crystalline and vitreous  $\text{SiO}_2$  are shown in Figure 2.1 [18,36] where Si is tetrahedrally bonded to oxygen, the fourth oxygen being out of the plane of paper. Whereas the local oxygen coordination is almost the same as that in a corresponding crystalline solid, the intermediate range order described by ring structures clearly differs considerably between the crystalline and the glassy forms. The glass network consists of holes that are larger than those in the crystal. Direct evidence of such kind of network of a thin silicate glass is reported [37]. The structure of amorphous silica is quite uniform at atomic distances, although there is no order beyond several layers of tetrahedral.

In silica glasses containing alkali and alkaline earth oxides, these cations apparently are not randomly distributed throughout the glass; their average separation is less than from a uniform distribution. It is possible that alkali ions form in sheets, as in certain crystalline alkali silicates.

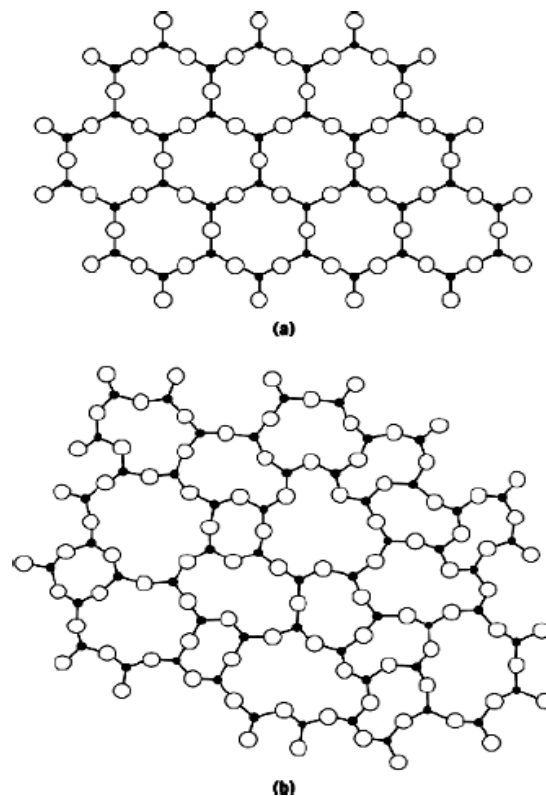


**Figure 2.1:** (a) Crystalline state of  $\text{SiO}_2$  (b) Amorphous state of  $\text{SiO}_2$  [18].

The network can be partially broken by other oxides like alkali and alkaline earth oxides, termed as network modifiers. When a compound such as  $\text{Na}_2\text{O}$  is introduced in silica, the

arrangement of atoms in a two-dimensional plane is shown in Figure 2.2. Those oxygen, which connect two silicon tetrahedra at corners, are called *bridging oxygens* (BOs). Some oxygen atoms are linked to only one silicon atom; which are called the *nonbridging oxygen* (NBOs). Since oxygen is a bivalent ion, its connection to only one silicon ion leaves one negative charge, which is satisfied by a univalent positive sodium ion in the interstitial spaces.

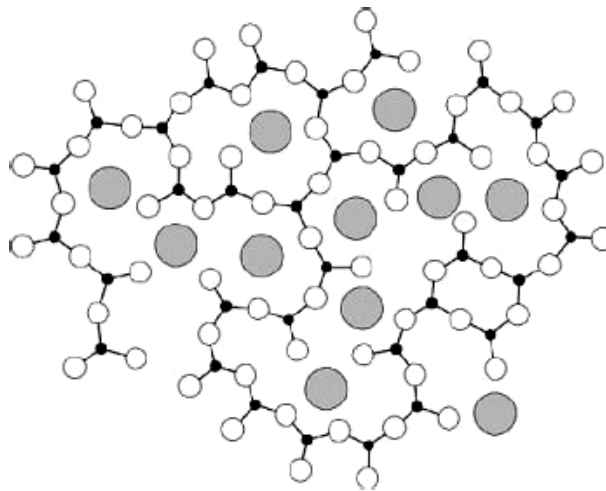


**Figure 2.2:**  $\text{Na}_2\text{O}$  is introduced in silica, the arrangement of atoms in a two-dimensional plane. The big gray filled circles are the Na atoms and the small black circles are the Si atoms and the white circles are the oxygen atoms [18].

## 2.5 Thermodynamics of glass

Numerous investigations have been done to understand the basic thermodynamics and kinetics of formation of glasses [38-40]. The thermodynamics of glass transformation behavior can be understood on the basis of changing the volume with respect to temperature. Figure 2.3 shows the curve for the change in the volume of a material with temperature.

In the Figure 2.3, point **a** is the small volume of a liquid at the temperature well above the melting temperature of that substance. Atoms were arranged differently as the substance is cooled differently below the melting temperature. When the substance is cooled below point **a** then the volume shrinks along the line **ab**. The temperature at point **b** is the thermodynamic melting point of crystals of same composition, slightly below this point there is high probability of long range periodic arrangements of atoms to form crystalline structures. Crystallization is possible only when there is a sufficient nucleation rate followed by significant crystal growth.

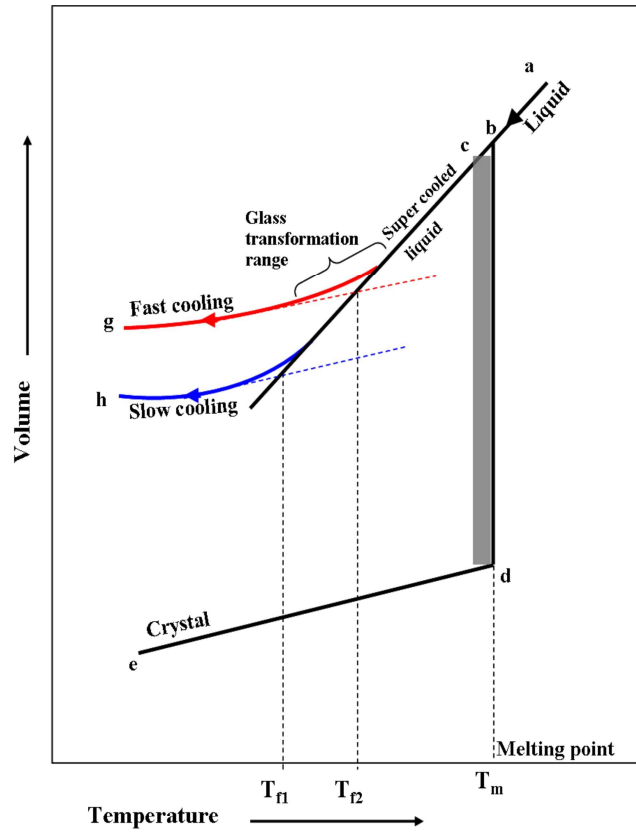


Figure 2.3: The volume-temperature diagram [34].

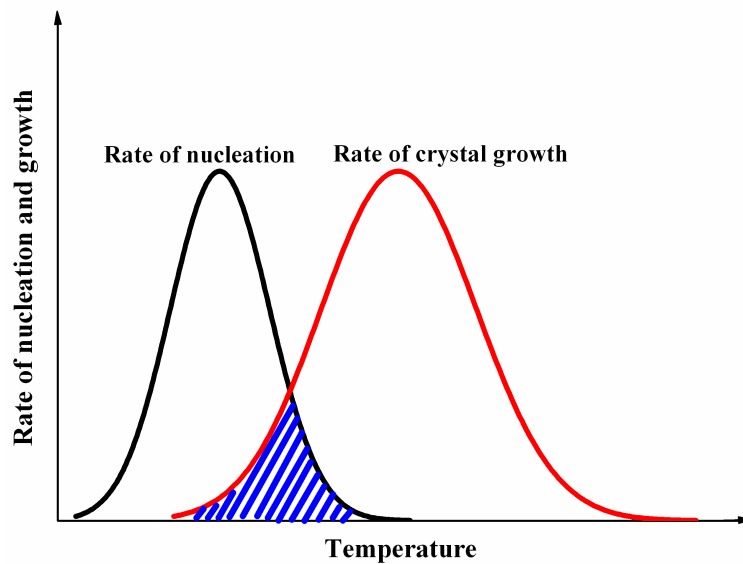


Figure 2.4: Schematic of nucleation and crystal growth rates as a function of temperature.

Figure 2.4 shows the dependency of nucleation rate and crystal growth with temperature. The shaded area in Figure 2.4 reveals the temperature range for the crystallization, which resembles with the shaded line in Figure 2.3. Point *c* has the highest probability of crystal formations. In this range of *b-c* the volume of the substance drop discontinuously without any

change in temperature is called as thermodynamically first order transition. For further decrease of temperature, the volume decreases as followed by the slope *d-e*. In Figure 2.4, when there is no overlap in nucleation rate with the crystal growth, then the volume of a substance decreases by following the supercooled state and remain liquid below its melting point because there are no nucleation sites to initiate the crystallization.

Further cooling leads to increase in viscosity of the substance. Below super cooled state the volume decreases exponentially by following the slope c-g or c-h depending on the cooling rate. In this range the substance now appears as a solid. In this region the molecules have a disordered arrangement, but sufficient cohesion to maintain some rigidity. In this state it is often called an amorphous solid or glass. There is a beginning of the glassy state below the supercooled state. Volume is higher for the faster cooling and lower for the slow cooling as shown in Figure 2.3. The transition between the supercooled and glassy state do not occur rather at sharp temperature, but smoothly over a temperature range. Such type of continuous transition is like a thermodynamic second order transition. This range of temperature is called the glass transformation range. The glass transition temperature  $T_g$  in the transformation range at the intersection of the glass line with a tangent to the steepest portion of the transition curve. However,  $T_g$  is a useful indicator of the approximate temperature where the super cooled liquid converts to a solid on cooling or conversely, of which the solid begins to behave as a viscoelastic solid on heating. Thus, the glass transition range is characterized as the region of temperatures where the structure of the mass is continuously relaxing to greater equilibrium. The temperature  $T_f$  between the supercooled liquid and glass state is called as fictive temperature. This temperature may be assumed as a point where the liquid is instantly frozen into the solid glass. This approximation says that the structure of liquid relaxes rapidly at first, and with increase of viscosity this relaxation rate slows down with the temperature.

## 2.6 Nucleation of glass

In glass, crystallization is a process of forming crystalline structures in glass matrix. For crystallization process, it requires a crystal nucleation followed by the crystal growth as discussed in section 2.5. Formation of nano or micro size crystalline phases in glass ceramics may change drastically the properties of materials. Therefore in glass ceramics, many properties can be optimizing by choosing base glass with suitable compositions and by controlling crystal nucleation and growth process [41].

Formation of crystals in glasses primarily requires the formation of tiny nucleus or embryo of the new phase which is termed as nucleation process and the specific temperature at which the crystal nuclei are form is called as crystal nucleation temperature. Nucleation is the important factor for controlling crystallization in glass ceramics. When the glass is held at its crystal nucleation temperature, multiple crystal seeds are formed and starts to grow slowly. For the better quality of material, requires crystals of small sizes and its uniform distribution in the glass matrix. Classical nucleation theory can describe the nucleation and crystallization in glass ceramics [42-44]. According to the classical theory, the difference between the free energy of the crystal and the remaining glass  $\Delta G$  acts as a driving force for the transformation of glass to a crystal via nucleation and growth process. During the process of nucleation and growth an interface between crystal and glass matrix and the energy associated with the interface is termed as a surface free energy. As the crystal grows, the total surface free energy increases. During the homogenous nucleation process the energy minimization involves two terms: **Volume transition** and **Surface formation**.

The volume transition term for a spherical shape nucleation of radius  $r$  is given as:

$$\Delta G_1 = \frac{4}{3} \pi r^3 \Delta G_{vol} \quad (2.1)$$

where  $\Delta G_{vol}$  is the change in free energy per unit volume.  $\Delta G_1$  is a negative term, which provides a driving force for nucleation. The surface formation energy is given by:

$$\Delta G_{surf} = 4\pi r^2 \gamma \quad (2.2)$$

where  $\gamma$  the surface energy per unit area. The change in surface energy is always positive when forming surfaces. So the total change in the energy is the sum of volume and surface free energy term and given as:

$$\Delta G = \frac{4}{3} \pi r^3 \Delta G_{vol} + 4\pi r^2 \gamma \quad (2.3)$$

The variation of the above equation with the radius of the spherical particle is shown in Figure 2.5. In the Figure, the different energy contribution yields an increase in the total free energy up to a certain radius called as  $r_c$  is the critical radius for the nuclei and after that, the total free energy starts to decrease. The variation of total energy upto the critical radius is due to decrease of surface to volume ratio with increasing radius. After reaching the critical radius, the negative volume free energy dominates the positive surface free energy and the total free energy starts to decrease.

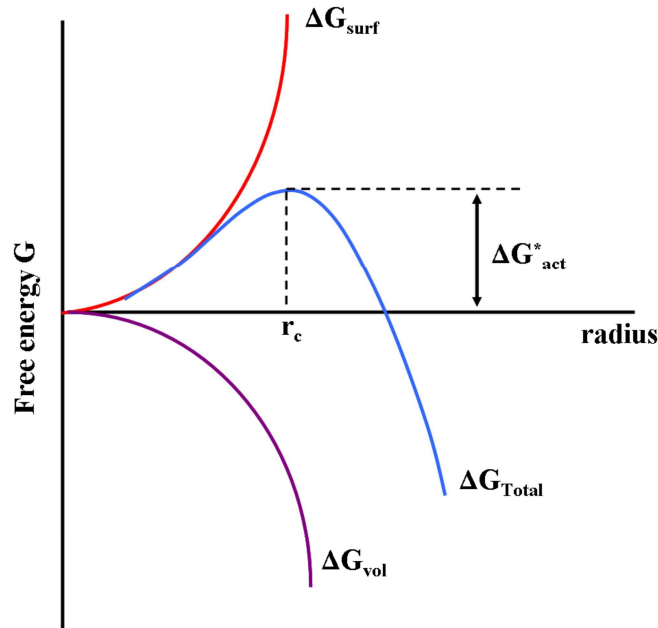


**Figure 2.5:** Change in Gibbs free energy with radius of particles in nucleation and growth process.

The value of critical radius can be calculated by taking the derivative of the total free energy in equation (2.3) as  $\frac{d\Delta G}{dr} = 0$  at  $r=r^*$  and this evaluation gives the critical radius values as:

$$r^* = -\frac{2\gamma}{\Delta G_{vol}} \quad (2.4)$$

By putting  $r^*$  in equation (2.3) it is possible to evaluate the activation energy for nucleation as:

$$\Delta G_{act}^* = \frac{16\pi\gamma^3}{3(\Delta G_{vol})^2} \quad (2.5)$$

As the nuclei grow larger, the free energy reaches a maximum and become negative and leaving stable nuclei. Both nucleation and growth process dependent on viscosity and the free energy change. At the initial process of nucleation, many small crystallites are form, but slowly they disappear and remain only the big crystallites due to which the area around the bigger crystal depleted of the smaller crystallites. The smaller crystallites have higher solubility than the bigger crystallites, as results larger crystallites are more energetically favorable than the smaller crystallites. This process is terms as **Ostwald ripening**. In this process, the small crystallites are kinetically favored because they nucleate easily and the larger crystals are thermodynamically favored.



## 3 Small Angle Scattering

### 3.1 Scattering

Scattering is a phenomenon that occurs when the trajectory of moving object or radiation (light, sound) deviates from a straight line due to interaction with some other objects. In science scattering theory is the study of the scattering of waves and particles. In any technique that uses radiation, scattering and absorption are the first processes that take place while interacting with matter. In microscopic techniques, a small part of the sample is illuminated by electromagnetic radiation or particles beam, which interacts with the sample and the consequent collection of scattered photons or particles and its phase relation are used to create an image. In other scattering techniques such as XRD, SAXS, SANS etc. a whole illuminated sample volume is investigated. Neutron and synchrotron X-rays has their wavelengths in angstroms scale, which makes them a suitable tool for structure analysis, especially on different length scales from the atomic scale to micron scale. Also due to the neutrality of neutrons and the high energy of synchrotron X-rays, they can transmit through bulky materials, enables to investigate the properties of the system as a bulk.

When an electromagnetic wave interacts with a matter, then depending on the energy of wave, matter composition and thickness of the material, a fraction of photons will transmitted, absorbed, scattered or transformed in other form of energies. Let us consider an electromagnetic wave of intensity  $I_0$  is incident on the sample of thickness  $t$ , density  $\rho$  and the linear absorption coefficient  $\mu$ , which combines with the density and makes mass absorption coefficient ( $\mu/\rho$ ). Depending on the energy and material the values of mass absorption is tabulated [45] and  $I$  is the resultant intensity of the wave after attenuation of incident wave  $I_0$ . Figure 3.1 shows the schematic profile of the propagation of electromagnetic wave through matter. The formula that described the above attenuation of X-rays is defined as:

$$I = I_0 e^{(-\mu d)} \quad (3.1)$$

The number of photons transmitted through the matter depends on the thickness, density and atomic number of the material and the energy of the individual photons. From the above equation (3.1) transmission ( $T$ ) or absorption ( $A$ ) can be calculated, which is defined as a ratio of transmitted wave over the incident wave as:

$$Transmission = \frac{1}{Absorption} = \frac{I}{I_0} \quad (3.2)$$

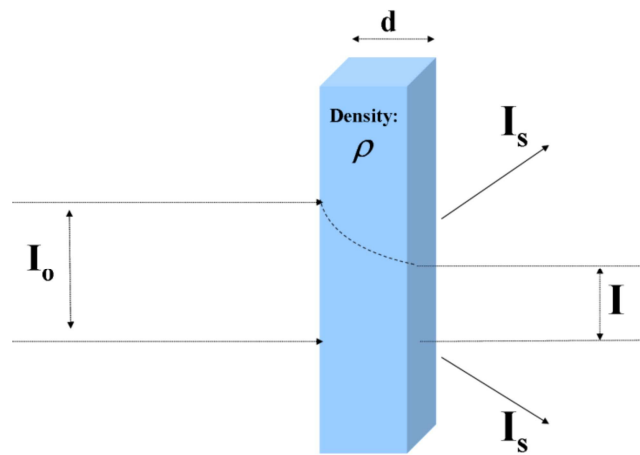


**Figure 3.1:** Attenuation interaction of electromagnetic wave with matter.

Cross section is defined as an effective area for collision of photons with the matter. This can also be defined as; it measures the effectiveness of the interaction between the incident particle or wave with the target matter. A cross section depends on the type of the particles and energy of the incoming beam. The amount of scattering from a medium is determined by the product of the scattering cross sections and the number of scattering sites. Figure 3.2 shows the schematic of scattering of a wave with matter at a solid angle  $\Delta\Omega$  in three dimensional spaces where the detector is located. The wave generated from the source incident on the sample and after interacting with the sample scattered in all direction and collected at the detector.

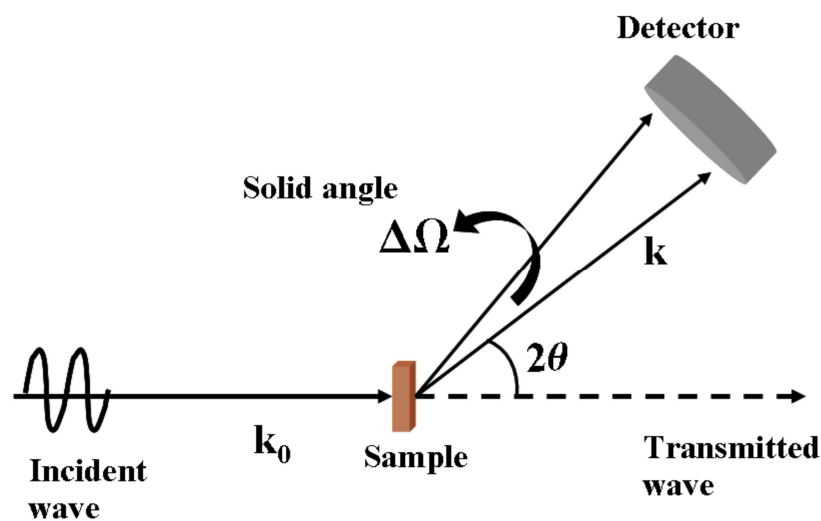


**Figure 3.2:** Scattering of wave by a medium.

The wave function for the incident electromagnetic or neutron wave as a plane wave is defined as:

$$I_{inc} = e^{(i\vec{k}_0 r)} \quad (3.3)$$

here  $k_0 = \frac{2\pi}{\lambda}$  is the momentum vector of the incident wave. After the interaction of the wave with the sample, the wave scattered in all directions and the wave function for the scattered wave is given by:

$$I_{scat} = A e^{i\vec{k} r} \quad (3.4)$$

where  $A$  is the scattering amplitude of the scattered outgoing wave. Since the electromagnetic waves scattered by the electrons distributed in an atom, the scattering amplitude not only depend on the distribution of electrons  $\rho(r)$ , but also on the scattering angle and wavelength of the incident wave. The scattering amplitude for scattered wave is given by:

$$A(\vec{q}) = \int \rho(r) e^{(-i\vec{q} \cdot \vec{r})} d\vec{r} \quad (3.5)$$

where  $\vec{q} = \vec{k} - \vec{k}_0$  is the momentum transfer vector. The scattering amplitude is proportional to the differential scattering cross section of the scattered wave. The total scattered intensity of the wave is evaluated from the differential scattering cross section, which is defined as a number of particles which are scattered into a solid angle  $d\Omega$  per second divided by the incident flux. The differential scattering cross section is given by:

$$\frac{d\sigma}{d\Omega} = \frac{C}{I_{flux} \cdot d\Omega} = |A(\vec{q})|^2 \quad (3.6)$$

where  $I_{flux}$  is the incident flux,  $C$  is the count rate of the scattered flux and  $d\Omega$  is the solid angle for the scattered wave at the detector. The above equation (3.6) reveals the probability of finding a scattered particles or wave within a given solid angle. The total scattering cross section which is proportional to the total scattered intensity is evaluated by the integral cross section over the whole sphere of observation. The total scattering cross section is given by:

$$\sigma = \int_0^\pi \int_0^{2\pi} \frac{d\sigma}{d\Omega} \sin \theta d\theta d\phi \quad (3.7)$$

Basically scattering cross sections are measured during the experiments. The total scattering is the integral over all angles of the differential cross section.

### 3.2 Small Angle X-ray Scattering (SAXS)

Small angle scattering (SAS) techniques, including small angle X-ray scattering (SAXS) and small angle neutron scattering (SANS), are capable to give information on the structural features of particles of colloidal size as well as their spatial correlation. Both SAXS and SANS are powerful techniques for determining size, shape and internal structure of particles in the size range from few nanometers up to about hundred nanometers [46,47]. SAXS is an elastic scattering of X-rays from the electrons in atoms and therefore it is sensitive to electron density fluctuations in samples, whereas SANS is an elastic scattering of neutrons at the atomic cores and sensitive to scattering length density differences.

Generally, when two or more parallel incoming waves as described by equation (3.3) interact with the sample then the scattered waves of variable intensities are emitted in all direction [48]. The scattered waves are spherically symmetric spherical waves. Figure 3.3 shows the schematic of interaction of the incident wave with two scattering centre 1 and 2 which are at  $r$  distance apart from each other. Due to different distance of the two volumes from the wave front, the scattered momentum wave vector  $k$  undergoes different phase shift.

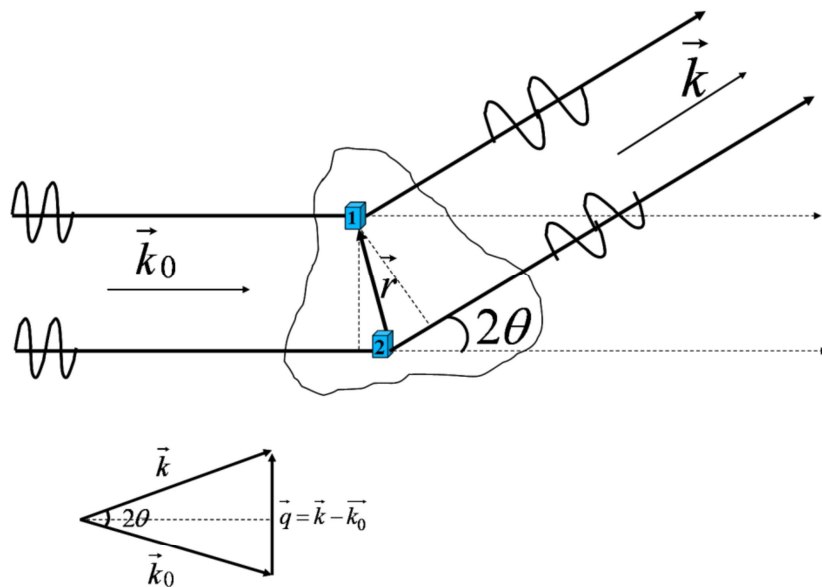


**Figure 3.3:** Scattering from nanoparticles.

The incident and scattered wave vector are described by  $\vec{k}_0$  and  $\vec{k}$ , respectively. The resultant intensity is the superposition of waves of different amplitudes and phases. The intensity also depends on the scattering angle  $2\theta$  and the momentum transfer

vector  $\vec{q} = \vec{k} - \vec{k}_0$ . For the elastic scattering the scattering wave has the same energy as the incident energy, therefore  $|k|=|k_0|$  is valid for the elastic scattering.

In small angle scattering experiments one measures the spatial correlations in the scattering density, averaged over the time scale of the measurement. The differential scattering cross section  $\frac{d\sigma}{d\Omega}(q)$  from a number distribution of scatters per unit volume  $N(r)$  can be calculated by the following expression:

$$\frac{d\sigma}{d\Omega}(q) = \int_0^{\infty} N(r) V_p(r)^2 |F(q, r, \Delta\eta(E))|^2 S(q, r) dr \quad (3.8)$$

where  $\Delta\eta(E) = \eta_{particle} - \eta_{matrix}$  is the averaged electron density fluctuation between the particle and remaining matrix.  $V_p(r)$  is the volume of the particle. Also  $q$  is momentum transferred, which is related with the scattering angle  $2\theta$  and the wavelength  $\lambda$  of X-rays as:

$$|\vec{q}| = q = \frac{4\pi \sin \theta}{\lambda} \quad (3.9)$$

The small angle scattering measurements are sensitive to the inhomogenities of the electron density of different nanosized phases in the sample, termed as contrast. The visibility of detecting the particle in SAS measurement increases with enhancing the electron density difference between the different phases in the sample. The electron density is evaluated by the product of atom number density and the number of electrons of each atom is given by:

$$\eta = N_A \rho \frac{\sum_i c_i Z_i}{\sum_i c_i M_i} \quad (3.10)$$

where  $N_A$  is the Avagodaro number,  $\rho$  is the mass density of the total phase and  $Z$  is the atomic number of the  $i$  elements.  $c_i$  is the atomic concentration and  $M_i$  is the atomic mass of the particular element  $i$  present in the phase.

In equation (3.8),  $F(q, r, \Delta\eta(E))$  is the form factor which accounts for the shape and size of particles. The form factor is the important factor while fitting the experimental data with the theoretically assumed model except in the structural biology where the shape of the particles is often the target of the study. For a homogenous sphere with the radius  $r$ , the form factor is defined as [49,50]:

$$F(q, r, \Delta\eta(E)) = 3\Delta\eta(E) \frac{\sin(qr) - (qr) \cos(qr)}{(qr)^3} \quad (3.11)$$

It depends on the scattering vector  $q$ , the radius of the particle  $r$  and the electron density difference between the particles and remaining matrix represented by  $\Delta\eta(E)$ .

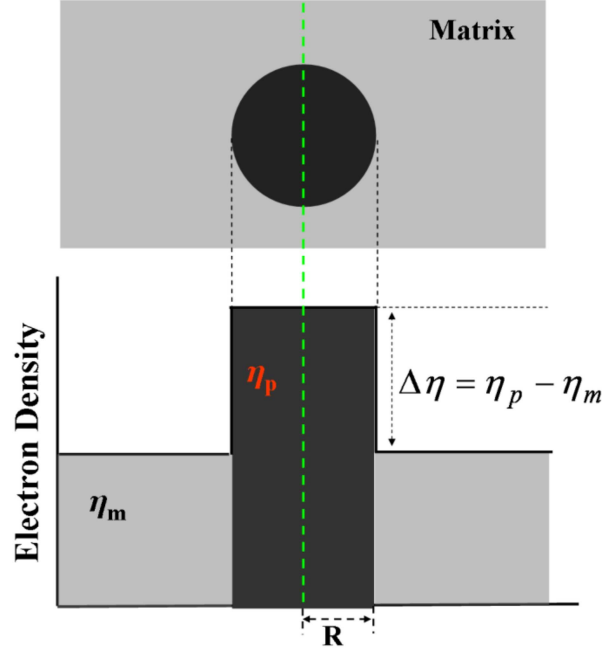


**Figure 3.4:** Sketch of an electron density profile of spherical model where the electron density  $\eta_p$  of particle is larger than that of the matrix  $\eta_m$ .

The electron density difference profile with respect to the remaining matrix for a spherical shape particle is shown in Figure 3.4. In equation (3.8)  $N(r)$  is the particle distribution function which is used during the simulations of SAXS scattering curves. In our investigations we have chosen two kinds of distribution functions, lognormal and Gauss distribution. The lognormal distribution for particles is given as:

$$N(r) = \frac{1}{(2\pi)^2 r \sigma} \exp\left[\frac{-\ln\left(\frac{r}{\mu}\right)^2}{2\sigma^2}\right] \quad (3.12)$$

where  $r > 0$ .

$$\begin{aligned} \langle \mu \rangle &= \mu \exp\left(\frac{\sigma^2}{2}\right) \\ \langle \sigma \rangle &= \mu \sqrt{(-1 + \exp(\sigma^2)) \exp(\sigma^2)} \end{aligned}$$

The Gauss distribution of particles is given as:

$$N(r) = \frac{1}{\sqrt{2\pi\sigma^2}} \exp\left[\frac{-(r - \mu)^2}{2\sigma^2}\right] \quad (3.13)$$

where  $\mu$  is the mean and  $\sigma$  is the standard deviation of the particles.

In dense particular systems it is necessary to account for interparticle interaction (structure factor). Such interactions will be calculated within approximations. Mainly, the local monodisperse approximation and the decoupling approximation are used for dense particulate system [51,52]. Complete randomness of size and position of particles is assumed in decoupling approximation, while in local monodisperse approximation a particle of certain size is surrounded by particles with the same size. The structure assuming a hard sphere potential is given as [53,54]:

$$S(q, R_{HS}, f_p) = \frac{1}{1 + 24f_p \frac{G(f_p, 2R_{HS}q)}{2R_{HS}q}} \quad (3.14)$$

where

$$G(q, A) = \alpha \frac{\sin A - A \cos A}{A^2} + \beta \frac{2A \sin A + (2 - A^2) \cos A - 2}{A^3} \\ \gamma \frac{-A^4 \cos A + 4[(3A^2 - 6) \cos A + (A^3 - 6A) \sin A + 6]}{A^5} \\ \alpha = \frac{(1 + 2f_p)^2}{(1 - f_p)^4}; \quad \beta = -6f_p \frac{\left(1 + \frac{f_p}{2}\right)^2}{(1 - f_p)^4}; \quad \gamma = \frac{f_p \alpha}{2}$$

A constant scattering background coming from fluorescence and resonant Raman scattering is also added to equation (3.8).

Subtracting the form factor of the inner sphere from the outer sphere provides the case of spherical core shell form factor.

$$F(q, r, \Delta\eta(E), \mu) = F(q, r, \Delta\eta(E)) - F(q, vr, \Delta\eta(E))(1 - \mu) \quad (3.15)$$

where  $\Delta\eta(E)$  is the electron density difference between shell and matrix and  $\mu \cdot \Delta\eta(E)$  is the electron density difference between core and matrix. The total radius of the particles is defined by  $r$  and the radius of the core  $r_c = \nu r$ .

There are different ways of variation of the electron density difference between the core, shell and the remaining matrix. Figure 3.5 (a) and (b) shows the two main types of variation of electron density profile for a spherical core shell type particles. In Figure 3.5 (a) a sink like electron density profile is shown, while a stair like electron density profile in Figure 3.5 (b) is shown.

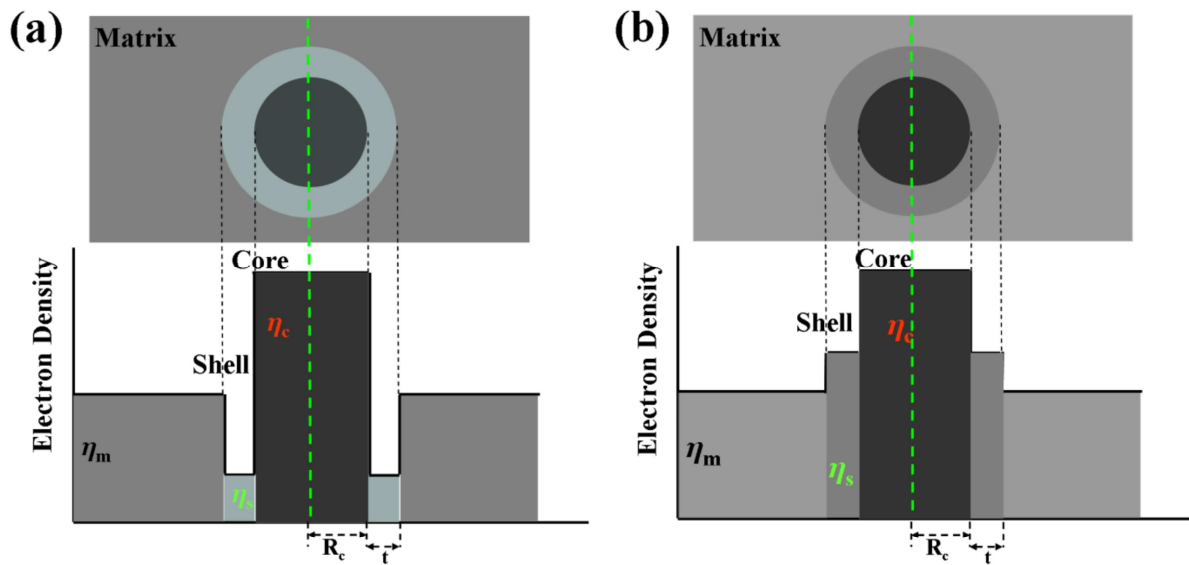


**Figure 3.5:** Sketch of two main electron density profiles, shows how the electron density can vary between core, shell and matrix. (a) Spherical core shell particle with an electron density of the shell smaller than the matrix and one of the core is larger than that of the matrix. (b) Spherical core shell particle with electron density of the core shell larger than the matrix.

Figure 3.5 (b) shows the steps like profile where the electron density of the core and shell are greater than that of the matrix which represents the positive contrast for the core and shell. While in the Figure 3.5 (a) shows the profile in which the electron density of core is greater than the matrix, while the electron density of the shell is smaller than the matrix, which gives a core contrast that is positive and a shell contrast that is negative.

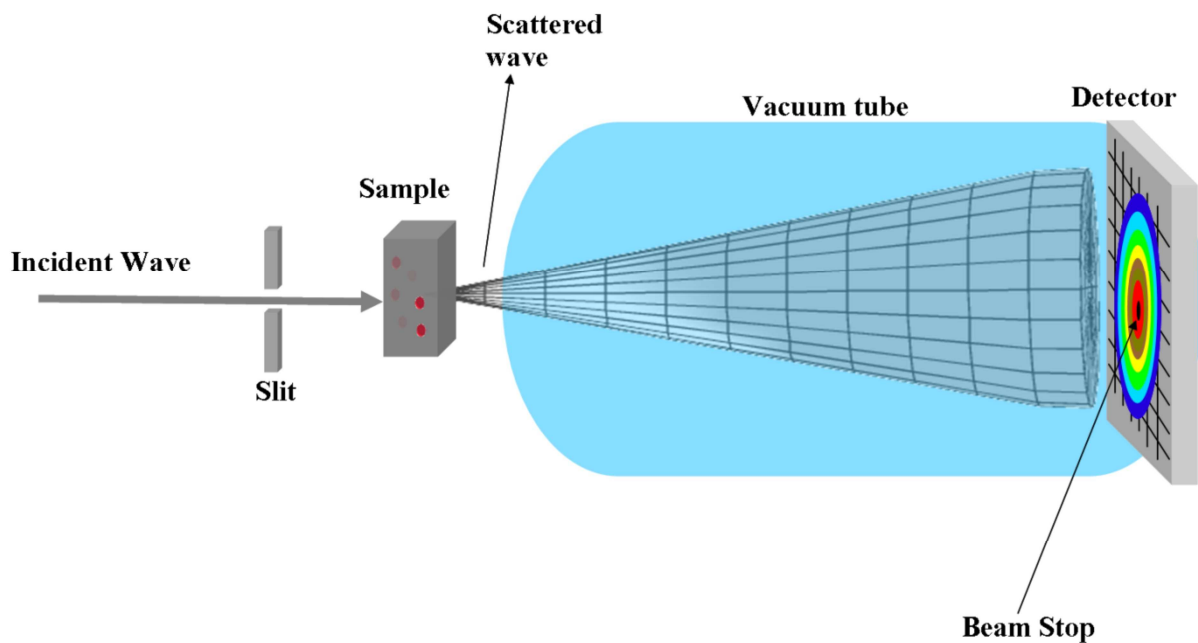


**Figure 3.6:** Sketch of a small angle scattering setup.

Figure 3.6 shows the sketch of a small angle X-ray scattering setup. In the above sketch, X-ray wave of certain energy interacts with the sample and scatters from the particles. The scattered wave passes through a vacuum tube (to reduce the air scattering) and hits the detector. The transmission, calibrating standard and background are measured with the samples to correct and to calibrate the scattering images. Distance between the sample and detector can vary in order to achieve the wide  $q$  range. A beam stop which is a good absorber for X-rays is placed in the centre of the detector.

### 3.3 Anomalous Small Angle X-ray Scattering (ASAXS)

By SAXS investigation at different energies near the absorption edge of an element also termed as ASAXS, enables to isolate the scattering from that particular element with respect to rest of the surrounding matrix. ASAXS technique is applied to determine the spatial distribution of a specific element on a nanometer scale. In ASAXS the anomalous properties of the scattering amplitude is used. The atomic scattering amplitude  $f$  is the ratio of the wave amplitude scattered by the actual electron distribution in an atom to that scattered by free electron localized at a point [55]. Anomalous small angle X-ray scattering (ASAXS) refers to variation in contrast of scatter in a system by using the physical phenomenon of anomalous dispersion of X-rays near the absorption edge of an element. This phenomenon of dispersion occurs when the X-ray photon energy reaches the binding energy of an electron in the sample [56]. The atomic scattering amplitudes changes significantly near the energy absorption edge of an element as shown in Figure 3.7. This drop is due to the resonance effect by the bound electron. When the energy of X-rays increases beyond the binding energy, the X-rays are absorbed and liberate the bound electron.

The scattering amplitude is given near to an edge of any element by:

$$f(E) = f_0 + f'(E) + if''(E) \quad (3.16)$$

where  $E$  is the X-ray energy and  $f_0 = Z$ , where  $Z$  is the number of electron of the element.

The second and third terms are the complex anomalous dispersion corrections to the scattering amplitude and depend on both atomic number of the elements in the sample and the photon energy. Far from the absorption edge, SAXS intensities are proportional to the atomic number of the element  $Z$ .

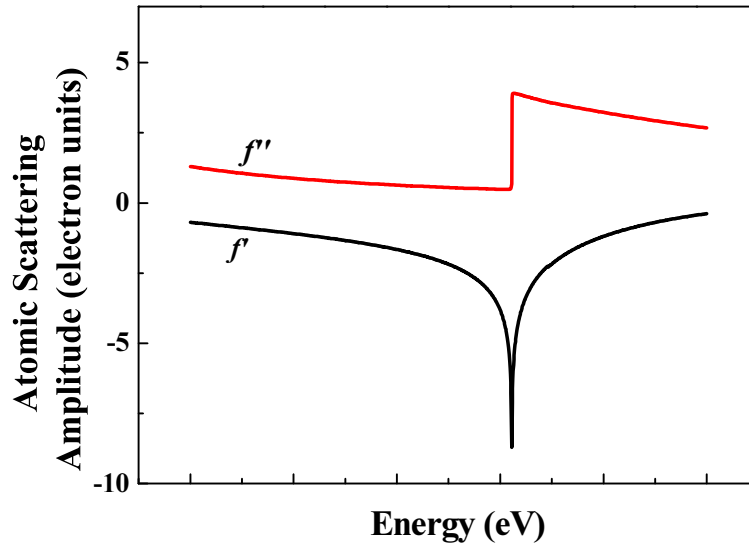


**Figure 3.7:** Typical atomic scattering amplitude variation near an X-ray absorption edge of that element.

Optical theorem gives the relation between  $f''$  and the atomic absorption coefficient  $\mu_a$  at an incident photon energy  $E$  as:

$$f'' = \frac{m_e c \epsilon_0 E \mu_a}{e \hbar} \quad (3.17)$$

where  $e$  is the classical radius of an electron,  $c$  is the velocity of light,  $h$  is Planck's constant,  $\mu_a$  is the attenuation coefficient per atom. Thus the increase in absorption is described in the imaginary part,  $f''(E)$ . With further increases in the photon energy, the absorption decreases smoothly. The real and imaginary parts of the scattering factors are connected to each other by famous Kramers- Kronig relation defined as:

$$f'(E_0) = \frac{2}{\pi} \int_0^{\infty} \frac{E f''(E)}{E_0^2 - E^2} dE \quad (3.18)$$

Theoretically calculated scattering factors values have been used for the experiment, which is tabulated by Cromer and Liberman [57]. Fluorescence, which is constant and occurs when the incident photon energy is above the electron binding energy, leads to an increased background in a small angle X-ray scattering experiment. Therefore it is appropriate to perform SAXS experiments below the absorption edge to avoid the fluorescence.

The small angle scattering from precipitates that are enriched with the anomalous element may be isolated both qualitatively and quantitatively, even in the presence of other scatterers which are not enriched with the anomalous element. SAXS is a contrast dependent technique

where the electron density fluctuation is proportional to the amplitude of atomic scattering factors given as:

$$(\Delta\eta(E))^2 \propto f^*(E)f(E) = f_o^2 + 2f_o f'(E) + f''(E)^2 \quad (3.19)$$

in ASAXS contribution of particular element (resonant atoms) in the scattering intensity is separated from the total scattered intensity by calculating the resonant curve using the Stuhrmann equation [58,59].

$$I(q, E) = F_O(q) + f'(E)F_{OR}(q) + (f'(E)^2 + f''(E)^2)F_R(q) \quad (3.20)$$

where  $F_O(q)$  -- Normal SAXS term

$F_{OR}(q)$  -- Scattering cross term

$F_R(q)$  -- Resonant Scattering term

Solving the above equation (3.20) for three or more energies, allows us to separate the resonant scattering term from the rest of the combined SAXS term. The resonant scattering term contains the information about the spatial distribution of the resonant scattering atoms only.

ASAXS not only gives a qualitative characterization of specific element, but also it provides quantitative information about the distribution of the resonant atoms. The number density of the resonant atoms can be calculated by using the following equation as reported earlier by Goerigk et. al. [60,61]:

$$N = \frac{1}{2V_z} \pm \sqrt{\frac{1}{4V_z^2} - \frac{1}{(2\pi)^3 r_e^2} \int |F_R(q)|^2 d^3q} \quad (3.21)$$

where  $V_z = \frac{4}{3}\pi R_z^3$  is the volume of the Z atoms with ionic radius  $R_z$  and  $r_e$  is the classical electron radius. The integral represents the  $Q$  invariant of the resonant curve.

### 3.4 Energy dependent scattering contrast

The compositions were calculated by two different fitting routines. First, all ASAXS curves were simultaneously fitted with the software SASfit [62] which used equation (3.8) in order to obtain the nanostructure and the experimental contrast at a particular absorption edge. After fitting we have different values of experimental contrast for different energies.

Second, after determining the relative experimental contrasts values from the first fitting

routine, these contrasts values were further fitted with the theoretically calculated contrasts in a separate MATLAB routine. For calculating theoretical contrast, the total numbers of atoms of each element were distributed into the nanoparticle (core), shell and in the remaining glass matrix. The number of moles of each elements as well as the stoichiometry for the crystalline phase is kept constant during fitting. For a crystalline phase  $P_lQ_m$  in the core, the effective electron density is calculated as follows:

$$\eta_{core}(E) = \frac{N_A D_C x P_l}{M_C} \left[ f_p(E) + \sum_i \frac{m_i}{l} f_i(E) \right] \quad (3.22)$$

where  $N_A$  is the Avogadro number,  $D_C$  is the mass density and  $M_C$  is the total molar mass of the crystalline phase.  $P_l$  is the total number of moles of an element  $P$  in the system before heat treatment.  $x$  ( $0 < x < 1$ ) is the fraction of moles out of total  $P_l$  moles used in the formation of crystals after heat treatment. The number of moles for other elements (such as  $Q$ ) in the crystalline phase is evaluated by the stoichiometric ratio  $m/l$ . Theoretically calculated atomic scattering amplitude for an element  $P$  is given by  $f_p(E)$  and the atomic scattering amplitudes for all the other elements present in the crystalline phase is given by  $f_i(E)$ , where the index of summation  $i$  represents all the other elements present in the crystalline phase except  $P$ .

After the distribution of moles for a crystalline phase forming elements in the core, the remaining moles of  $P$  and  $Q$  and the moles of all other elements present in the glass are distributed into the shell and the remaining matrix. The effective electron density of the shell is given by:

$$\eta_{shell}(E) = \frac{N_A D_S}{M_S} \left[ y(1-x)P_l f_p(E) + z \left( Q_l - \frac{m}{l} x P_l \right) f_Q(E) + \sum_i u_i N_i f_i(E) \right] \quad (3.23)$$

where  $D_S$  is the mass density and  $M_S$  is the total molar mass of the shell. In the first two terms,  $y$  ( $0 < y < 1$ ) and  $z$  ( $0 < z < 1$ ) are the fractions of moles of element  $P$  and  $Q$  from the remaining moles left in the system after the core formation. The last term  $u_i$  ( $0 < u < 1$ ) is the fraction of moles for all the other elements  $N_i$  (except the elements in the core) present in the system and the index of summation  $i$  represents the number of elements.

After the formation of a core and a shell, the remaining fraction of mole for each element must be present in the matrix. The effective electron density of the matrix is given as:

$$\eta_{matrix}(E) = \frac{N_A D_M}{M_M} \left[ (1-x-y(1-x))P_l f_p(E) + \left( Q_l - P_l \left( x \frac{m}{l} + z \left( \frac{Q_l}{P_l} - \frac{m}{l} x \right) \right) \right) f_Q(E) + \sum_i N_i (1-u_i) f_i(E) \right] \quad (3.24)$$

where  $D_M$  is the mass density and  $M_M$  is the total molar mass of the remaining matrix. The first two terms are the moles of the elements ( $P$  and  $Q$ ) finally left in the matrix after the formation of crystalline core and the shell. The last term represents the number of moles of all the other elements  $N_i$  (except  $P$  and  $Q$ ) left in the matrix after the formation of shell.

While fitting  $x$ ,  $y$ ,  $z$ ,  $u_b$ ,  $D_C$ ,  $D_S$  and  $D_M$  were used as fitting variables to calculate the theoretical contrast, which is the difference of the electron densities of core, shell and remaining matrix, which is calculated as follows:

$$\frac{\Delta\eta(E_n)}{\Delta\eta(E_1)} = \frac{|\eta_{core}(E_n) - \eta_{matrix}(E_n)|}{|\eta_{core}(E_1) - \eta_{matrix}(E_1)|} \quad (3.25)$$

By using the above equation for relative change in the energy dependent contrast enables to evaluate the composition and density of the spherical core-shell particles in the studied system.

Due to the anomalous dispersion of atomic scattering amplitudes  $f'$  and  $f''$  near the electron binding energy makes a variable photon energies as a basic requirement of ASAXS. Such type of X-ray source with variable photon energy is available only at the synchrotrons. Broad high-intensity spectrum, high intensity, good angular collimation makes synchrotron a suitable tool for ASAXS. The energy resolution, defined as  $\Delta E/E$ , is also important for diminishing the smearing effect near the absorption edge.

### 3.5 Small Angle Neutron Scattering (SANS)

Scattering of cold neutrons has become an elegant and powerful probe of both static and dynamical properties of chemical and magnetic structure of solids. The power of the neutron relies on a number of fortunate intrinsic properties such as electric neutrality, which makes it penetrate easily into a bulky sample. By means of the strong nuclear forces, the neutron interacts with the atomic nuclei of the sample. As the neutron possesses a magnetic moment, it interacts also through magnetic dipole forces with the unpaired electrons of the sample. Due to the actual value of the neutron mass, neutrons with energies of the order of  $meV$  have de Broglie wavelengths of the order of Angstrom. In a scattering experiment, the detectable momentum transfer is thus of the order of inverse atomic distance and at the same time, the detectable energy transfer is comparable to the characteristic energies of structural and magnetic excitations in solids.

The fundamental difference between the X-rays and neutron is the interaction with the matter. X-rays scatter by an electron shell of the atom, while the neutrons interact with the atomic nuclei called as neutron scattering. Due to the electric neutrality of neutrons, it interacts weakly with the matter and penetrates deeply in the matter up to several millimeters. Since the neutrons has a small magnetic moment, which interact with the spin and orbital magnetic moment of atoms causing magnetic scattering. The other differences are the scattering cross section for the electromagnetic wave varies with the square of the atomic number of the element, while for neutrons the neutron-nucleus scattering cross section varies randomly respective to the atom number and depends also on the isotopes of the elements. The de Broglie and Schrödinger wave particle principle provides the relation between the energy of the neutron with its respective wavelength as:

$$E = \frac{\hbar^2 k^2}{2m_n} \quad (3.26)$$

where  $k$  is the wave vector and  $m_n$  is the mass of the neutron  $1.67 \times 10^{-27}$  kg.

Small Angle Neutron Scattering (SANS) is a complementary method to SAXS and analyses the same nanostructures, but having different contrasts. Additionally, scattering of neutrons by the magnetic moments of atoms enable to determine both the chemical and magnetic structure of materials. Also, the use of using polarized SANS permits to separate the nuclear and magnetic scattering independently. The total scattering cross section of a system is given similarly as we shown for the SAXS measurements in equation (3.8), only the contrast has to be defined in terms of nuclear scattering length density which is given as [48]:

$$\eta_i = \frac{1}{V} \sum_i^N b_i \quad (3.27)$$

where  $V$  is the volume containing  $N$  atoms and  $b_i$  is the (bound coherent) scattering length of the  $i^{th}$  atom in the volume.  $V$  is usually the molecular or molar volume for a homogenous phase in the system of interest.

#### *Nuclear Scattering*

In SANS experiment neutrons are interacting with a complex array of spatially distributed nuclei. When there are more than one phase is present in the studied sample, then the cross section includes the different nuclear length densities and volumes for each phase in the material. The scattering length density then modified as:

$$\eta = N_A \rho \frac{\sum_{i=1}^N c_i b_i}{\sum_{i=1}^N c_i M_i} \quad (3.28)$$

where  $c_i$  is the atomic part,  $b_i$  is the nuclear scattering length of atoms of the  $i^{th}$  element and  $M_i$  is the atomic weight of element  $i$  containing in the phase and  $\rho$  is the mass density of the phase. Then the scattering cross section is proportional to the square of the difference in neutron scattering length density of different phases present in the sample also called as **nuclear contrast**,  $\Delta\eta_{nucl}^2 = (\eta_1 - \eta_2)^2$  and the nuclear scattering cross section is given as:

$$\left( \frac{d\sigma}{d\Omega}(\vec{q}) \right)_{nuclear} \propto \Delta\eta_{nucl}^2 |F_N(q, r)|^2 \quad (3.29)$$

where  $F_N(q, r)$  is the nuclear form factor of the particles.

### Magnetic Scattering

Neutrons have magnetic moment which interact with the magnetic moment of an atom with unpaired electron spins and contributes as a magnetic scattering. The contrast for the magnetic scattering comes from the moment of neutron  $\mu_n$  and moment of electron  $\mu_e$ . The unpaired electron spins form the magnetic moment of the atom. Since SAS has no atomic resolution the scattering is describe by the total magnetization  $\vec{M}$  of a nanosized phase that appears. The magnetic contrast is defined as the difference between the magnetizations of the phases in the sample. For a two phase system (matrix and particles) it is given as:

$$\Delta\eta_{magn} \propto \mu_n \left[ \frac{\vec{q} \times (\vec{M} \times \vec{q})}{q^2} \right] \propto (M_{par} - M_{mat}) \quad (3.30)$$

where  $M_{par}$  and  $M_{mat}$  are the magnetization of the crystalline phase and the remaining matrix phase. The magnetic scattering measured at a 2D detector has an angular dependence by a factor of  $\sin^2\psi$  where  $\psi$  is the angle between the direction of external homogenous magnetic field applied to the sample and the scattering vector  $\vec{q}$ . So from the above equation (3.30) it is concluded that, when the direction of the vector  $\vec{q}$  is parallel ( $\psi=0^\circ$ ) to the magnetization direction, no magnetic scattering appears if all magnetic moments in the sample aligned by the external field. While the case with  $\vec{q}$  perpendicular to the magnetization direction for  $\psi=90^\circ$  results in mixture of magnetic and nuclear scattering. The magnetic scattering density is defined as:

$$\eta_{magn} = \frac{N_A \rho \mu m}{\sum_{i=1}^N c_i M_i} \quad (3.31)$$

where  $c_i$  is the atomic part of the element  $i$ ,  $m$  is the magnetization of the phase in Bohr magnetons per atoms perpendicular to momentum vector  $\vec{q}$  and  $M_i$  is the atomic weight of the element  $i$  in the phase and  $\mu = 0.27 \times 10^{-12}$  cm is an unit conversion multiplier. The magnetic scattering cross section is given as:

$$\left( \frac{d\sigma}{d\Omega}(\vec{q}) \right)_{magnetic} \propto \Delta \eta_{magn}^2 \sin^2 \psi |F_M(q, r)|^2 \quad (3.32)$$

where  $F_M(q, r)$  is the magnetic form factor.

### 3.6 Polarized Small Angle Neutron Scattering (polarized SANS)

When the incoming monochromatic neutron beam is unpolarized in nature such that the neutron spin is randomly distributed, then the scattering cross section is the sum of the scattering cross section of isotropic nuclear and anisotropic magnetic scattering given as [63]:

$$\frac{d\sigma}{d\Omega}(\vec{q}) = \left( \frac{d\sigma}{d\Omega}(\vec{q}) \right)_{nuclear} + \left( \frac{d\sigma}{d\Omega}(\vec{q}) \right)_{magnetic} \quad (3.33)$$

After putting the values from equation(3.29) and equation(3.32) in above equation we can conclude that the scattering intensities measured perpendicular to the applied magnetic field results the sum of nuclear and magnetic scattering, While the scattering intensities measured parallel to magnetic field results only the nuclear scattering. When the magnetic contrast is very small compared to the nuclear contrast then the magnetic caused anisotropic signal is very weak and hard to measure precisely.

In order to extract the magnetic scattering, one possibility is to use the polarized neutron beam, by using the specific spin orientation of the neutron either parallel or antiparallel to the applied magnetic field [64]. In the polarized SANS experiment the constant magnetic field is applied on the sample in such a way that the direction of the field is perpendicular to the direction of the incident neutron beam. A polarizer is used to polarize the neutron beam guided through the collimation tube. A spin flipper is used to flip the spins just before the sample position. There are two possible situation for the flippers either it is ON or OFF and

depending on it the flipper flips the spin of the polarized neutron either parallel or antiparallel to the applied magnetic field.

When the flipper is OFF then the state of polarized neutron ( $n^+$  or  $n^-$ ) is scattered through the sample without change of the spin. In this situation we measured the scattering cross section either  $\left(\frac{d\sigma}{d\Omega}\right)^{++}$  or  $\left(\frac{d\sigma}{d\Omega}\right)^{+-}$  called as non spin flip scattering (NSF). But when the flipper is ON then the flippers flips the spin of the polarized neutrons and we measured the scattering cross section either  $\left(\frac{d\sigma}{d\Omega}\right)^{--}$  or  $\left(\frac{d\sigma}{d\Omega}\right)^{-+}$  depending on the incident polarized direction of the neutrons and called as spin flip scattering (SF). So we have four scattering cross sections two for NSF and two for SF.

If the analyzer is not used then the scattered neutrons collected at the detector contains the contribution from both the SF and NSF and depends on the polarization of the incident neutron beam. When the neutron polarization and magnetic moments are directed along the external applied magnetic field, then the cross sections are given by [7]:

$$\begin{aligned} \frac{d\sigma}{d\Omega}(q, \psi)^+ &= \left(\frac{d\sigma}{d\Omega}\right)^{++} + \left(\frac{d\sigma}{d\Omega}\right)^{+-} = \Delta\eta_{nuc}^2 F_N^2(q, r) + \left[ \Delta\eta_{magn}^2 F_M^2(q, r) - \right. \\ &\quad \left. 2P(1 - 2\varepsilon^+) \Delta\eta_{nuc} F_N(q, r) \Delta\eta_{magn} F_M(q, r) \right] \sin^2 \psi \end{aligned} \quad (3.34)$$

$$\begin{aligned} \frac{d\sigma}{d\Omega}(q, \psi)^- &= \left(\frac{d\sigma}{d\Omega}\right)^{--} + \left(\frac{d\sigma}{d\Omega}\right)^{-+} = \Delta\eta_{nuc}^2 F_N^2(q, r) + \left[ \Delta\eta_{magn}^2 F_M^2(q, r) - \right. \\ &\quad \left. 2P(1 - 2\varepsilon^-) \Delta\eta_{nuc} F_N(q, r) \Delta\eta_{magn} F_M(q, r) \right] \sin^2 \psi \end{aligned} \quad (3.35)$$

where  $P$  is the polarization of the neutron and defined as:

$$P = \frac{N^+ - N^-}{N^+ + N^-} \quad (3.36)$$

where  $N^+$  is the number of neutron having spin anti-parallel and  $N^-$  spin parallel to the applied magnetic field direction  $H$ . The efficiency of the spin flipper is shown by  $\varepsilon$ . When the flipper is ON efficiency is close to unity  $\varepsilon \approx 1$  and for OFF efficiency is zero ( $\varepsilon = 0$ ).



## 4 Experimental

### 4.1 SAXS and ASAXS at BESSY II

#### 4.1.1 Beamline description

A system that delivers, chooses photons upon the requirements of the samples and shapes the beam profile accordingly to the requirement of the experiment is denoted as a beamline. The ASAXS beamline at BESSY II (HZB) uses a 7 Tesla multipole wiggler (7T-MPW) photon source with a critical energy of 13.5keV for  $E=1.7\text{GeV}$  [65]. The wiggler allows a very high photon flux with wide X-ray energy range from about 3.5keV to 28keV will be used in the monochromatic branch for ASAXS. The beamline can be divided into four parts. These are the *optics* (Figure 4.1) which contains slit system, *beam forming and beam monitoring-region*, the *sample environment* and the *detections system* for the small angle scattering signal. From the source to sample, the beam has to pass a collimating mirror for the white beam, a Si (111) double crystal monochromator and a focusing mirror. A schematic sketch of the beamline optics is shown in Figure 4.1.

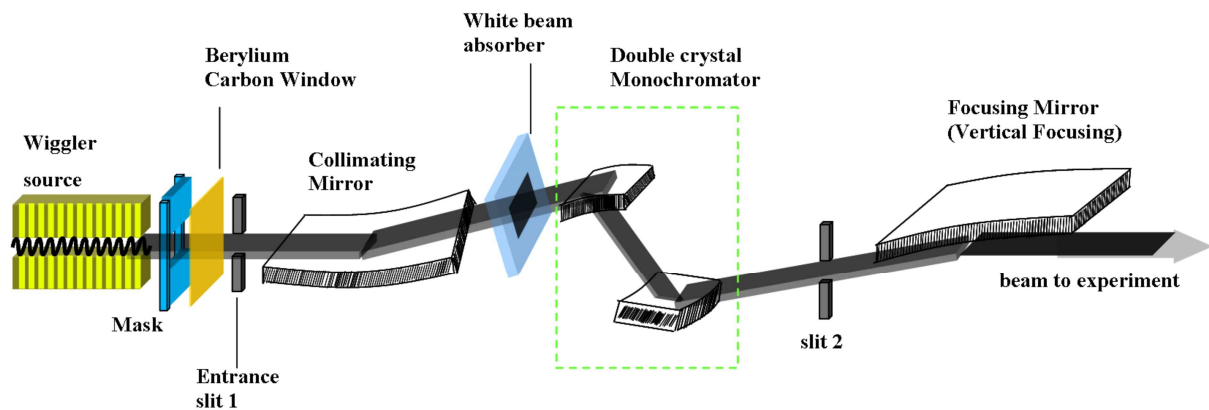


*Figure 4.1: Schematic view of the optics of the beamline from wiggler source.*

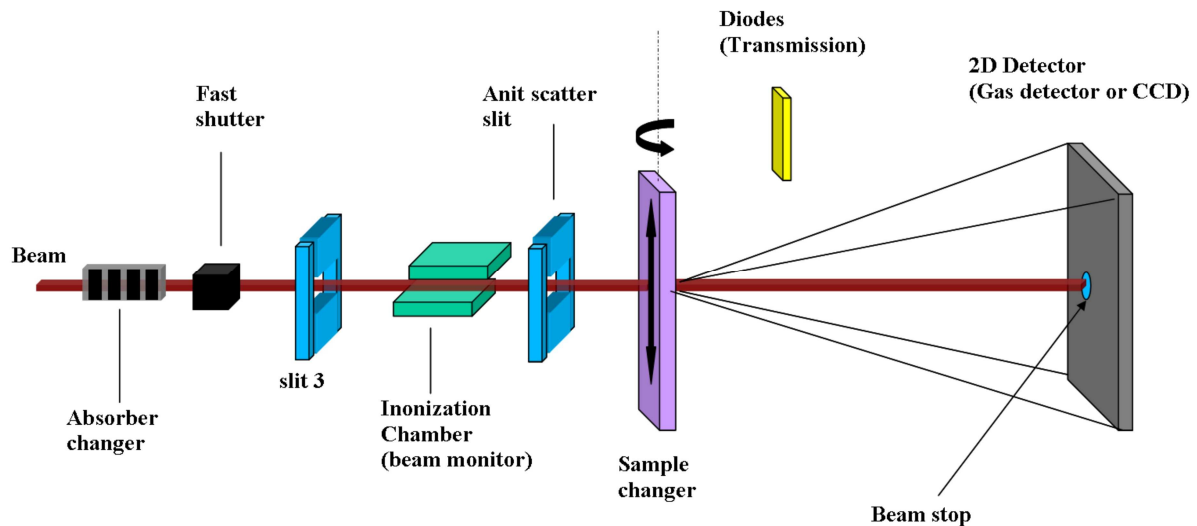


**Figure 4.2:** Schematic view of the SAXS-setup in the experimental hutch after the optical hutch.

There are two main sections of the beamline:

- (i) *Optical Hutch (Figure 4.1)*
- (ii) *Experimental Hutch (Figure 4.2)*

#### *Optical Hutch*

The first section after the beam source is the optical hutch, which contains the X-ray optics mainly consisting of 2 mirrors and a double crystal monochromator. From wiggler the beam hits the aperture and the primary slit 1, which defines the horizontal and vertical cross section of the beam hitting the first mirror. The slit one has usually size of 10mm by 3mm (horizontal\*vertical) depending on the mirror angle and defines mainly the divergence. The first mirror is the collimating mirrors, with pitch angle variable between 0-5 milliradians. The mirror provides a vertically parallel beam on the monochromator. The two mirrors have two tracks from silicon and from rhodium to provide X-ray reflexion till high energies. The function of the Double Crystal Monochromator (DCM) is to select and transmit X-ray radiation of desired photon energy from an incident white synchrotron radiation beam. Our X-ray monochromator is consists of two silicon crystals cuted to the Si (111) plane. The Si (111) has a ‘ $d$ ’ spacing of 1.135 Angstroms, which act as a diffraction grating to produce an angle dependent monochromatic beam by following Bragg’s law:

$$\sin \theta = \frac{n\lambda}{2d} \quad (4.1)$$

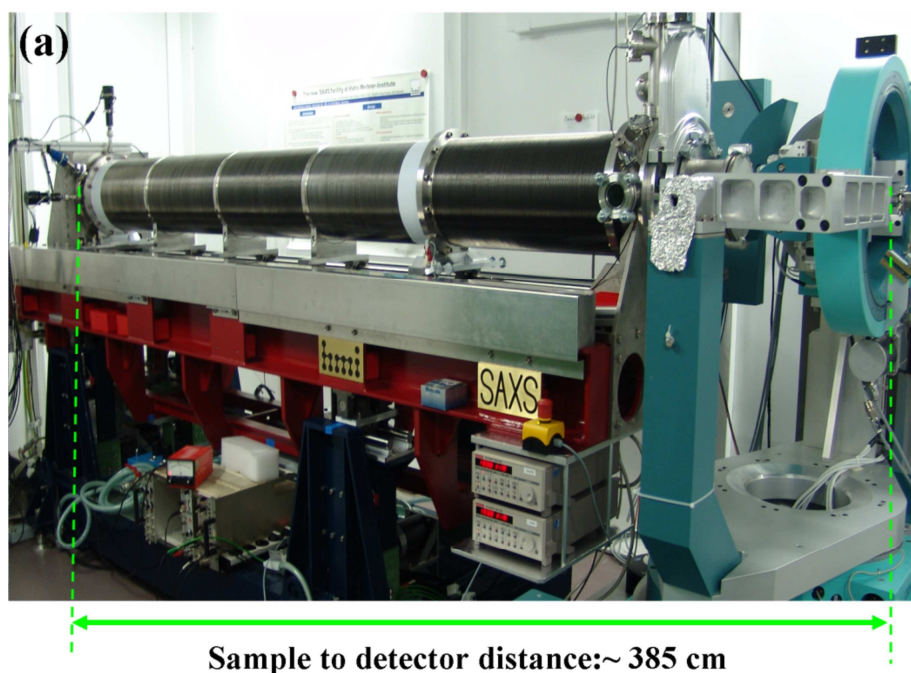
where ‘ $d$ ’ spacing is fixed and  $\theta$  is the incidence angle and  $\lambda$  is the wavelength of energy. The energy will be selected by rotating both the crystals and varying the Bragg angle whilst keeping the crystals parallel to each other. A Si (111) crystal monochromator will produce a monochromatic beam with an energy resolution,  $(\Delta E/E) = 1.2 \times 10^{-4}$ . After passing through monochromator, the beam can be focused vertically by a second mirror.

The beamline has an option for tuning of energies higher than 15.2keV by removing the mirrors. The beam forming and analysis region consists of the slit system, the absorbers to vary the primary intensity, a fast shutter and the ionic chamber to monitor the incoming beam that hits the sample. These parts are distributed in both the optical and experimental hutches.

#### *Experimental Hutch*

The small angle scattering process and the detection and data collection takes place in the experimental hutch. A schematic view is show in Figure 4.2 and Figure 4.3 shows the SAXS experimental setup in two geometric configurations from the sample chamber to the 2D SAXS detector.

The sample environments are usually places in the center of a Huber diffractometer. The main environment used in this thesis in a vacuum sample chamber in those a sample changer is mounted (Figure 4.3 (b)). Additionally the chamber can be equipped with a furnace. The advantage of the vacuum environment is the reduction of air scattering and no additional windows are necessary.



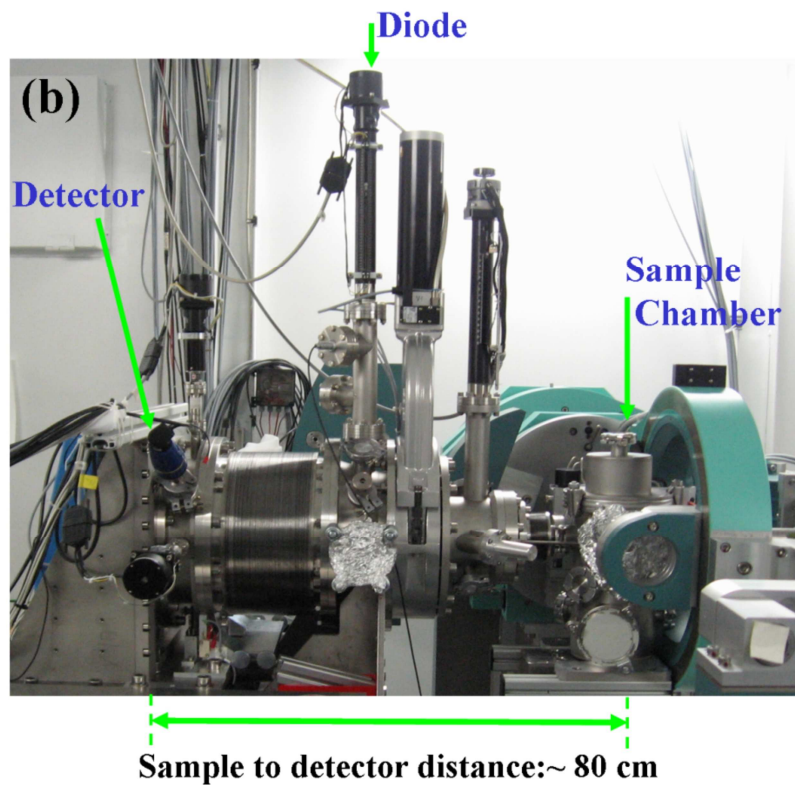


**Figure 4.3:** Experimental SAXS setup installed at BESSY II, Helmholtz-Zentrum Berlin: (a) detector at long distance from the sample and (b) detector at short distance from the sample.

The SAXS instrument is shown in Figures 4.3. The main part is an optical bench that can be tilted for GISAXS. Different area detectors can be attached at the end of a vacuum scattering part. This part is constructed by using an innovative solution of an edge welded bellow system. Therefore, the sample detector distance, that means the  $q$ -range, can be varied without breaking the vacuum between 80cm and 380cm.

Two different detectors are possible to be used. The standard detector in case of ASAXS is a 2D delayline gasfilled detector (MWPC) that can perform single photon counting while having a low background. The second detector is a MAR CCD 165 that will be used in case of very strong scattering samples and in case of GISAXS.

#### 4.1.2 Data reduction / SASREDTOOL

During the SAXS measurement, photons scattered from the samples are collected at a two dimensional detector in  $x$ - $y$  plane. But these two-dimensional images have to be corrected for various parameters and finally converted into one dimensional curve. The scattered intensity from the particle at detector is corrected by the following formula:

$$I(x, y) = \left( \frac{I_s(x, z)T - I_D.t}{\tau_s I_{os}} - \frac{I_b(x, z)T - I_D.t}{\tau_b I_{ob}} \right) \times \frac{1}{S(x, y)\Omega_{x,y}} \quad (4.2)$$

where  $I_s(x, y)$  is the scattered intensity from the sample which is collected at the detector during measurement.

#### *Dead time correction*

Dead time is the time interval, between a change in the input signal or event and response to the signal.  $T$  is the dead time in equation (4.2). Dead time correction factor  $T$  is defined as:

$$T = \frac{\alpha}{\sum_x \sum_y I_s(x, y)} \quad (4.3)$$

where  $\alpha$  is the number of detected events at the anode of MWPC gas detector. Summations in the above equation are sum over all the pixels of detector. The averaged factor is in our case about 1.10. In case of the CCD detector is this effect not valid in first approximation.

#### *Dark current correction*

It is the small electric current that records when no photons are entering the detector.  $I_D$  is the dark current in equation (4.2), which has to be subtracted from the scattered intensity from the sample. Various factors are responsible for the dark current, such as electromagnetic interference from power lines, electronic noise, and cosmic radiation events in detector trigger. The dark currents for gas detectors are much lower and have long term stability than that of the CCD camera.

#### *Normalization by primary intensity*

Continuous decay of synchrotron current, leads to decay of X-ray photon flux with time. Normalization with the primary beam intensity is necessary to omit the effect of continuous decaying and potential fluctuations of photon flux with time.  $I_{os}$  is the primary intensity in equation (4.2), which is measured simultaneously with the SAXS measurements.

#### *Transmission correction*

X-ray photons not only scatter from the sample, but also they absorbed by the samples. Ratio of the transmitted photons over incident photons is termed as transmission of the sample.  $\tau_s$  is the transmission from the sample, which is measured by the following formula:

$$\tau_s = \frac{I_s^1 - I_D^1}{I_s^0 - I_D^0} \frac{I_e^0 - I_D^0}{I_e^1 - I_D^1} \quad (4.4)$$

Where  $I_s^1$  and  $I_s^0$  are the intensity measured at diode after and before the samples.  $I_e^1$  and  $I_e^0$  are the intensity measured at diode for the empty beam (no sample is present), after and before the empty sample holder. In principle the ratio of  $I_e^1$  and  $I_e^0$  must be equal to one.

$I_D^0$  and  $I_D^1$  are the intensities due to the inherent noise (dark current).  $\tau_b$  in equation (4.2) is the transmission from the background respectively

##### *Background correction*

Backgrounds can arise from sample holders, slit scattering, primary beam absorber, beamline flight tubes that means from all components in the beamline, are included in the measured scattered curves. By measuring separately the scattering of an empty sample holder or background samples (e.g. capillaries) and then subtracting it from the scattering of main samples leads to correct the background for the measurements.  $I_b$  is the background scattering from the sample holder.

##### *Detector sensitivity*

Sensitivity profile of detector is the important parameter, which has to be taken in account while correcting the two-dimensional image of detector. The sensitivity relates all detector pixels to each other in correction function. In equation (4.2),  $S(x, y)$  is the sensitivity profile by which the scattered intensity is normalized. Sensitivity is also termed as flatfield. It is mandatory to measure sensitivity for the 2D gas detector.

##### *Solid Angle Correction*

Since the detector has a flat surface while the wave reached the detector after scattering are spherical in shape, which leads to the geometrical correction of the solid angle. In equation (4.2),  $\Omega_{x,y}$  is the solid angle correction for the measurement.

##### *Calibration of $q$ value*

In order to calibrate the  $q$  values, Silver Behenate is used as a standard. Since the first peak value for scattering vector  $q=1.067\text{nm}^{-1}$  for Silver Behenate is known, by using this value we can calibrate the curves to the exact  $q$  values [66]. So the Silver Behenate standard is measured in a sample sequence with the measuring samples.

### *Normalization to Absolute value*

To evaluate the quantitative measurement, it is necessary to get the corrected intensities in differential scattering cross section per solid angle in units of  $\text{cm}^{-1}$ . Normalizing the measured sample curves with the standard sample of known scattering cross section, measured under identical conditions allow to get the curves in absolute units of cross section. In SAXS normally a glassy carbon sample of thickness  $90\mu\text{m}$  or  $1\text{mm}$  is used to normalize the curves. This standard is also measured simultaneously with the measuring samples.

All the corrections mentioned above will be done during the primary data analysis by using the software package “SASREDTOOL”.

## 4.2 SANS at ILL

### 4.2.1 Description of the beamline D22

The neutrons are coming from a cold source will be monochromatized by means of a velocity selector. A 1.2m long permanent FeSi supermirror transmission polarizer is used after the velocity selector. A schematic view of a beamline is shown in Figure 4.4. The polarizer is used to select one of the neutron spin state. A radio frequency spin flipper is used to reverse the spin state of polarized neutron and installed just before the sample [67].

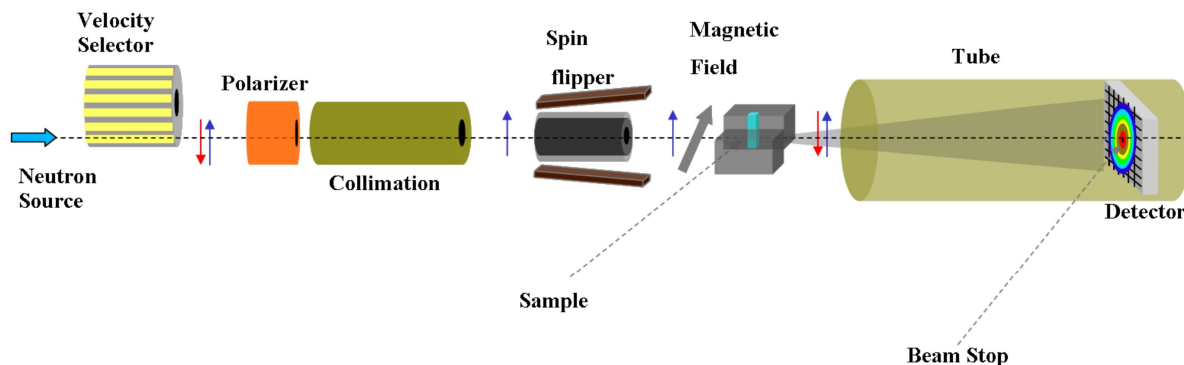


**Figure 4.4:** Schematic of polarized SANS beamline.

Neutrons having wavelength of 6 Angstrom are incident on the sample. During measurement magnetic field of 1.5 Tesla is applied perpendicular to the direction of the incident neutron beam direction. Each sample is measured twice, once with the flipper ON and once with the flipper OFF. The scattered neutrons were collected at a multi-tube detector, which is consists of  $128 \times 128$  pixels with a resolution of  $8 \times 8\text{mm}^2$ . The samples were

measured at three different detector positions, at 2m, 8m and 17.6m to achieve long  $q$  range. The raw data was corrected for background, transmission, and calibrated to absolute value of scattering cross sections. The scattered intensity contains the mixture of isotropic nuclear scattering and anisotropic magnetic scattering from the magnetic moments. In the ideal case all the magnetic moments in the sample has to be aligned with the field in the vertical direction and there should be no magnetic scattering for  $q$  vector parallel to the magnetic moments and a maximum magnetic scattered intensity for the  $q$  vector perpendicular to the moment direction. Around a circle of constant momentum vector the magnetic scattered intensity should vary as a cosine square with angle around the multi detector image. The anisotropic averaged curve provides the separate curves for the nuclear and the magnetic scattering. Measurement of the four partial neutron intensities  $I^{++}$ ,  $I^{--}$ ,  $I^{+-}$ , and  $I^{-+}$  became possible by registering all scattered neutrons independently on their polarization state after the scattering. That means no polarization analysis was done. Magnetic guide fields of the order of 1mT serve to maintain the polarization between polarizer and RF flipper.

#### 4.2.2 Data reduction / GRASP

Raw data treatment was carried out by means of the software named GRASP [68]. In GRASP one has to load the scattering data, background and cadmium data sets (for dark current) into the relevant workspace areas. For calculating transmission firstly load the transmission files and the corresponding empty cell files into the worksheets then calculate the sample transmission  $T_s$  using the graphical zoom and transmission calculator. Similarly, the empty cell transmission will be calculated. GRASP software uses the 'Centre of Mass' calculator to determine the beam centre coordinates from the zoomed area of the transmission or reference beam measurement. In order to eliminate the bad data pixels software uses the masking of the pixels which is combined with an instrumental mask that eliminates the inactive regions of the detector. For calibration and scaling, software uses a water scattering measurement as a differential scattering cross section standard. The detector efficiency calculator generates a calibration scaling value and detector efficiency map. After all the corrections the image is averaged isotropic or anisotropic depending on the scattering from the samples.

## 5 Crystallization of magnetic $\text{Mn}_x\text{Fe}_{3-x}\text{O}_4$ nanocrystals in silicate glasses

### 5.1 Motivation

Magnetic nanoparticles are abundant in nature and also present in some biological objects [69]. The development of magnetic nanoparticles has been a source of invention of spectacular new phenomena and increase the interest of the scientific community to study the fundamental properties and enhance its potential applications in different fields mainly information technology, telecommunication or medicine [70-75]. Magnetic nanocomposite materials are generally composed of magnetic nanosized particles distributed either in a non-magnetic or magnetic host matrix [76,77]. The transport and magnetic properties are depending on the distribution of magnetic nanoparticles in the host matrix. Therefore, understanding and controlling the nanostructures in materials is essential to obtain desired physical properties.

The synthesis of nanosized magnetic crystals is usually achieved by using wet chemical routes, i.e. by the precipitation of magnetite ( $\text{Fe}_3\text{O}_4$ ) [34,78,79] but also of  $\text{Co}_3\text{O}_4$  and  $\text{MnFe}_2\text{O}_4$  [80,81] from salt solutions. Magnetotactic bacteria (MTB) which has nanosized magnetite crystals covered by protein and lipid membranes where produce by the biological route [82-84]. These particles have often monodisperse size distributions and have sizes that are difficult to prepare by other chemical methods. Precipitation of magnetic nanocrystals in glass ceramics is another route to get well dispersed particles in glass matrix. The syntheses of oxide glass-ceramics containing nanosized ferrimagnetic or superparamagnetic particles are reported in the literature [85, 86]. The main problem associated with the synthesis of oxide glasses with high concentrations of transition metals using standard melting techniques is that the corresponding products may crystallize spontaneously [87-89]. This may result in uncontrolled crystallite sizes and sometimes, phase compositions [90]. The spontaneous crystallization during cooling can be avoided or reduced by adjusting the glass composition accordingly and by increasing the cooling rate. Thermal annealing for variable time periods of the obtained glasses can enable the precipitation of crystalline phases with tailored size-distribution of the particles. Magnetic nanoparticles may lead to numerous applications through variation of the matrix containing the nanoparticles. The magnetic nanoparticles in glass ceramics can have different types of magnetism behaviour such as ferromagnetism, ferrimagnetism or superparamagnetism.

The properties such as magnetic, electrical and optical of the magnetic nanoparticles are depend on many factors, the key of these includes the chemical composition, the particle size, its distribution, shape, volume fraction and on its morphology, also it depends on the interaction of the particles with the surrounding matrix and with neighbouring particles [91, 92]. One can control the magnetic and electrical characteristic of the material by varying the nanoparticle size, shape and composition. Broad variation of different properties of the nanomagnetic particle provides possibility for a large variety of applications.

Transition metals (Fe, Mn) containing silicate glass ceramics can have a possibility of precipitation of transition metal oxide nanocrystals during heat treatment. There is a formation of spherical core shell kind of structure for these particles and it is difficult to identify the complete structure and phase of particles by XRD and microscopic techniques. We have implied the ASAXS technique to determine the Fe-Mn-O ratio in nanocrystals and the composition of shell surrounds the crystalline phase.

## 5.2 Glass preparation

The base glass was produced by using reagent grade compounds of  $Na_2CO_3$ ,  $MnCO_3$ ,  $SiO_2$  and  $FeC_2O_4 \cdot 2H_2O$  [93]. The batches (100g) were homogenized and melted in  $SiO_2$ -crucibles using a  $MoSi_2$ -furnace with temperatures in the range from 1400 to 1450°C for 1.5h. After that the melt is pouring into the pre-heated graphite mould, and after 3-5min when the surface solidifies the resulting glasses were further transferred to a muffle furnace and kept at 480°C for 10min, since the glass transition temperature is  $T_g=490^\circ C$ . Then, the furnace was switched off and the samples were cooled down with furnace velocity to room temperature. The base glass used in our study has the composition as mixed 13.6 $Na_2O$ -62.9 $SiO_2$ -8.5 $MnO$ -15.0 $Fe_2O_{3-x}$  (mol %). The measured density of the glass is 2.897g/cm<sup>3</sup>. The chemical synthesis of the samples are shown in Table 6.1

**Table 5.1:** Chemical synthesis composition of the Fe-Mn-O containing glass ceramics.

Element	Weight (%)	Mol (%)
Na	7.91	8.46
Mn	6.17	2.65
Si	23.26	19.56
Fe	21.89	9.33
O	40.77	60.00

In order to get the iron and manganese containing crystals of composition  $Mn_xFe_{3-x}O_4$  the glass samples were heat treated at temperatures in the range from 500 to 700°C for different times varying from 0-300min. The heating rate from room temperature to the preferred annealing temperature was always 10K/min and the heat treatment temperature was always above the glass transition temperature  $T_g = 490^\circ\text{C}$ , for the studied samples. After annealing the samples for desired time period, they are taken out from the furnace and cooled down in air to room temperature. The samples are opaque and black in color as shown in Figure 5.1.

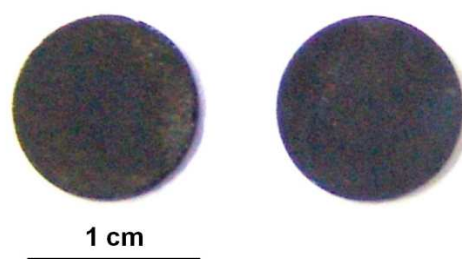


*Figure 5.1: Picture of the glass ceramics samples containing magnetic Fe and Mn oxide crystals.*

Finally the samples were polished to about 150 $\mu\text{m}$  thicknesses both sides for the SAXS and ASAXS experiments. A series of samples annealed at 540, 550 and 580°C for different time periods varying from 0-180min were used for SAXS investigation. A list of sample is given in the appendix A.1. Three samples annealed at 550°C for 40, 60 and 180 minutes have been selected for ASAXS measurement to study the nanostructure as well as their averaged chemical compositions.

### **5.3 Sample characterization using electron microscopy and X-ray diffraction**

First, microscopic measurements were made to understand the morphology of the nanoparticles. The microstructures were studied by using a scanning electron microscope (SEM: JEOL 7001F). The samples surfaces have been polished to optical quality. Secondary and back scattered electrons are used for the imaging. Figure 5.2 shows the SEM images of the sample heat treated at 550°C for 180min [93]. The SEM shows nearly spherical particles with an unimodal size distributions.

Another sample was annealed at higher temperature and for higher times. The sample annealed at 600°C for 16h shows the formation of two types of nanocrystalline phase as

shown in Figure 5.3 [93]. The images show that there is a formation of large ellipsoidal crystals of a second phase  $NaFe(SiO_3)_2$  having size in the range of 1 micrometer, along with a population of smaller crystals with the mean size of 50nm as similar to those in Figure 6.2.

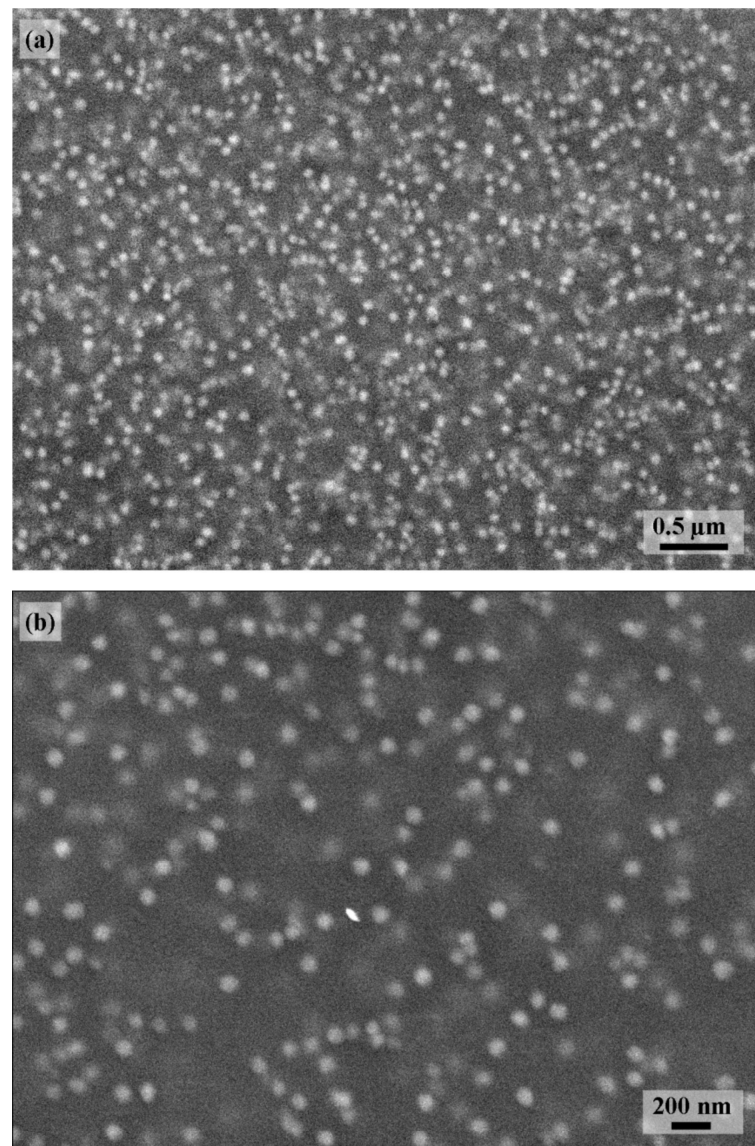


**Figure 5.2:** Scanning Electron Microscopy (SEM) image for the sample annealed at 550°C for 180min (a) 0.5 $\mu$ m (b) 200nm [93].

SEM revealed the formation and growth of nanoparticles in the glass ceramics. However, SEM is not able to distinguish between amorphous or crystalline particles. Therefore, XRD measurements were done on a series of samples. Moreover, it is assumed that  $Mn_xFe_{3-x}O_4$  phase will crystallize, but the exact ratio of Fe and Mn is not known.

The XRD measurement was performed on the samples at 7T-MPW-SAXS beamline at BESSY II. The glass samples were also examined by SAXS and ASAXS methods. The measurement was done in the transmission geometry. During the measurement, X-ray of energy 17keV (wavelength  $\lambda = 0.073$ nm) was used, which was appropriate for achieving

suitable transmission from the samples. The X-ray beam incident perpendicularly on the sample and interacts with the distribution of electrons and scatters in all directions. The scattered photons were collected at the MAR CCD 165 camera having pixel size of  $79\mu\text{m} \times 79\mu\text{m}$ . During measurement the sample was stationary and the detector was collecting the photon at three different positions  $15^\circ$ ,  $35^\circ$  and  $55^\circ$ . A gold foil was measured with the samples was used to calibrate the XRD- $2\theta$  values in a range from  $10^\circ$  to  $60^\circ$  [94].

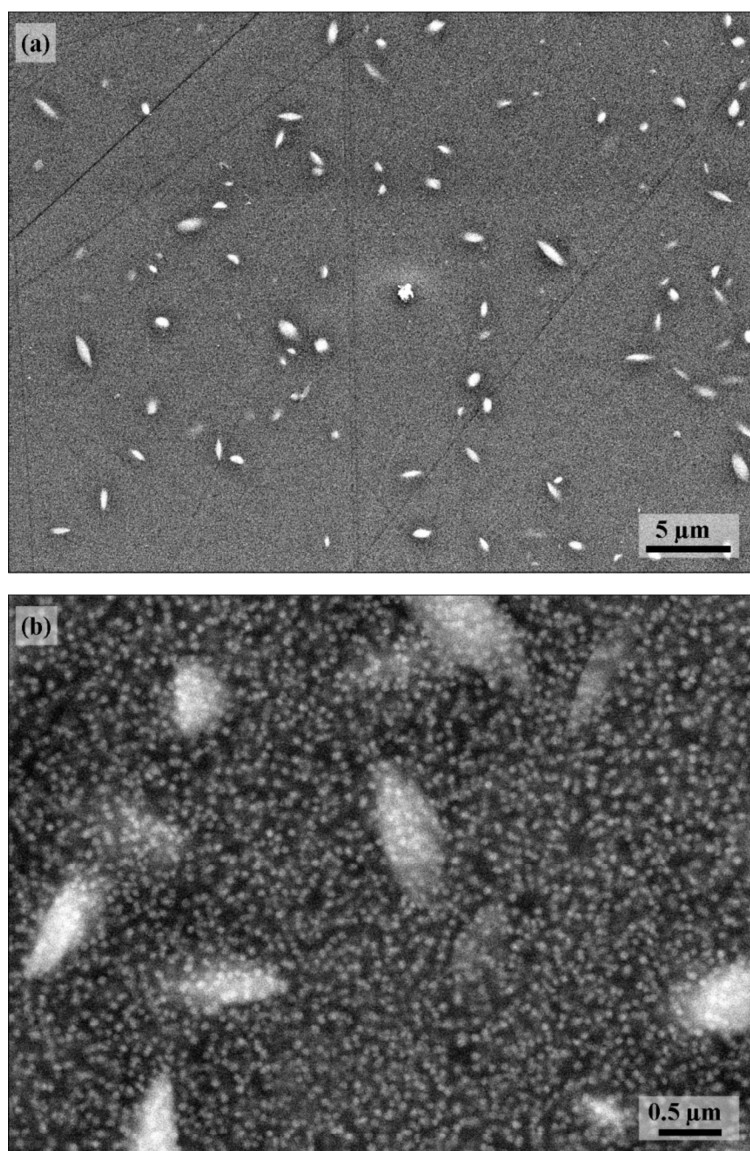


**Figure 5.3:** SEM image for the sample annealed at  $600^\circ\text{C}$  for 16h at different resolution (a)  $5\mu\text{m}$  (b)  $0.5\mu\text{m}$  [93].

Figure 5.4 shows the XRD curves measured on an unannealed sample and on the samples annealed at  $550^\circ\text{C}$  for 10, 40, 60 and 180min. XRD shows no peaks for unannealed and for the sample annealed for 10min. While for the samples, which were annealed for more than 10min pronounced peaks at about  $20^\circ$ ,  $28.5^\circ$  and  $50^\circ$  are clearly detectable.

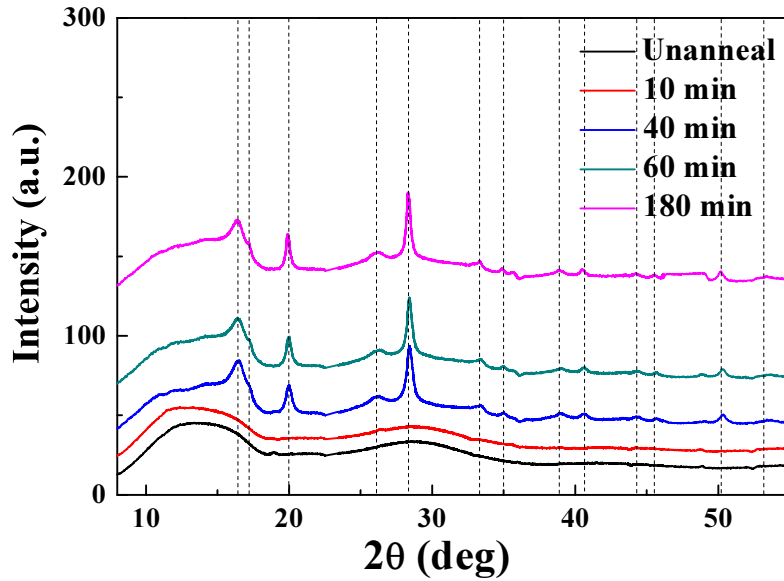


**Figure 5.4:** X-ray diffraction of the sample annealed at 550°C for unannealed, 10, 40, 60 and 180min.

For analyzing the phases, annealed samples were fitted with different standard phases of iron and manganese oxide. XRD fit results shows the formation of particles having a mixed phase of Fe and Mn oxides as  $Mn_xFe_{3-x}O_4$  and it is difficult to distinguish between  $Fe_3O_4$  and  $MnFe_2O_4$  (jacobsite) phases. However, in some cases e.g. of a solid solution containing two or more transition metal are difficult to characterize by XRD. This is due to the insufficient separation between the main diffraction peaks of two nanocrystalline phases due to relatively low intensity of the peaks and by the nano dimension of the particles that broadens the peaks. In such cases, XRD is not able to provide the precise phase of the nanocrystalline particles.

In XRD the broadening of peak decreases with the annealing time, which shows increase in the particle size with time of heat treatment as evaluated by Debye Scherer equation.

$$T = \frac{K\lambda}{\beta \cos \theta} \quad (5.1)$$

where  $T$  is the mean size of the crystalline domains,  $K$  is the shape factor,  $\lambda$  is the X-ray wave length,  $\beta$  is the line broadening at half the maximum intensity (FWHM) in radians and  $\theta$  is the Bragg angle. The shape factor  $K$  has a typical value of about 0.9, but varies with the actual shape of the crystals. The FWHM was determined by fitting the peaks at 20°, 28.5° and 50° by Gaussian fit, which fits well with the peaks. The fit for one of the sample annealed at 550°C for 40min and for the peak at 20° is shown in the Figure 5.5. The error for the particle size is calculated by the equation (5.2):

$$T_{Error} = T \sqrt{\left(\frac{d\beta}{\beta}\right)^2 + (\tan \theta)^2 d\theta^2} \quad (5.2)$$

where  $T_{Error}$  is the error for the particle size,  $d\beta$  is an error in FWHM, and  $d\theta$  is an error of the Bragg angle. By using Scherer equation, particle size between 10-30nm was evaluated as shown in Figure 5.6.

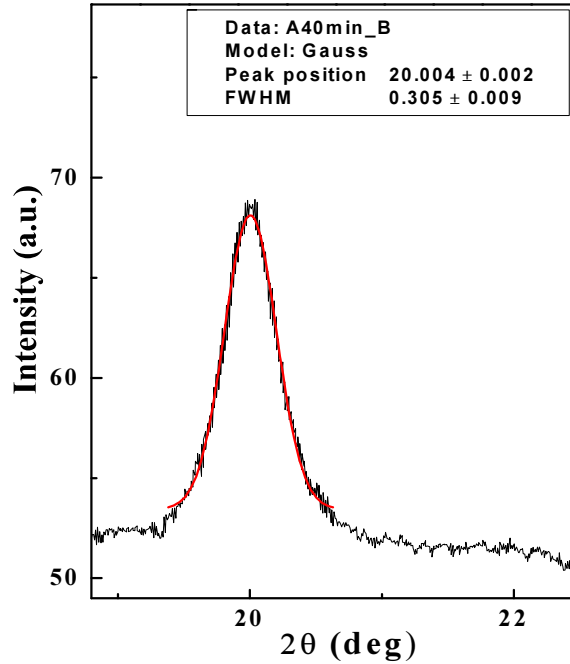


**Figure 5.5:** Gaussian fit for the peak at  $20^\circ$  for the sample annealed at  $550^\circ\text{C}$  for 40min. The inset shows the parameter after the fit.

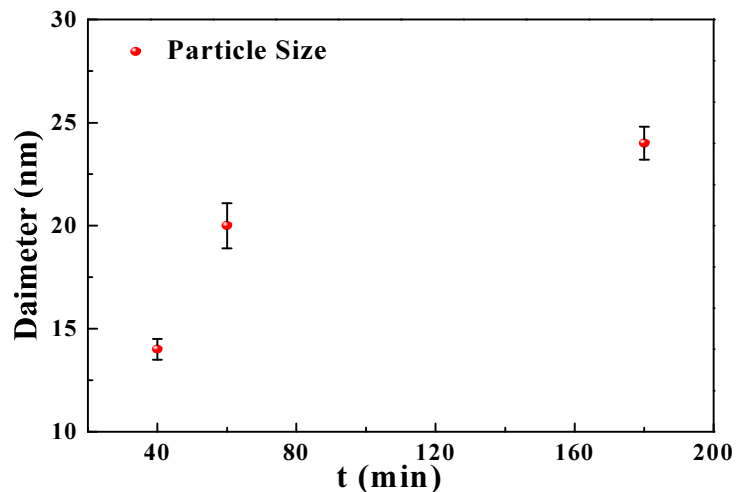


**Figure 5.6:** Size of the particles calculated by XRD using the Debye Scherer equation

Furthermore, in order to investigate the effect of heat treatment on the shape, size, volume fraction and distribution of the particles in the glass matrix, the samples were studied

by SAXS and the composition is determined by analysing the ASAXS curves. The volume studied in the SEM is much smaller ( $<1\mu\text{m}^3$ ) than in the SAXS/ASAXS experiments ( $>0.1\text{mm}^3$ ) and therefore a much better average and a more reliable statement for the macroscopic sample is given in these experiments. XRD measurements delivers the average sizes of the crystalline phases by Scherer equation, but it is not able to provide any information about the amorphous phases present in the system. To get a comprehensive size distribution we performed the SAXS investigations.

#### 5.4 SAXS study of heat treated sample series

To investigate the nanostructure and its size distribution in the glass matrix, SAXS technique was chosen. The SAXS measurement was performed at 7T-MPW SAXS beamline at BESSY II. Since the X-ray K-absorption edges of Fe and Mn are at 7112eV and 6539eV, we have chosen a X-ray energy of 6047eV for the SAXS measurement which is sufficiently below the X-ray absorption edges of both the elements, so the fluorescence will be avoided. For collecting the scattered photons a 2D delay-line gas detector with pixel size of  $207\mu\text{m} \times 207\mu\text{m}$  was used. The scattered photons were collected at two different distances, one far from the sample at about 3800mm and other close to the sample at about 850mm to get the whole reachable  $q$  range of the instrument. The glass-ceramic samples were measured in transmission geometry. Samples were mounted on a sample changer together with a standard samples. The sample chamber was under vacuum conditions ( $10^{-3}$  mbar) to avoid air scattering. All the samples were measured together with the background scattering, with a glassy carbon standard for differential scattering calibration and with the silver behenate for calibrating  $q$  values. The data reduction was done by using the software SASREDTOOL.

Figure 5.7 shows measured SAXS curves calibrated to differential scattering cross section ( $\text{cm}^{-1} \text{sr}^{-1}$ ), as a function of magnitude of the scattering vector  $q$ . The SAXS Figure shows that the intensity of the scattering curves increases with annealing time. The unannealed sample shows the small hump at about  $q=0.8\text{nm}^{-1}$  which is shifted towards the lower  $q$  value for the 10min annealed sample. Both samples have a slope of about  $q^{-4}$  at smallest  $q$  values, which is coming from nanosized surface structures. For longer time annealed samples for 40, 60 and 180min, the scattering intensities are increasing significantly and two humps can be seen in the Figure, which gives a first hint for the presence of nanostructures of spherical core shell or two different kinds of particles, also the shoulders are shifting towards lower  $q$  values with annealing time, which implies the growth of the particles. In Figure 5.7 slope of the scattering

curves approached a  $q^{-4}$  behavior at higher  $q$  values larger than  $q=1\text{nm}^{-1}$ . This implies for the smooth surface of the particles.

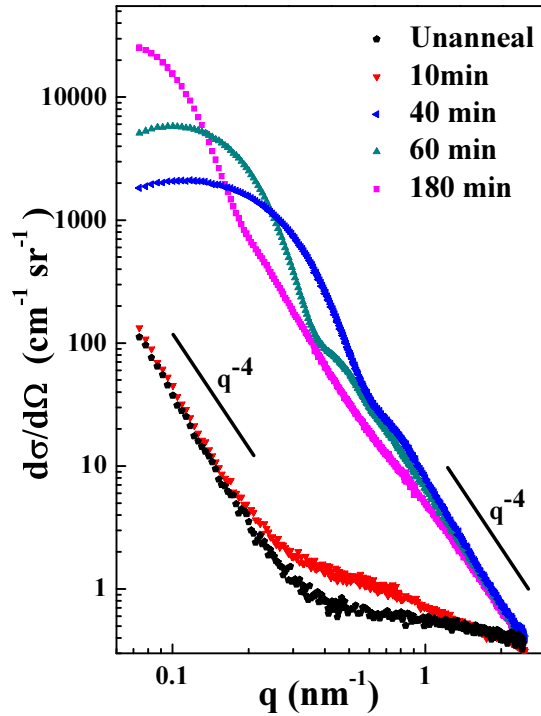


**Figure 5.7:** SAXS curves measured at 6047eV for the samples as prepared and annealed at 550°C for 10, 40, 60 and 180min. The slope of the scattering curves approached a  $q^{-4}$  at a higher  $q$  values for annealing time larger than 10 minutes.

The SEM investigations gave a hint that the nanocrystals are almost spherical. Since the SAXS curves show a pronounced shoulder, a spherical core shell structure seems to be performed. Typically for particle growth process in an amorphous matrix, the particles will have a lognormal size distribution. With these starting assumptions the SAXS scattering curves in Figure 5.7 can be fitted well. To evaluate the structural information from the scattering curves, they were fitted with equation (3.8) by assuming first a spherical core-shell model by using program SASfit. The fitted SAXS curves annealed at 550°C for 40, 60 and 180min is shown in the Figure 5.8. Since the particles has higher volume fraction, structure factor has to be considered by assuming local monodisperse approximation, which accounts for the inter particle interaction. The lognormal size distributions are shown in the Figure 5.9 which reveals that the particle sizes are increasing with the annealing time and the sample annealed for longer time has a broader size distribution than the sample annealed for shorter times.

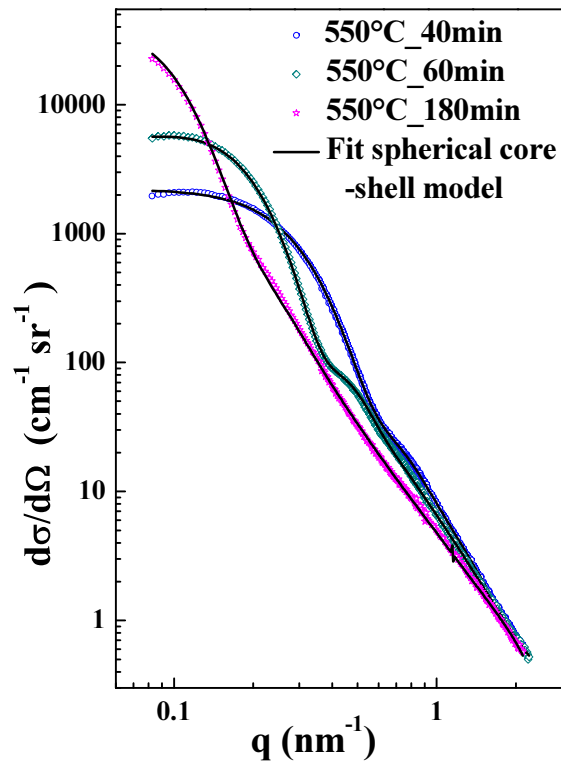


**Figure 5.8:** SAXS curves measured at 6047eV for three samples annealed at 550°C for 40, 60 and 180min. The fits using a spherical core shell model are shown by straight black line.

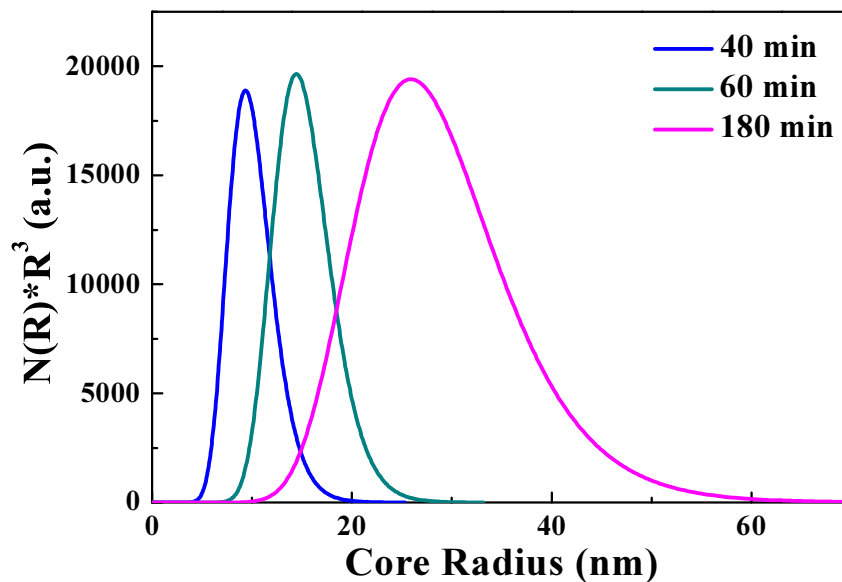


**Figure 5.9:** Volume weighted size distributions of the core radii for the particles in the samples annealed at 550°C for 40, 60 and 180min.

The XRD results revealed the formation of  $Mn_xFe_{3-x}O_4$ , because of its high mass density these particles must have the highest electron density as shown in Figure 5.10. Contrast parameters from the SAXS curve fitting between core-shell and matrix, shows that electron

density of core has highest and the shell has the lowest electron density with respect to the matrix as shown in Figure 5.10. Therefore, the electron density profile reveals that the particles are surrounded by the layer dominated by elements whose electron density is smaller than that of the remaining glass matrix. In our case, Si is the most prominent element expected to be present in the layer and furthermore acts as a diffusion barrier for further diffusion of the nanocrystals forming elements Fe and Mn. This layer grows with increasing the annealing time and may slows down further crystal growth Table 5.2.

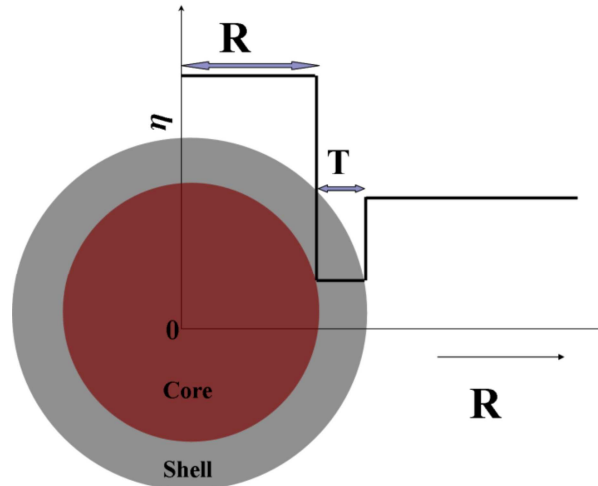


**Figure 5.10:** Sketch of variation of electron density for a spherical core shell model.

Table 5.2 shows the parameters obtained after the fitting of the three SAXS curves. Parameters reveal an increase of particles diameter from 14nm up to 44nm after 180min of annealing and also the thickness of shell increases with annealing time up to 2.2nm.

**Table 5.2:** Resulting parameters for the SAXS curves fitted by spherical core shell model for the samples annealed at 550°C for 40, 60 and 180min.

Parameter	40min	60min	180min
Averaged Core Radius (nm)	$7.1 \pm 0.5$	$11.9 \pm 0.5$	$22.0 \pm 1.0$
Averaged Shell Thickness (nm)	$1.1 \pm 0.2$	$1.7 \pm 0.2$	$2.2 \pm 0.2$

On the other hand it turned out that the same SAXS curves can also be fitted with the two size sorts of spheres model without any surrounding shell or diffusion region. The resulting fit parameters are also nearly the same as for the spherical core shell model. Figure 5.11 shows

the curves fitted with the two sphere model. The deviation of the fitted lines are in the same order as for the core shell model as shown in Figure 5.8 The size distributions of two sorts of spheres are shown in the Figure 5.12, which shows the distribution of two types of particles. Table 5.3 shows the averaged size parameters after fitting the scattering curves by two sphere model.

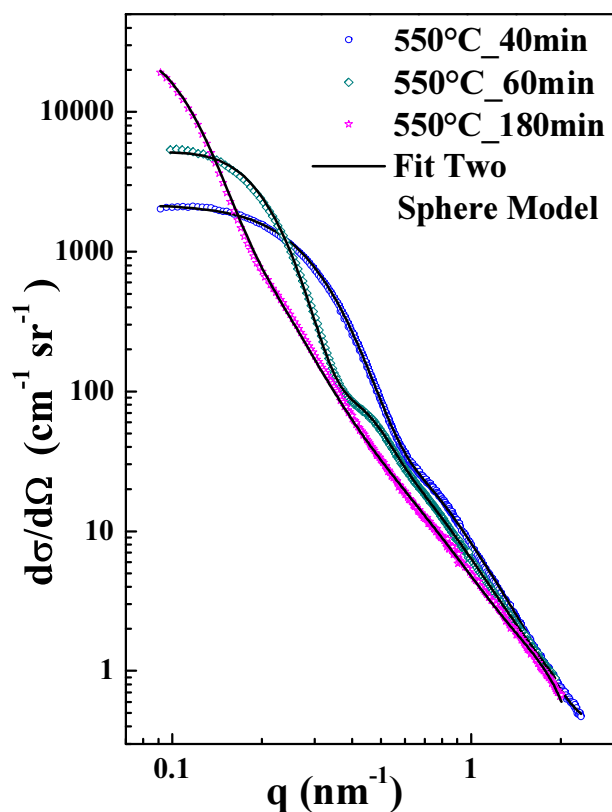


**Figure 5.11:** SAXS curves measured at 6047eV for the sample annealed at 550°C for 40, 60 and 180min fitted with a model of bimodal distribution.

**Table 5.3:** Resulting parameters for the SAXS curves fitted by two sphere model for the samples annealed at 550°C for 40, 60 and 180min.

Parameter	40min	60min	180min
Average Particle 1 Radius (nm)	$6.8 \pm 0.5$	$11.7 \pm 0.5$	$22.2 \pm 1.0$
Average Particle 2 Radius (nm)	$1.3 \pm 0.2$	$1.8 \pm 0.2$	$2.3 \pm 0.2$

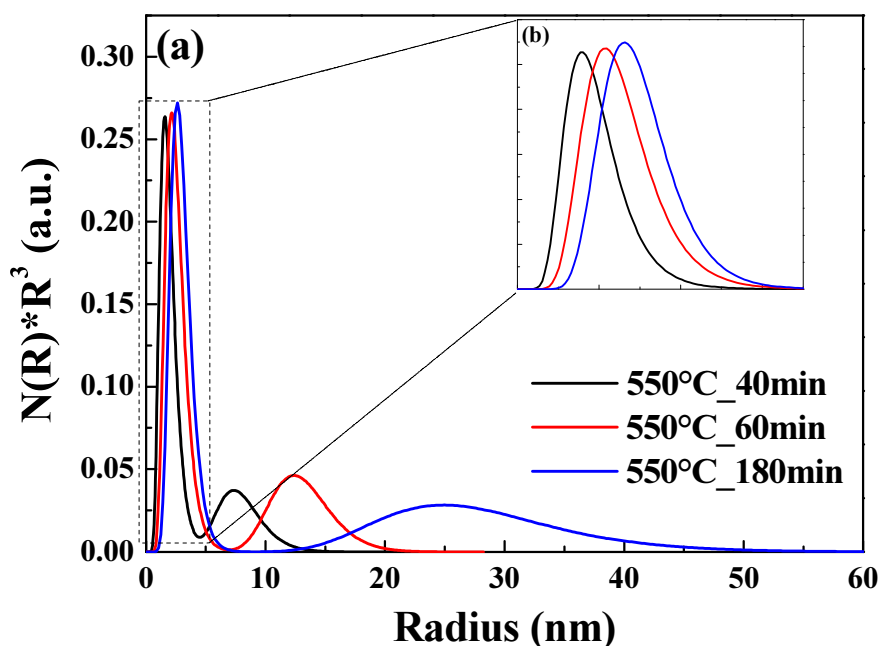


**Figure 5.12:** Bimodal size distributions for the samples annealed at 550°C for 40, 60 and 180min fitted with a model of two sorts of independent spherical particles. Enlarge image for the distribution of the small sorts of particles are shown in fig (b).

The comparison of the sizes determined by XRD using the Debye Scherrer equation and by SAXS (core shell model) shows that, both methods deliver similar averaged sizes upto 60min of annealing. At 180min the XRD diameter is much smaller, because XRD measures correlation lengths, this is a direct hint that the crystals become polycrystalline for longer annealing times (180min) as shown in Figure 5.13.

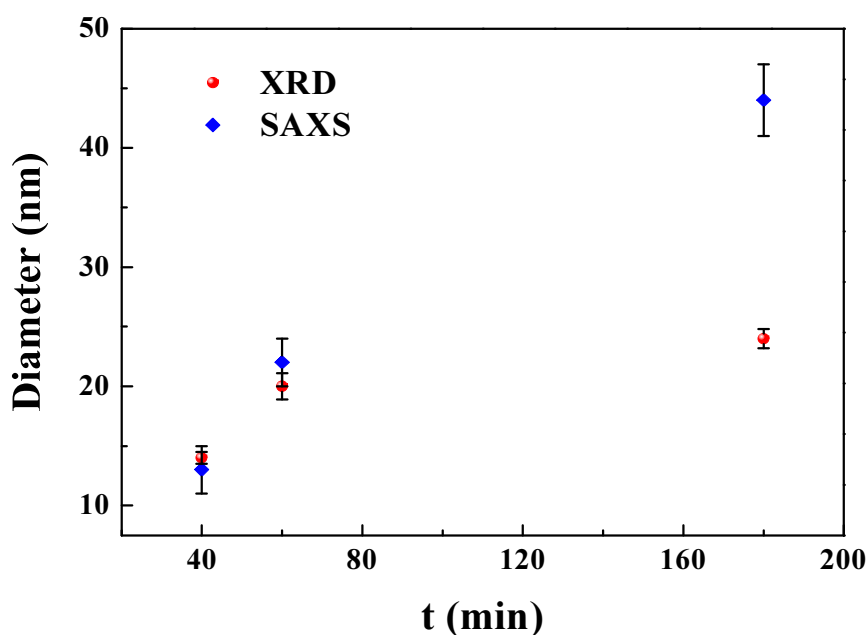


**Figure 5.13:** Comparison of the particle sizes as calculated by SAXS (spherical core-shell model) and XRD.

The parameters shown in Table 5.2 for the spherical core shell model and in Table 5.3 for the two sphere model are comparable to each other; also the fits are similar to each other. Since both the spherical core shell and two sphere model fit to the curves; this makes it difficult to distinguish between both the models. Such type of unsolved question remained as already reported earlier for the SANS measurements [95].

## 5.5 Investigation of magnetic nanostructure using polarized SANS

Glasses that contain transition metals have the possibility to be magnetic in nature. The sample studied contains a large amount of iron and manganese. This large amount of transition elements makes this material to be magnetic. While SAXS resulted in two different competing structural models and one could not decide, which one is the appropriate model. Here SANS was apply with polarized neutrons to overcome this contradiction. The reason to choose this method is that XRD revealed the formation of crystalline particles of a mixed composition of  $Mn_xFe_{3-x}O_4$ . Depending on the crystalline size they are superparamagnetic or become ferromagnetic while growing.

The polarized SANS measurements were performed on the studied samples annealed at different temperatures from 540-580°C for different times from 0-300min. The samples had thicknesses between 800 $\mu$ m to 2000 $\mu$ m, which is roughly the optimal thickness for the SANS measurement. A list of measured sample is given in appendix A.2. The SANS experiment was performed at the D22 SANS beamline at the Institute Laue-Langevin (ILL), Grenoble France [67]. In a polarized SANS experiments on magnetic materials one can observe a pronounced anisotropic signal for  $I^+$  (ON) and  $I$  (OFF) polarization states of neutrons as shown in Figure 5.14 (a) and (b) as an example for the sample annealed at 550°C for 60min.

The difference between both the states ( $I^+ - I$ ) shows the cross terms and has a negligible intensity along the direction of the magnetic field as shown in Figure 5.14 (c). This is an evidence that the magnetic moments in the sample are very well oriented in magnetic field direction. Therefore, it is not necessary to take a magnetization orientation distribution (Langevin function) into account. The anisotropic average of the above images is shown in the Figure 5.15, which shows only a small difference between the two polarization states, while the interference term has an intensity that is about 10 times lower than both polarization states. The cross term shows the interference between the nuclear and magnetic form factors. The value of the cross term equals to zero, when the magnetic form factor of a given particles will not interfere with the nuclear form factor of a particles [7].

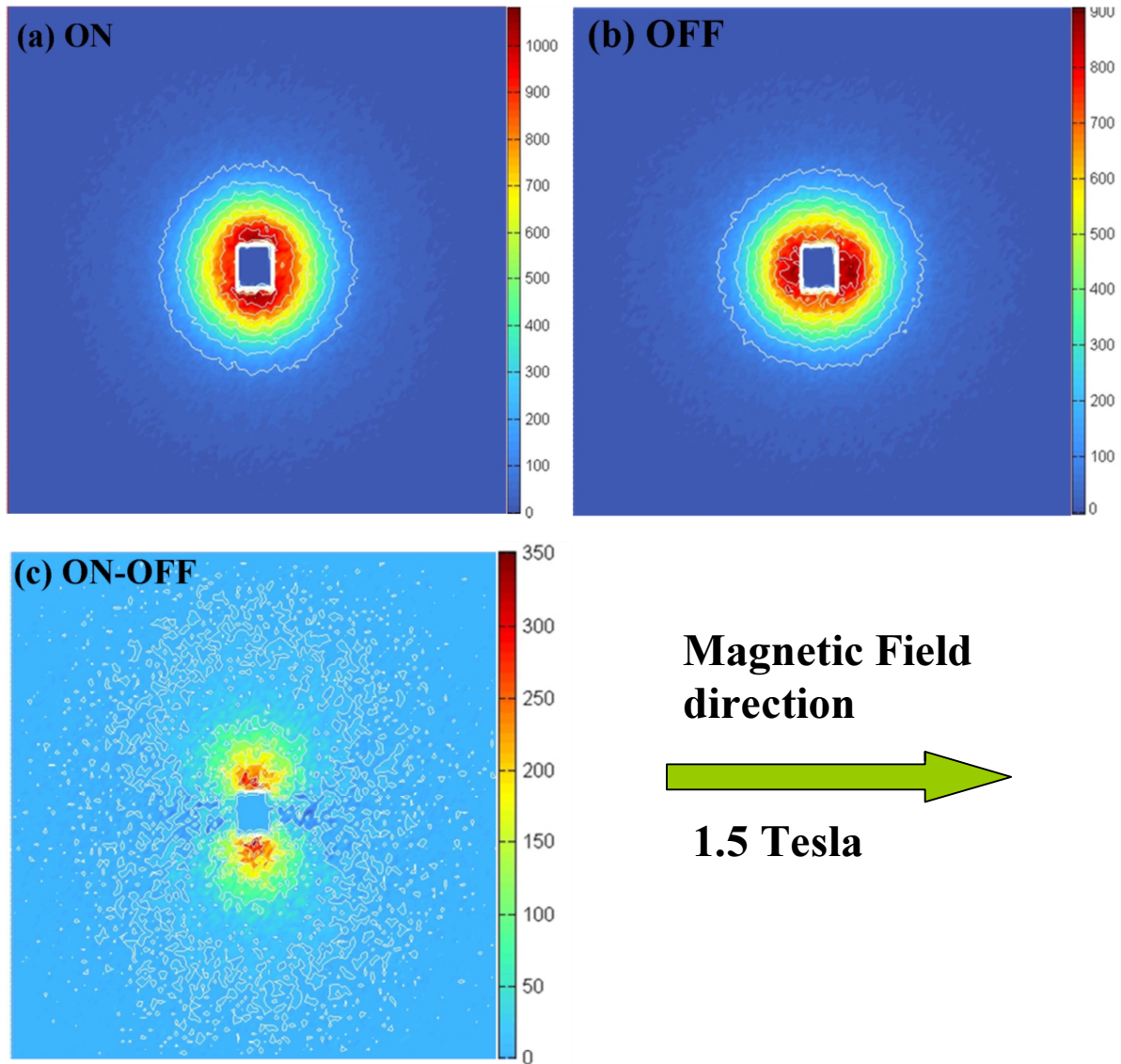


**Figure 5.14:** 2D detector scattering images from the polarized SANS experiment after the data correction for the sample annealed at 550°C for 60min. The applied magnetic field of 1.5Tesla is applied in the horizontal direction.

The images in Figure 5.14 reveal that by using polarized neutron scattering one can separate the magnetic scattering from the nuclear scattering. The nuclear scattering  $A(q) = F_N^2$  is extracted by analyzing the scattering intensity  $I^+$  and  $I^-$  and the magnetic scattering is determined by using the cross term represent as  $B(q)$  and the nuclear part as  $F_M^2 = B(q)^2 / [A(q)^2 4P^2 (1+e)^2]$ . Figure 5.16 shows the separated magnetic and nuclear scattering for one of the studied sample. The pronounced amount of magnetic scattering shows the magnetic behavior of the sample.

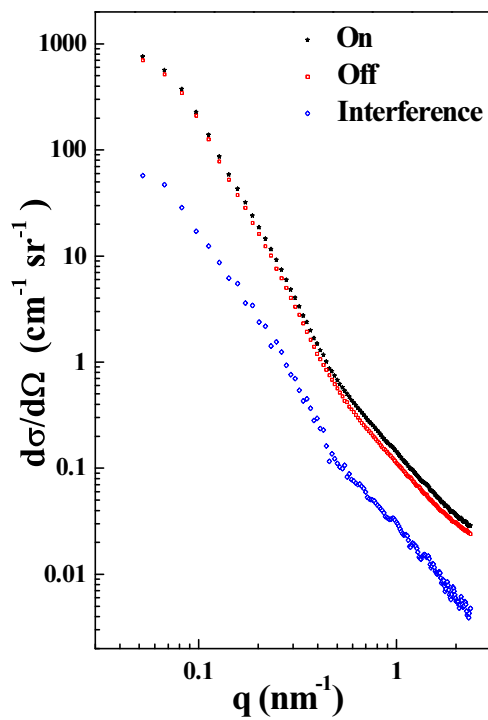


*Figure 5.15: Scattering curves for the ON, OFF and the cross term from the images for the sample annealed at 550°C for 60min.*

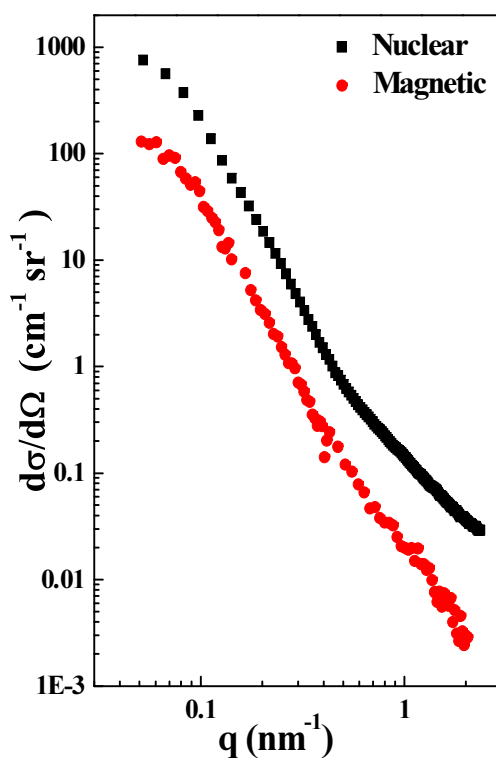


*Figure 5.16: Separated nuclear and magnetic scattering curves for the sample annealed at 550°C for 60min.*

Similarly the data reduction was performed on a series of samples annealed at the temperature range from 550-580°C for 0-180 minutes (see the list in appendix A.2). Figure 5.17 shows the nuclear and magnetic scattering curves for the samples annealed at 550°C for variable time periods from 10 to 180min. The scattering intensity increases with the annealing time which reveals the growth of the particles. In order to evaluate the structural information about the particles like size, shape and its distribution, the curves were further fitted with the theoretically calculated intensity by using equation (3.8) and by the program SASfit [62]. On the basis of structural information from SAXS in section 5.4, a spherical core shell model and a model with two sorts of particles was taken into account. For such a glass system that undergoes a growth process of nanocrystals, it is known that a log normal distribution model is appropriate.

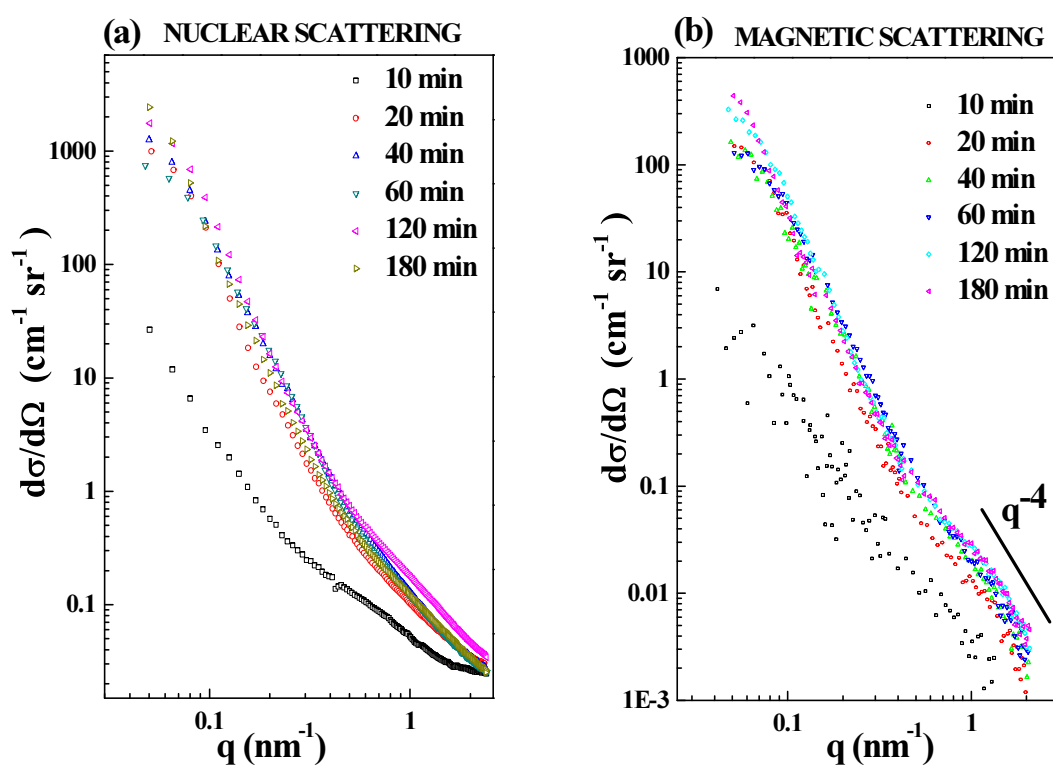


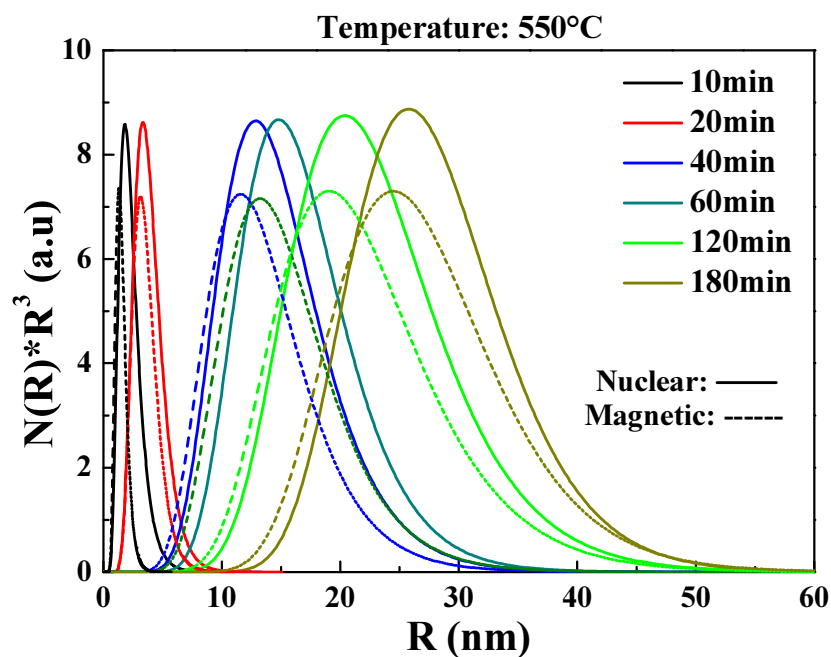
**Figure 5.17:** (a) Nuclear scattering (b) Magnetic scattering for the sample heat treated at 550°C for 10 to 180min. for the SANS measurement.

While fitting the nuclear scattering curves that fit well with the spherical core shell model and the magnetic curves fits well with the normal sphere model. Table 5.4 shows the size parameters obtained after the fitting of the respective SANS curves for the sample heat treated at 550°C for different times from 10 to 180 minutes. Parameters reveal increase in the size of particles as well as the thicknesses of the shell with annealing time. Distribution of particles is also an important parameter while studying the kinetics of the crystal growth in this glass-

ceramic matrix. Figure 5.18 shows the volume weighted size distribution of particles evaluated after fitting the scattering curves for the samples annealed for 550°C at different time periods from 10min to 180min. The size distributions derived from magnetic scattering curves revealed peaks at smaller radii in relation to those from nuclear scattering curves. The smaller radii of magnetic nanocrystals indicate the presence of a magnetic surface dead layer that surrounds the magnetically active core of the crystals [96]. The important result is (Table 5.4) that the magnetic scattering revealed only one sort of spherical particles. These magnetic particles have a slightly smaller size as the core in case of the nuclear scattering, that could modeled by spherical core shell model. While comparing the sizes given by the nuclear and magnetic scattering in Table 5.4, one has to conclude that one sort of magnetic crystals are formed having a non magnetic shell like region. These results provide a confirmation of formations of a spherical core shell kind of magnetic nanoparticles in the glass matrix.

**Table 5.4:** Averaged size parameters calculated by polarized SANS from the nuclear and magnetic scattering for the samples annealed at 550°C for 10 to 180min.

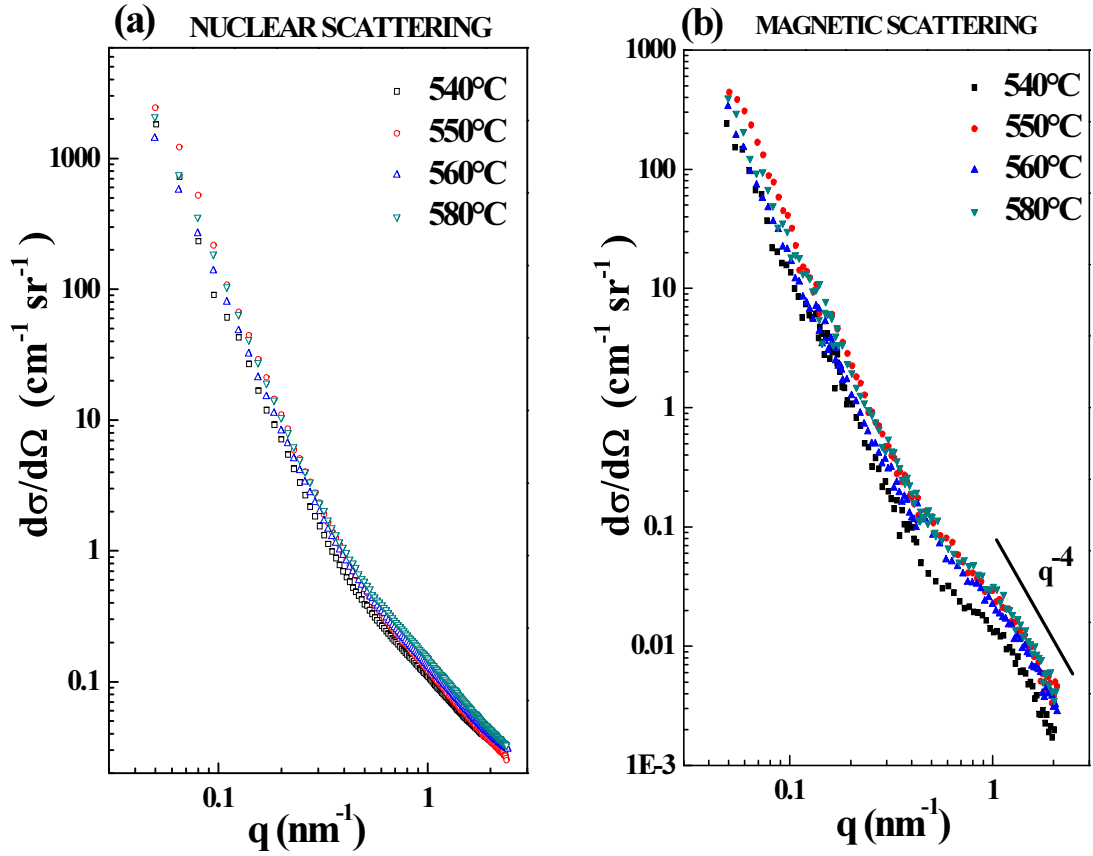
Sample 550°C	Nuclear Scattering		Magnetic Scattering
	Average Radius Particle (nm)	Average Thickness Shell (nm)	Average Radius Particle (nm)
10 min	1.4	---	1.3
20 min	2.8	0.4	2.7
40 min	10.0	1.0	9.8
60 min	11.5	1.5	11.4
120 min	16.2	1.8	16.2
180 min	22.0	2.2	22.0



**Figure 5.18:** Volume weighted size distribution curves for the samples annealed at 550°C for a duration varying from 10 to 180min for nuclear and magnetic scattering. It can be seen that the magnetic size distributions (dashed line) are smaller in comparison to the nuclear one (solid line). The magnetic size distribution curves are scaled down for good visibility.

Similarly, polarized SANS measurements were performed on the samples heat treated at four different temperature, but annealed always for 180 minutes. The nuclear and magnetic scattering curves for the samples annealed at different temperature from 540°C to 580°C for 180min are shown in Figure 5.19.

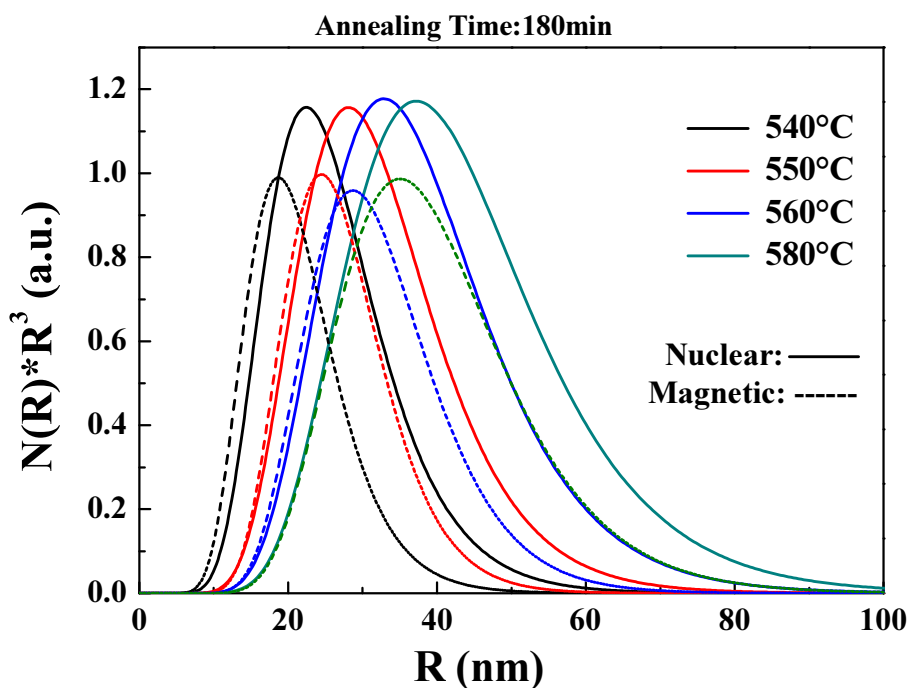
The intensity of the scattering increases with the annealing temperature, which shows the growth of the particles with the temperature. Structural information was evaluated by fitting the nuclear scattering curves by spherical core shell model and the magnetic curves by simple sphere model. The fit parameters are shown in Table 5.5 and the respective size distribution is shown in Figure 5.20. Also this sample set; annealed at different temperature, prove the core shell structures.



**Figure 5.19:** (a) Nuclear scattering (b) Magnetic scattering for the sample heat treated for 180min at different temperature for the SANS measurement.

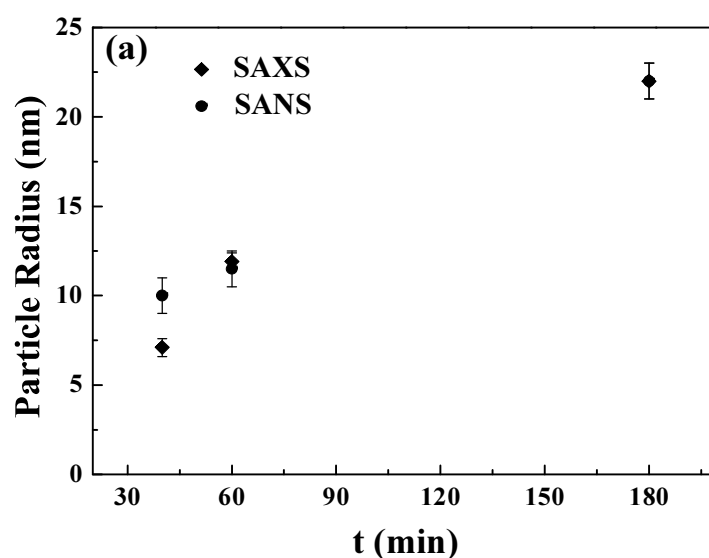
**Table 5.5:** Parameters calculated by polarized SANS for nuclear and magnetic scattering for the samples annealed for 180min at different temperatures.

Sample 180 minutes	Nuclear Scattering		Magnetic Scattering
	Average Radius Particle (nm)	Average Thickness Shell (nm)	Average Radius Particle (nm)
540°C	16.5	2.5	16.2
550°C	22.0	2.2	22.0
560°C	25.9	1.9	25.5
580°C	30.4	1.4	30.4



**Figure 5.20:** Volume weighted size distribution curves for the sample annealed for 180min at different temperatures from 540 to 580°C for nuclear and magnetic scattering represented by the same color. The magnetic curves are scaled down for good visibility.

The size parameters reveal that the sizes of the particles are increases and the thickness of layer decreases for the sample annealed at higher temperature for a particular time period. Earlier, SAXS measurements were performed on these sample and the structural parameters were evaluated by fitting the scattering curve by spherical core shell model. Figure 5.21 shows the comparison of the average size and thickness of the layer evaluated by SANS and SAXS measurements.



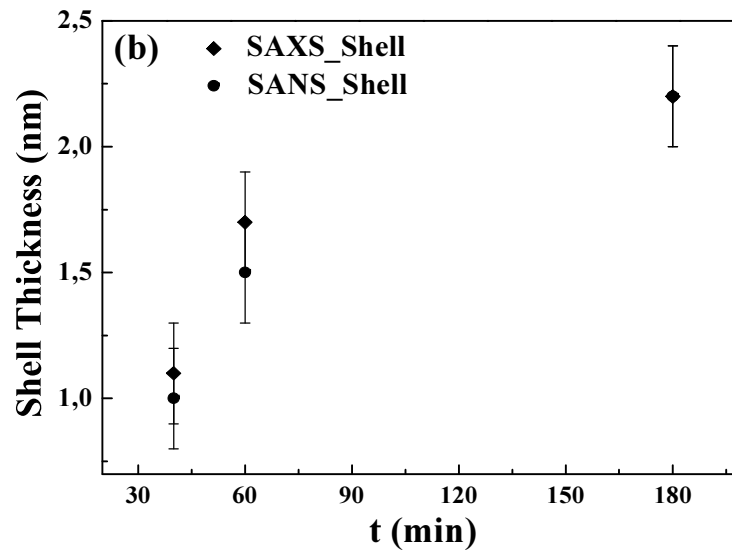


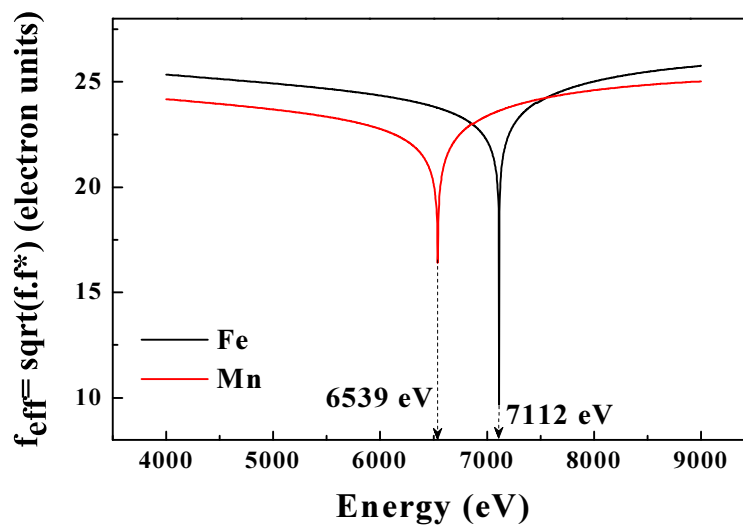
**Figure 5.21:** Comparison of SAXS and SANS parameters for the sample annealed at 550°C for 40, 60 and 180min (a) Particle Size (b) Shell Thickness.

## 5.6 ASAXS study at the absorption edge of Fe and Mn

ASAXS technique was applied to get additional information about the compositions of phases and particular element distribution in the glass matrix, respectively. Figure 5.22 shows the variation of effective atomic scattering amplitudes near the X-ray  $K$  absorption edges of Fe and Mn. The equation for the effective atomic scattering amplitude is given by:

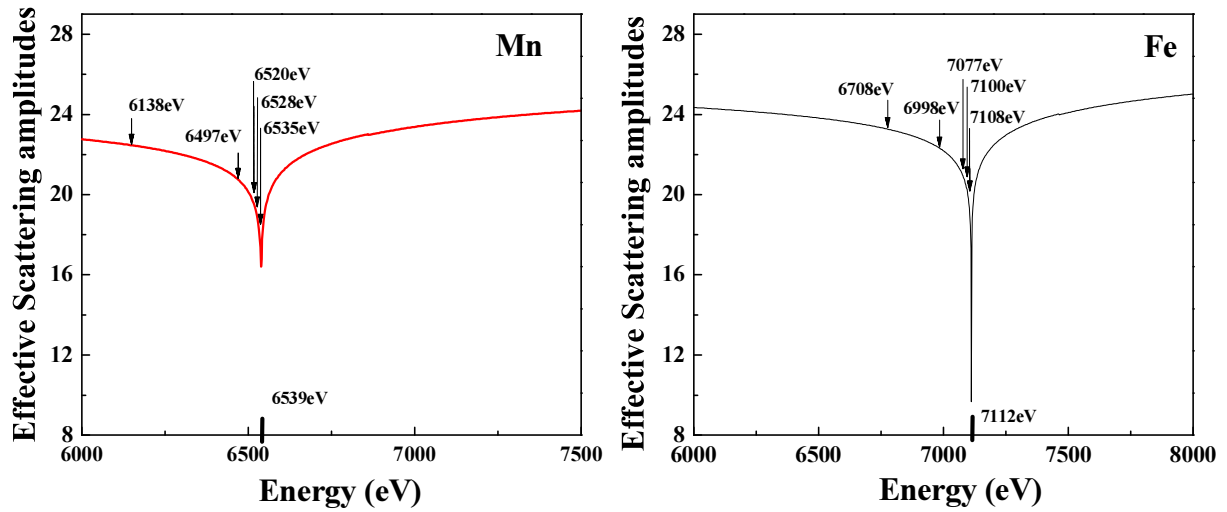
$$f_{eff} = \sqrt{f^*(E)f(E)} \quad (5.3)$$

where  $f(E)$  is the scattering factor defined in equation 3.16 (section 3.3).



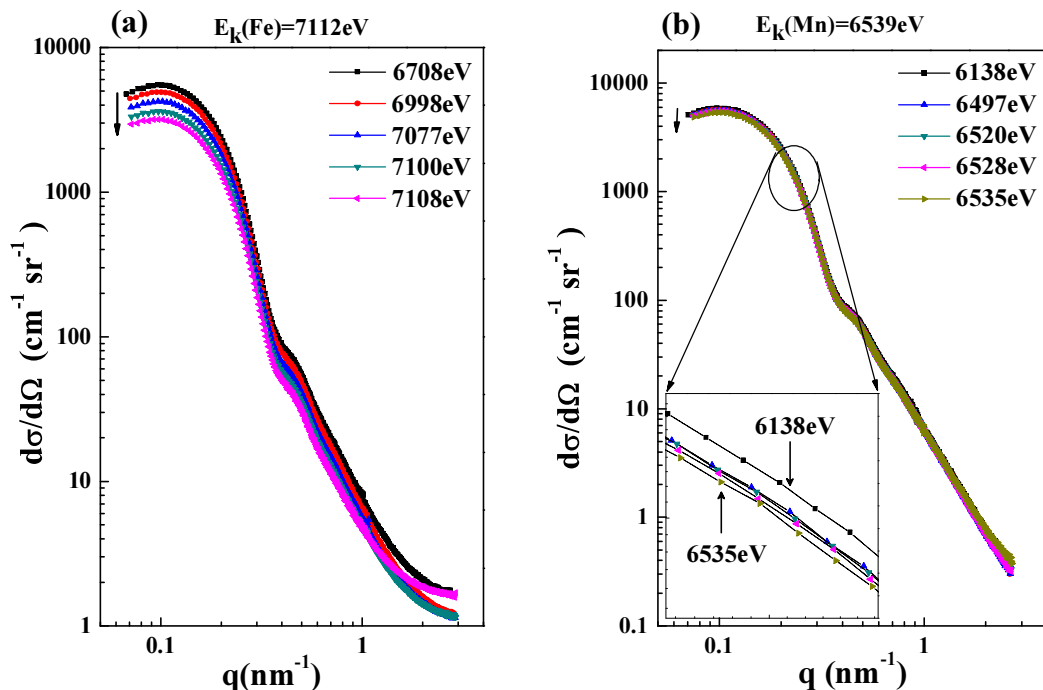
**Figure 5.22:** Effective atomic scattering amplitudes for the elements Fe and Mn.

ASAXS measurements were performed on the samples that are already investigated by SAXS by choosing five energies close to X-ray absorption edge of the elements iron and manganese as shown in Figure 5.23.



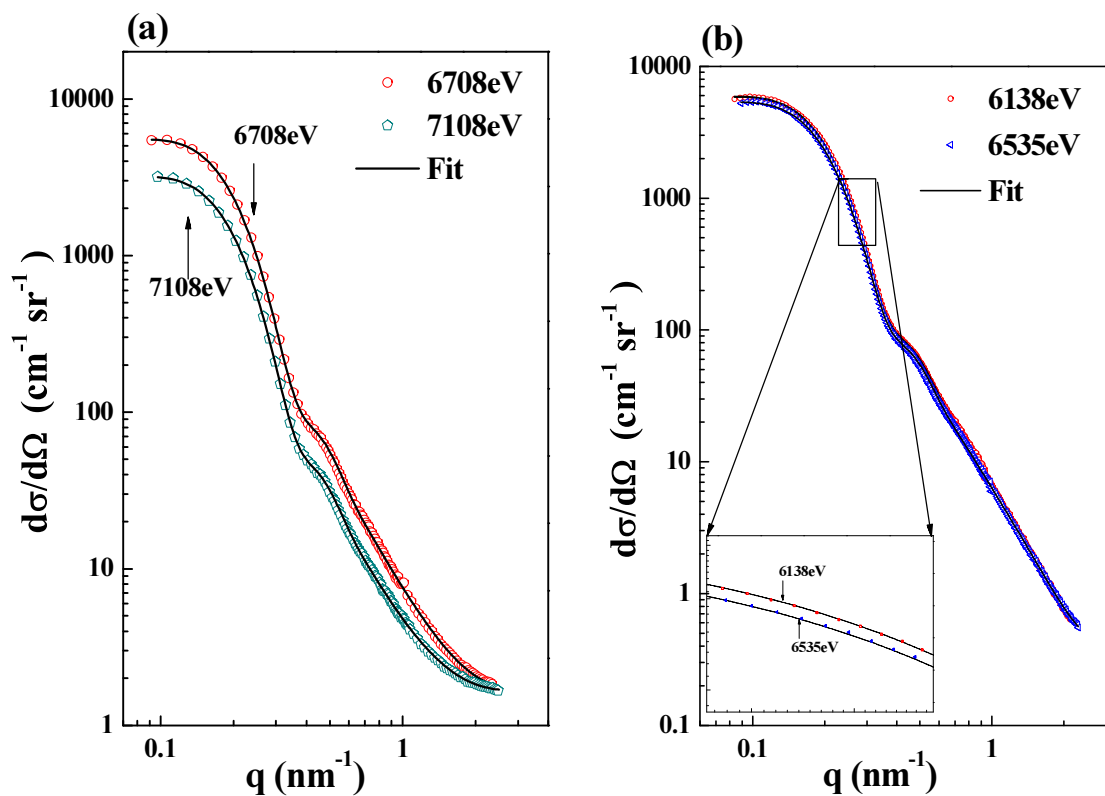
**Figure 5.23:** Effective atomic scattering amplitudes for the elements Fe and Mn. Arrows indicate the energies used for ASAXS measurements.

Figure 5.24 (a) and (b) shows the ASAXS curves measured at the Fe and Mn edge for the sample annealed at  $550^{\circ}\text{C}$  for 60min. It is seen from the Figure 5.24 (a) that for the iron edge the ASAXS effect varies larger than the manganese edge in Figure 5.24 (b), which reveals the fluctuation of higher concentration of Fe between the crystals, the shell region and the glass matrix and is more pronounced than that in case of manganese.



**Figure 5.24:** ASAXS curve for sample annealed at  $550^{\circ}\text{C}$  for 60min measured near but below the X-ray absorption edges (a) Fe K-edge and (b) Mn K-edge.

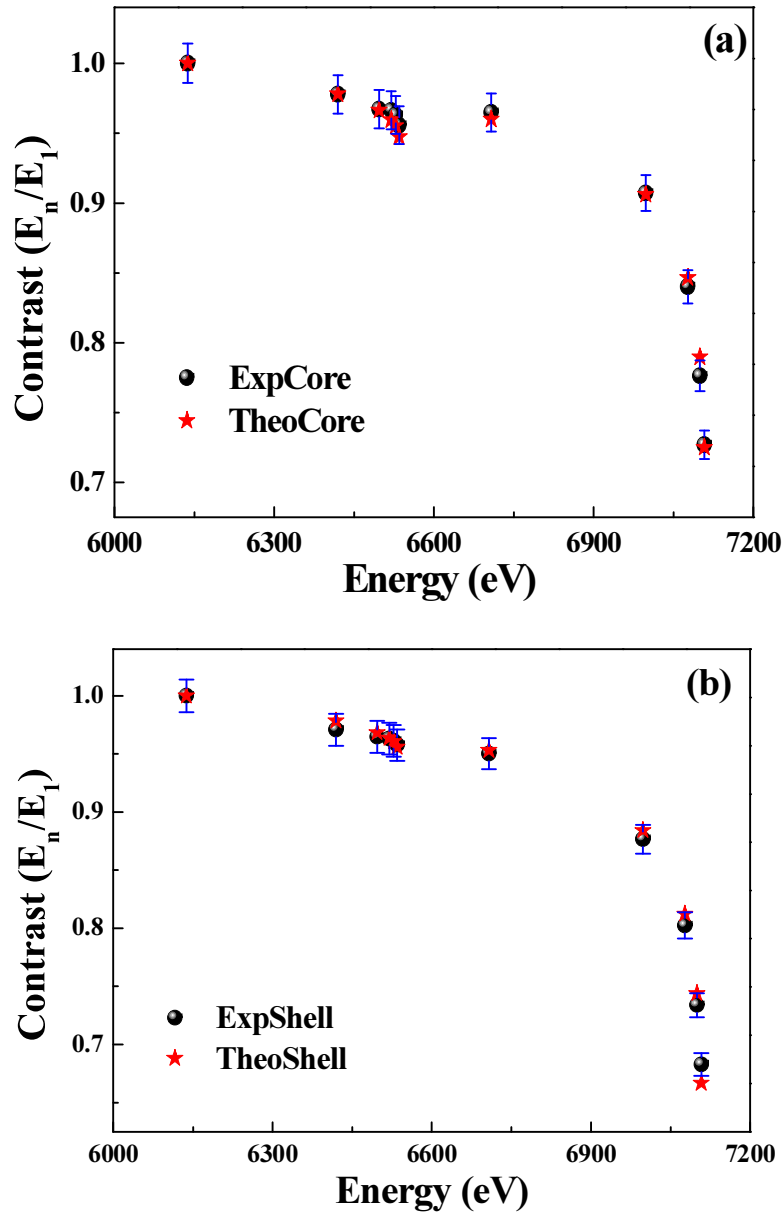
On the basis of structural model informations from SANS investigations, the ASAXS scattering curves were fitted by applying the spherical core-shell model and assuming a lognormal size distribution. During fitting all the structure determining parameter such as particle number, sizes, distribution function parameters ( $N$ ,  $R$ ,  $\sigma$ ) were fixed and only the contrast for shell and core were used as a free variables [97]. Figure 5.25 (a) shows that the fitted ASAXS scattering curves at two energies, (far and close) at the Fe absorption edge for one of the sample annealed at 550°C for 60min. Similarly for the same sample, fitted ASAXS scattering curves at Mn absorption edge is shown in Figure 5.25 (b).



**Figure 5.25:** ASAXS curves for the sample annealed at 550°C for 60min near the K absorption edges (a) Fe (7112eV) (b) Mn (6539eV).

The experimental contrasts values obtained after fitting ASAXS scattering curves, were further used for evaluating composition, density and volume fraction of the respective phases (core, shell and matrix) present in the glass sample after heat treatment. The experimentally evaluated contrasts were fitted with the theoretically calculated contrasts for core, shell and remaining matrix by using equations (3.22-3.25) as discussed in section 3.4. During fitting  $Mn_xFe_{3-x}O_4$  phase was assumed as a phase formed in core, where  $x$  is a fitting variable along with the density of the core, shell and matrix. During fitting the numbers of atoms were distributed in core, shell and matrix in such a way that the total number of atoms for each

element must be conserved. Figure 5.26 shows the comparison of the relative contrasts calculated theoretically with the experimentally evaluated contrasts for both Fe and Mn edges.

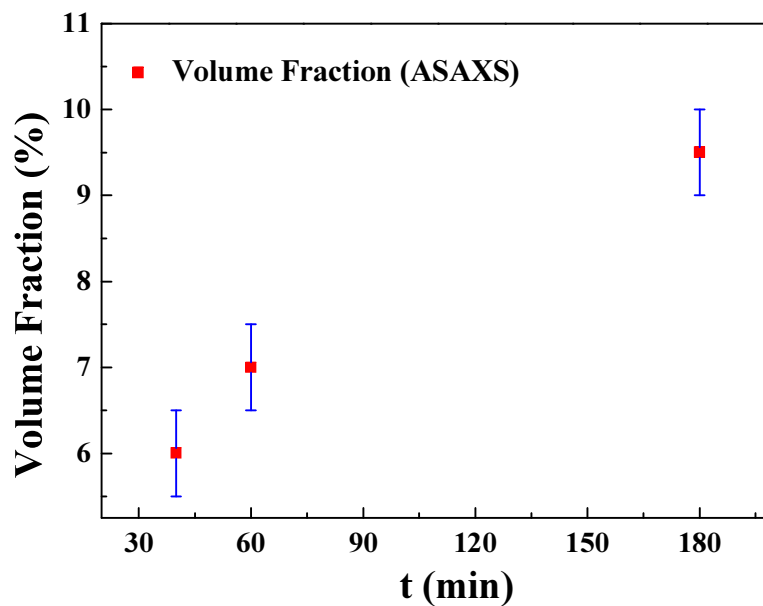


**Figure 5.26:** Comparison of the relative contrast calculated theoretically with the experimentally evaluated contrast for both Fe and Mn edges (a) Core (b) Shell.

Table 5.6 shows the resulting parameters obtained after fitting routines for all the three annealed samples. The respective parameters show that the density of core is about  $4.9 \pm 0.1 \text{g/cm}^3$  and for shell around  $2.2 \pm 0.05 \text{g/cm}^3$  and for remaining matrix is  $2.39 \pm 0.02 \text{g/cm}^3$ . Also the parameters reveal an increase in the value of volume fraction for particles from 6% to 9% during the heat treatment for long time periods. Variation of volume fraction evaluated by composition with the annealing time is shown in Figure 5.27.

**Table 5.6:** Resulting parameters for the ASAXS for the samples annealed at 550°C for 40, 60 and 180min.

Parameter	550°C_40min	550°C_60min	550°C_180min
Averaged Core Radius (nm)	$7.1 \pm 0.5$	$11.9 \pm 0.5$	$22.0 \pm 1.0$
Averaged shell thickness (nm)	$1.1 \pm 0.2$	$1.7 \pm 0.2$	$2.2 \pm 0.2$
Density Core ( $g/cm^3$ )	4.91	4.91	5.0
Density Shell ( $g/cm^3$ )	2.22	2.24	2.26
Density Matrix ( $g/cm^3$ )	2.38	2.40	2.40
Density System ( $g/cm^3$ )	2.89	2.89	2.89
Volume Fraction Particle	$\sim 6 \pm 0.5$	$\sim 7 \pm 0.5$	$\sim 9.5 \pm 0.5$
Fe atoms in particle (%) (Composition)	$\sim 55$	$\sim 62\%$	$\sim 80\%$
Fe atoms in particle (%) (Resonant curve)	--	$\sim 60\%$	$\sim 82\%$

**Figure 5.27:** Volume fraction variation with the annealing time for the samples annealed at 550°C as calculated from ASAXS.

Evaluated density of shell from fitting is close to the bulk density of  $SiO_2$  ( $2.2g/cm^3$ ) which provides direct hint of presence of  $SiO_2$  in shell. Table 5.7 shows the phases formed at core, amount of  $SiO_2$  in shell and the remaining composition left as a glass matrix. Quantitative information evaluated from the compositions shown in Table 5.6 and Table 5.7 reveals increase in the amount of Fe atoms along with the Mn atoms and the amount of  $SiO_2$  in shell with the annealing time.

**Table 5.7:** Composition calculated from ASAXS for the samples annealed at  $550^\circ C$  for 40, 60 and 180min.

Sample ( $550^\circ C$ )	Core	Shell ( $SiO_2$ )	Matrix
40 min	$Mn_{0.2}Fe_{2.8}O_4$	36%	$69.19SiO_2-15.28Na_2O-7.49Fe_2O_3-8.04MnO$
60 min	$Mn_{0.35}Fe_{2.65}O_4$	55%	$70.86SiO_2-15.88Na_2O-6.81Fe_2O_3-6.45MnO$
180 min	$Mn_{0.5}Fe_{2.5}O_4$	65%	$75.97SiO_2-17.08Na_2O-2.82Fe_2O_3-4.13MnO$

Pure resonant scattering contribution of the Fe atoms in the particles has been separated from the total scattering SAXS curves by using the Stuhrmann equation (3.20) [98]. Figure 5.28 shows the resonant curves calculated by the Stuhrmann equation at the Fe edge for the samples annealed at  $550^\circ C$  for 60 and 180min fitted with spherical core shell model, resonant curve for sample treated for 40min was very noisy, so it was excluded. Spherical core shell fit reveals the presence of iron in both in the particle and the surrounding shell. From these resonant curves, by evaluating the resonant invariant, the number density of Fe atoms in the respective formed particles was calculated by using equation (3.21) [99]. ASAXS data analysis in Table 5.6 reveals that concentration of Fe atoms in core increases up to 80% with the annealing time, which is comparable to the concentration of Fe atoms calculated by resonant curves.

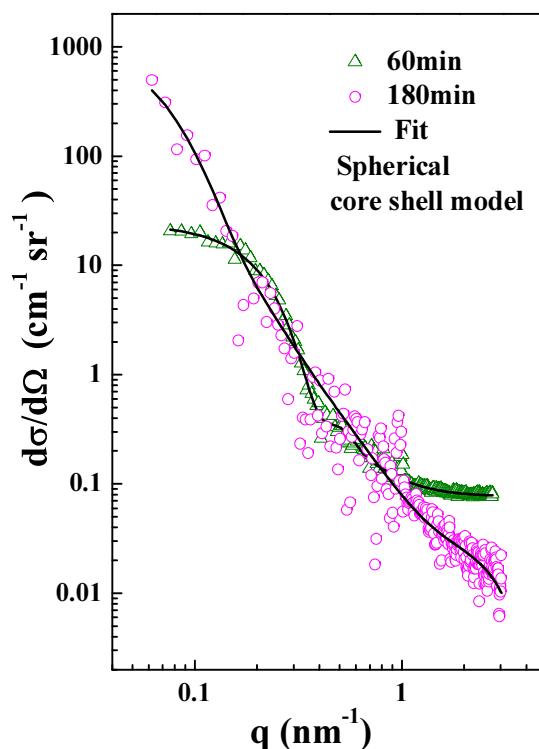
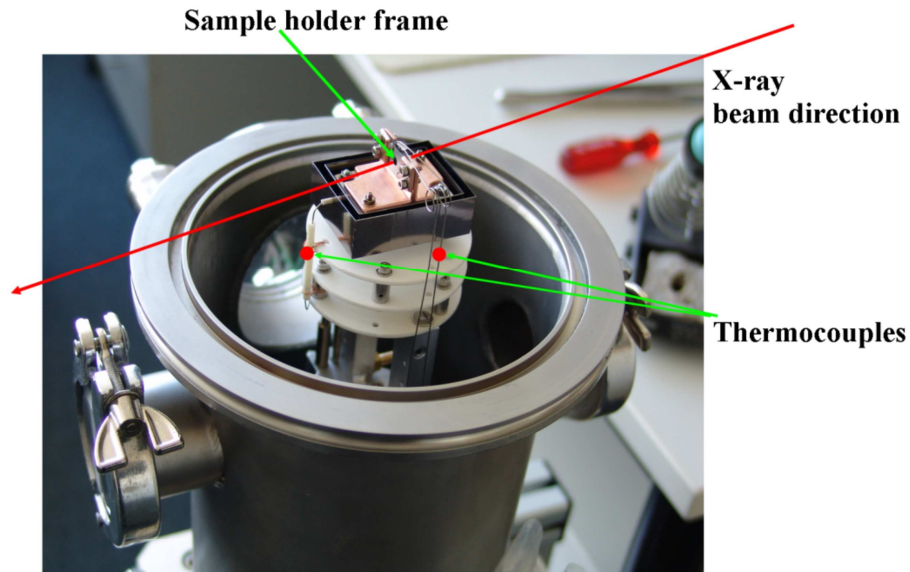


**Figure 5.28:** Resonant curves for the Fe edge ASAXS calculated by Stuhrmann method and fitted with spherical core shell model

## 5.7 Kinetics of phase formation as studied in situ

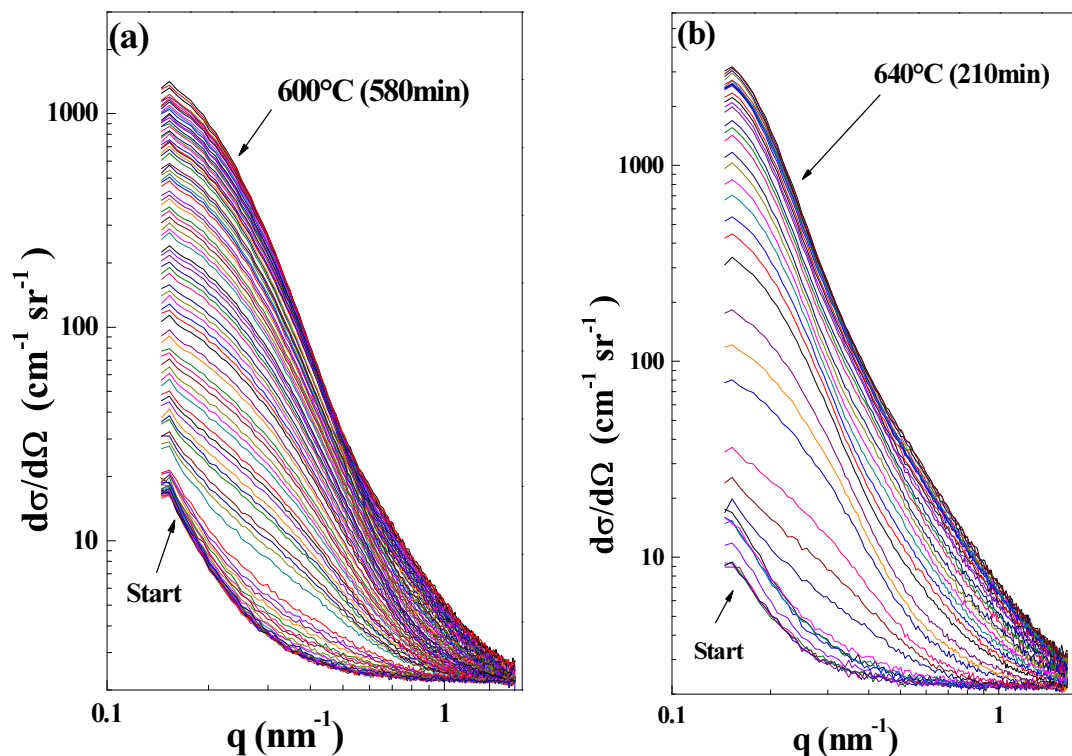
Up to now all investigations to resolve the core-shell like structure of the magnetic nanocrystals as well as their compositions were done at three samples annealed at 550°C for 40, 60 and 180min. In this chapter the kinetics of phase formation and its growth should be investigated in more detail by using in situ SAXS measurements.

The experiments were done under vacuum conditions ( $10^{-3}$ mbar) using a small furnace on top of a sample changer with the reference samples (Figure 5.29). The ceramics samples are mounted in a metal frame (Figure 5.29) that is fixed in a copper frame direct attached to the ceramic heater for a good thermal contact and for fast temperature setup times. Moreover, at least three thermocouples are used to control the temperatures.



**Figure 5 29:** Picture of the furnace used for the insitu SAXS measurements installed on top of a sample changer with the reference samples. During the experiment the chamber is under vacuum conditions.

SAXS measurements were done at 12keV at the longest sample to detector distance possible for the instrument at 3850mm, to measure the low  $q$  range. A single exposure took two minutes. Empty beam and standard samples were measured in between the sample measurements for subtracting the background from the measured curves and for calibrating them to differential scattering cross sections.



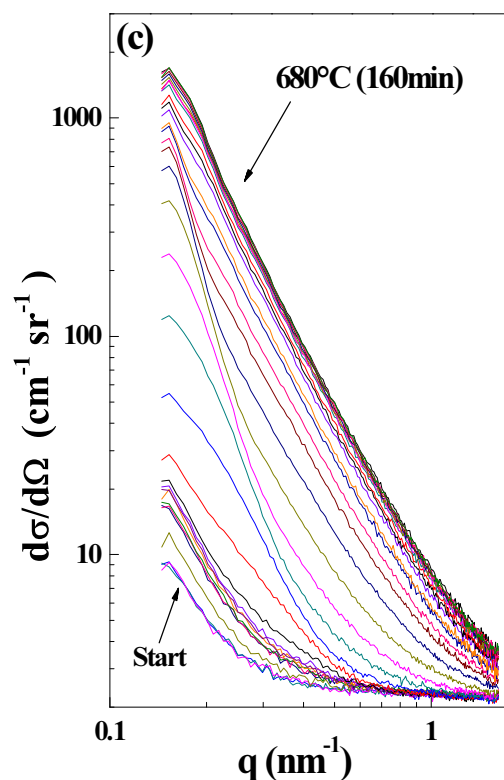


**Figure 5.30:** In situ SAXS curves measured at different temperatures (a) 600°C, (b) 640°C, (c) 680°C. Just after reaching the final temperature the first measurement was done and marked with “start”. While annealing the scattering cross section increases at all  $q$ -values and the final annealing time is marked.

Three in situ experiments at temperatures of 600°C, 640°C and 680°C were done. All scattering curves at all three temperatures are increasing monotonically during annealing, as shown in Figures 5.30 (a-c). Because the curves are measured equidistantly in time it can be seen that the intensity increase slows down after a certain annealing time. That means a growth stop or slowing down appears. The time after that the last curve is measured is indicated in the Figures 5.30. From that it is also evident that the growth rate increases with the annealing temperature. The observed growth stop appears earlier in case of higher temperatures. Furthermore, if one compares the shape, especially of the long annealed scattering curves, between the different temperatures, than it can be seen that these curves are more straight at higher temperature. This reveals larger particles at higher temperature are appearing. These qualitative findings can be summarized as follows: The higher the temperature the faster is the nanoparticle growth process, the earlier the growth stops and the particles are larger.

To determine the structural information from the curves, out of all the three measured temperature curves, the sample measured at 640°C was chosen, and further fitted with the SASfit software. Following the results from SANS and ASAXS it is evident that particles

with a shell region must be formed. This could be proved. Therefore, all curves could be fitted by exact this structural model. The quality of the resulting fit can be seen in Figure 5.31 at scattering curves chosen with an annealing time difference of ten minutes.

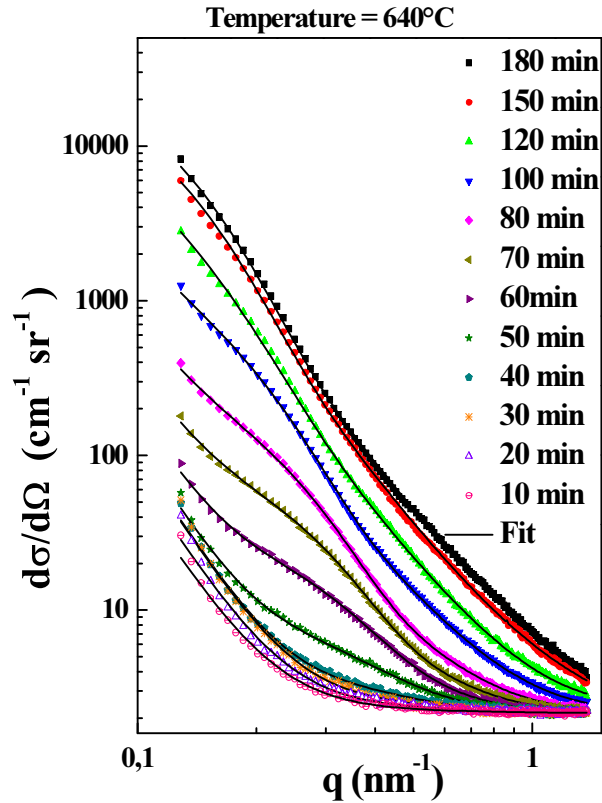


**Figure 5.31:** Fitted in situ SAXS measurement at 640°C for variable time period from 0-180 minutes.

From the fit, one can determine the structural parameters as, size of the particles (core), thicknesses of the shell region and the particle number. Figure 5.32 (a) shows the variation of the particle (core) radius with the annealing time from 10 to 180min at the annealing temperature of 640°C. It can be identified an increasing sizes with time. From about 30 to 100 minutes, the sizes are increase with about  $(t^{1/2})$  and after that with about  $(t^{1/3})$ .

The variation of the shell thickness with the annealing time is shown in the Figure 5.32 (b). The Figure shows a growth of the shell thickness with the annealing time. Figure 5.32 (c) shows the variation of the particle number with the annealing time, which shows that the number of particles decreases with the annealing time. These findings are not typical for a diffusion limited growth process or for an Ostwald ripening process. And will give raise for further studies.

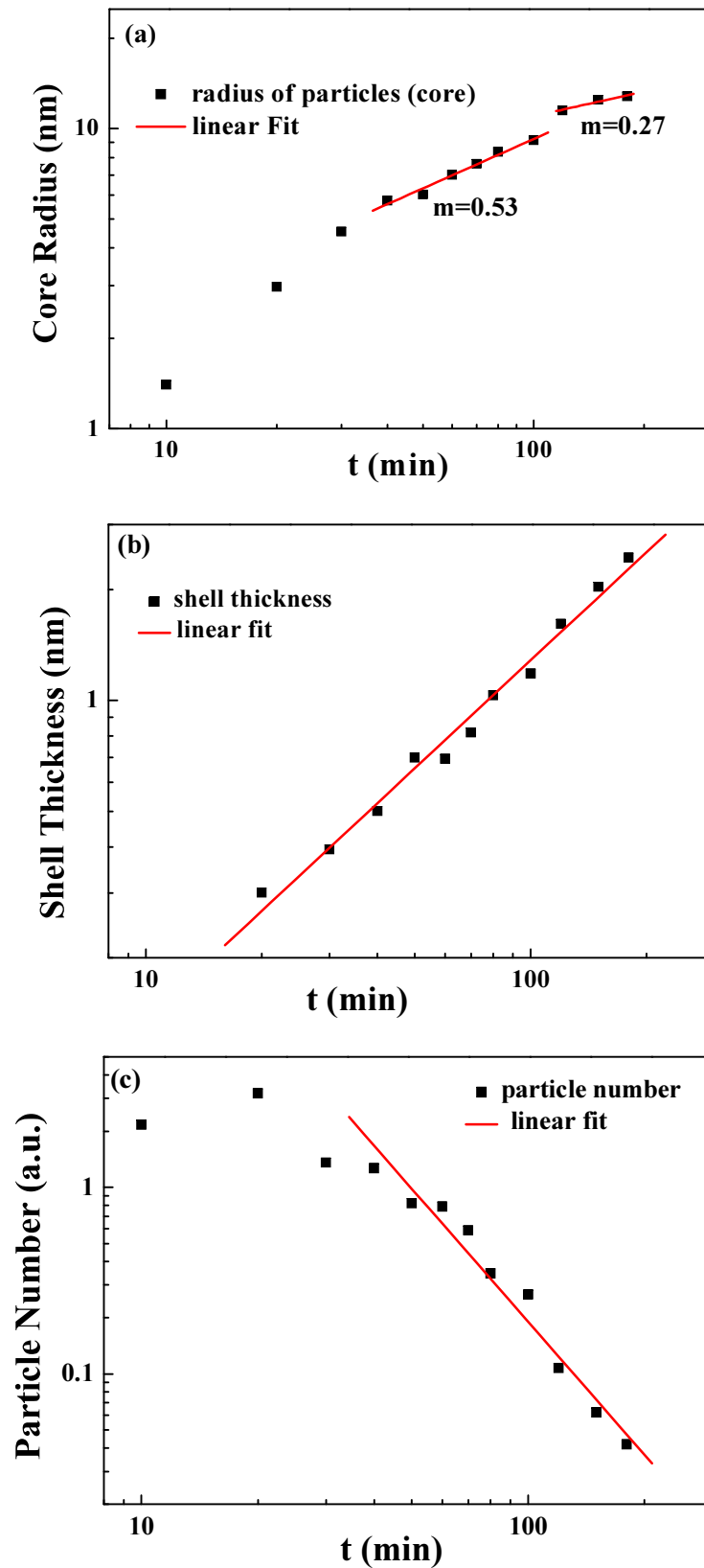


**Figure 5.32:** Fitted parameters for the insitu SAXS measurement at 640°C for variable time period from 0-180 minutes (a) Particle (b) Shell (c) Number of particles.

## 5.8 Discussion of the formation of magnetic nanoparticles

The task is to clarify the structure of the formed magnetic nanocrystals in glass ceramics. Previous studies resulted that a mixed phase containing Fe-Mn oxide is formed [9]. Microscopy results show the formation of spherical particles of sizes between 10-50nm. But to clarify the whole structure and composition we applied XRD, SAXS, SANS with polarized neutrons and ASAXS techniques.

XRD investigation reveals the formation of a  $Mn_xFe_{3-x}O_4$  phase, which is a mixed phase of Fe and Mn oxide. Particle sizes about 10-30nm are evaluated by XRD peaks analysis. But XRD investigation unsolved the exact crystals compositions and it is not clear if the crystals compositions will change with annealing time. SAXS investigation reveals that there is already a presence of very small particles in the as prepared state and with the annealing time, the size of the particle increases. Since the SAXS scattering curves for annealed sample were fitted with both spherical core shell and two sphere models, it is not possible to distinguish between both the models.

SANS investigations with polarized neutrons on the studied samples, show that the particles are magnetic and surrounded by a nonmagnetic shell like region. This result proved the formation of spherical core shell type on nanoparticles. Furthermore, the radii of the magnetic nanoparticles are smaller than the actual radii of nanoparticles as evaluated by nuclear scattering data; this reveals the presence of a small magnetic deadlayer in all the annealed samples. The existence of such kind of nonmagnetic layer was already observed in other glass ceramics [96]. Also the particles are growing with the annealing time for a particular temperature as shown in Table 5.4. Particle sizes and shell thickness evaluated for samples annealed at 550°C from SANS are comparable with the sizes calculated by SAXS investigations.

ASAXS measurements show a larger anomalous effect at the Fe edge than the Mn, which reveals the amount of Fe atoms in the particles are higher than the Mn atoms. For ASAXS data analysis a spherical core shell model was taken from SANS investigation. Quantitative information evaluated by ASAXS investigation reveals that the particles contain excessive amount of Fe atoms (up to 80%) for the sample annealed for longer time. The amount of Fe atoms in the particle computed from the resonant curves (at Fe edge) and by fitting the ASAXS curves are comparable to each other. Evaluated density  $2.22 \pm 0.05\text{g/cm}^3$  of shell reveals that the particles are surrounded by a thin layer, which is dominated by lighter elements of the glass composition. The evaluated density of shell is close to the bulk density

of  $SiO_2$  ( $2.2g/cm^3$ ) which provide a direct hint for the enrichment of shell with  $SiO_2$ . The particles also have a high volume fraction and it is increases with the annealing time. Furthermore, SAXS data analysis results in Table 5.7 shows the phase ( $Mn_xFe_{3-x}O_4$ ) formed at core, amount of  $SiO_2$  in shell and the remaining composition left as a glass matrix. The evaluated composition reveals increase in the amount of Fe atoms along with the Mn atoms and the amount of  $SiO_2$  in shell with the annealing time.

It has previously been shown that different preparation conditions of  $MnFe_2O_4$  may lead to partial oxidation of manganese or iron ions which can lead to a different distribution of Mn and Fe cations in the crystalline structure. In silicate glasses, ionic motion is the dominant diffusion phenomenon. During the crystallization of  $Mn_xFe_{3-x}O_4$  particles and subsequent crystal growth, the melt near the core is depleted in Fe and Mn, hence formed a shell enriched in Si and other glass components. This may leads to an increase in viscosity near the core and to the formation of a diffusion barrier, which can hinders further diffusion of Fe and Mn to core. With increasing annealing time, this layer becomes thicker (see Table 5.2) and the growth process is decelerated. Such type of growth has already been reported earlier during the precipitation of fluorides [100] or quartz from silicate glass [101,102]. As seen from the evaluated composition, with increasing annealing time, i.e. with the growth of the core, Fe is replaced by Mn. Presumably; pure Jacobsite ( $MnFe_2O_4$ ) will be obtained at longer annealing. This means that the particles are nucleate more like magnetite and then with annealing time Fe atoms are replaced by Mn and the growth continues with larger flux of Mn atoms. It can be associated with the smaller size of the Mn atoms, so that they go easier through the diffusion barrier of  $SiO_2$  like shell.

Furthermore, in situ investigations showing growth process that cannot be explained by classical growth theories and it will be a task for further investigations.

## 6. BaF<sub>2</sub> nanocrystals formation in transparent glass ceramics

### 6.1 Motivation

Nanoglass ceramics composed of a glassy host matrix and optically active nanocrystals play a growing role for various optical applications. In the past few decades, a revolution in optics has been emerged by the invention of a wide variety of lasers, having broad range of power, operating wavelength and beam characteristics [103,104]. These properties of lasers creates a broad range of applications, including fiber optic communications, navigation, medicine, nuclear waste fundamental studies of matter and many other fields [105,106]. Glass-ceramics containing rare-earth-doped metal fluoride or alkaline earth fluorides (BaF<sub>2</sub>, CaF<sub>2</sub>, PbF<sub>2</sub>, LaF<sub>3</sub>) nanocrystals of sizes from 5 and 100nm posses a huge potential application in fiber optics and photonics, due to their significantly enhanced fluorescence, luminescence and upconversion [107-111].

Mainly, metal fluoride nanocrystals containing glass ceramics are transparent and various factors affect the transparency and other properties of the glass ceramics such as crystallite sizes and their size distributions in the matrix and also the difference between the refractive index of the crystals and the glassy phase. An overall explanation for the formation of nano crystals is still difficult to evaluate [112]. Recently, narrower experimental size distributions were observed in glasses with specific compositions containing BaF<sub>2</sub> or CaF<sub>2</sub> [10,113]. This was explained by the formation of a diffusion barrier around the crystals during their growth [11]. During nucleation and subsequent growth of the barium fluoride crystals a fluoride and barium depleted, i.e. silica-enriched, layer is formed. This leads to an increased viscosity and a core-shell like structure is developed which acts as a diffusion barrier and limiting further crystal growth. A homogeneous dispersion of the crystals in the glassy matrix and a narrow crystal size distribution is the consequence [10]. Previously, an experimental evidence of such a silica enriched shell surrounding BaF<sub>2</sub> nanocrystals in glass ceramics was shown by using energy filtering transmission electron microscopy (EFTEM) and electron energy-loss spectrometry (EELS) spot analysis [12]. This qualitative information needs to be quantified; therefore the aim of work is to gain mechanistic insight. We apply ASAXS technique for quantitative analysis of the shell (sizes and composition) and of the distribution of the nanocrystals.

## 6.2 Glass preparation

Glass ceramic samples were prepared by using reagent grade raw materials  $Na_2CO_3$ ,  $K_2CO_3$ ,  $BaF_2$ ,  $Al(OH)_3$  and  $SiO_2$  (quartz). The glass preparation was done by our cooperation partners at the university Jena. Glass batches of 200g were prepared in a platinum crucible which was covered in order to avoid strong fluoride evaporation. The crucible was placed in a furnace and heated to  $1590^\circ C$  kept for 1.5h. Then the melt was cast on a copper block and subsequently placed into a furnace at  $450^\circ C$ . The glass transition temperature  $T_g$  for these glasses is  $549^\circ C$ . In order to relax thermal stresses, the cooling furnace was switched off and the glasses were cooled down to room temperature. For a better homogeneity, the glasses were re-melted in an inductive furnace at  $1500^\circ C$  and stirred for 20min. In a second step, the glasses were crystallized in a one step annealing process at temperatures in the range from  $500$  to  $700^\circ C$  for 2 to 20h. The already crystallized glass samples are visually transparent as shown in Figure 6.1.



**Figure 6.1:** Transparent  $BaF_2$  nanocrystal containing glass ceramics [10].

The remaining fluorine concentration in later glasses was determined by a wet-chemical analysis method [114]. X-ray fluorescence and energy-dispersive X-ray spectrometry in a scanning electron microscope results, a mean value of  $66 \pm 3\%$  of the fluorine remains in the glass which leads to a nominal mol% composition of sample  $69.6SiO_2-15.0K_2O-7.5Al_2O_3-1.9Na_2O-4BaF_2-2BaO$ . The composition for the samples as prepared and after analysis is shown in Table 6.1. The density of the bulk glass samples are  $2.603 \pm 0.001g/cm^3$ , which was measured by a helium pycnometer (AccuPyc 1330). Structural behavior and composition of nanoparticles in the glass samples were studied by SAXS and ASAXS. The thicknesses of the samples are about  $30-50\mu m$ , which is suitable to achieve optimal X-ray transmission for the SAXS and ASAXS measurements.

**Table 6.1** Composition of the glass ceramics as synthesis and as analyzed.

Element	Weight (%) Synthesis	Mol (%) Synthesis	Weight (%) Analyzed	Mol (%) Analyzed
Al	5.4	4.8	5.4	4.8
K	15.6	9.5	15.6	9.5
Na	1.2	1.2	1.2	1.2
Si	26.0	22.1	26.0	22.0
Ba	10.9	1.9	10.9	1.9
F	3.0	3.8	2.0	2.5
O	37.9	56.7	39.0	58.1

### 6.3 Sample Characterization

To investigate the crystalline phase and structure of the nanoparticles in the glass matrix, various characterizing techniques were already applied on the studied samples such as TEM and XRD. It is already reported that definite annealing of these glasses leads to a formation of BaF<sub>2</sub> nano crystals which are dispersed very homogeneously in the glassy matrix with a narrow crystallite size distribution [10]. These samples are pre-characterized by transmission electron microscopy (TEM). Figure 6.2 shows the dark field TEM image of the glass ceramics sample annealed at 540°C for 20h [10]. The contrast between the bright crystals and the light gray background for the amorphous matrix is clearly visible in the image. The TEM image shows the formation of almost spherical shaped particles. Further investigation of the image reveals the presence of 252 crystallites with a mean crystallite size of  $9 \pm 2$ nm. The dark field TEM image of a sample annealed at 600°C for 20h is shown in Figure 6.3. It is clearly seen from the image that there is a formation of bigger crystals for the sample annealed at 600°C than the sample annealed at 540°C. The size distribution analysis of that sample shows the crystallites with the mean size of  $15 \pm 2$ nm.

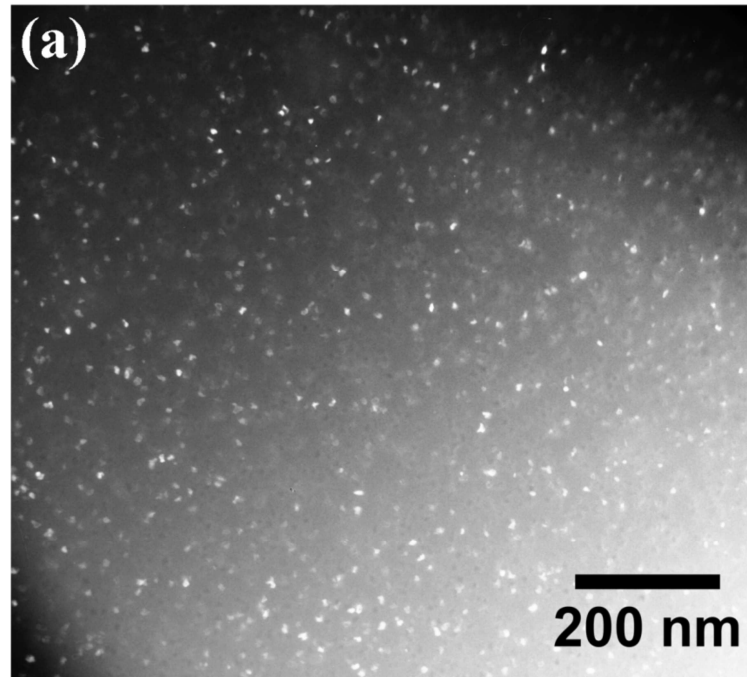


**Figure 6.2:** Dark field TEM image of the sample annealed at 540°C for 20h [10].

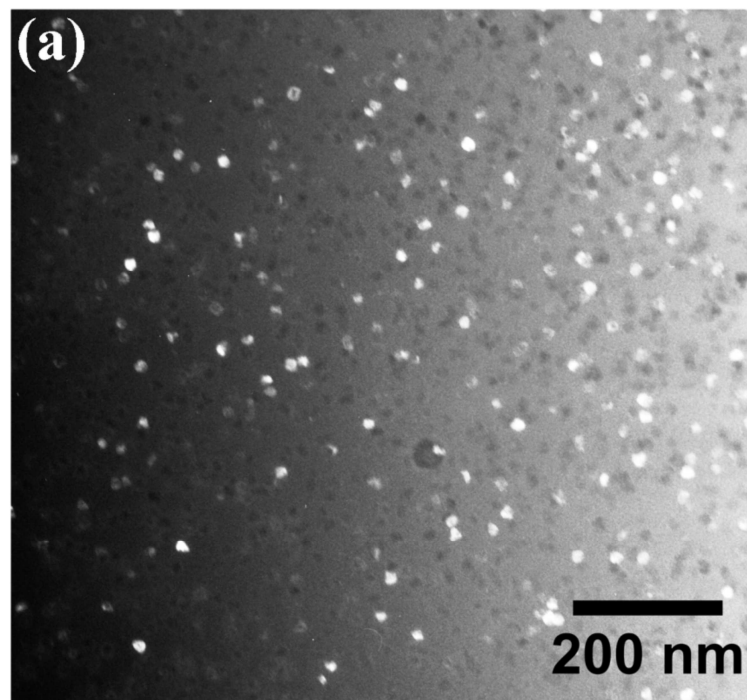


**Figure 6.3:** Dark field TEM image of the sample annealed at 600°C for 20h [10].

For the sample annealed at 700°C, a TEM micrograph was obtained as shown in Figure 6.4. It shows dark appearing BaF<sub>2</sub> crystals in a grey glassy matrix. Due to the low contrast, a reliable size distribution was not computed. However, it can be seen from the image that most crystals are in the range from 50 to 70nm in diameter with a few crystals larger than 100nm. Microscopic measurements and investigations show the growth of the crystallites with the

annealing temperature. Such type of microscopic investigations provides information only about the size, shape and distribution of particles in the host matrix, but they do not provide any information about the phase (crystalline or amorphous) of the particles. However, in order to determine the phases of the particles, one option is to use the TEM measurements in the diffraction mode and other option is to perform X-ray diffraction measurements.

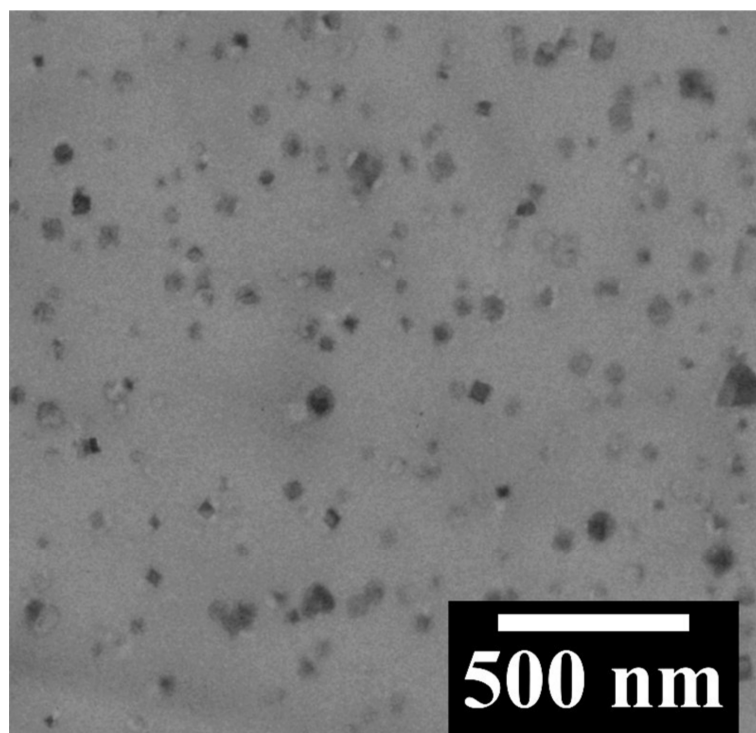


**Figure 6.4** TEM image of BaF<sub>2</sub> particles for the sample heat treated at 700°C for 2h.

To determine the phase of the crystalline particles, XRD experiments are performed on the samples. For recording the X-ray diffraction patterns, diffractometer Siemens D 5000 using a Cu<sub>K $\alpha$</sub>  (wavelength  $\lambda = 0.154\text{nm}$ ) radiation source and an energy-dispersive SolX detector was used. Figure 6.5 shows the XRD measurement of the as prepared and heat treated samples [10]. Figure shows that, for as prepared sample there are no visible peaks or distinct maxima is observed except the broadness around 27° due to the silica. For the samples heat treated at different temperatures clearly shows the visible peaks around 25°, 28°, 42° and 48° which attributed to the crystalline BaF<sub>2</sub> (JCPDS Nr. 4-452) phase. The sample heat treated at 540°C for 20h shows the broadened peaks and lower intensity as compare to the sample heat treated for 600°C and 700°C. The full width at half maxima (FWHM) of the peaks decreases with increasing annealing temperature, which reveals the growth of particles. From the peak broadening, the mean crystallite size was evaluated by using Debye Scherrer equations (6.1) by using the values for shape factor  $K = 0.89$  for cubic crystals, and the X-ray

wavelength of 0.154nm (Cu K<sub>α</sub> radiation). The mean crystallite sizes of samples as calculated by Scherrer equation were  $10.8 \pm 1$ nm and  $12.5 \pm 1$ nm for the samples annealed at 540°C and 600°C for 20h, respectively. The sample annealed at 700°C for 2h showed a mean crystal size of  $37.6 \pm 4$ nm. By XRD technique it is possible to determine the information about the crystalline phase and mean crystallite sizes, but by XRD it is not possible to get any information about possible amorphous phases in the studied glass ceramics. Since XRD and microscopy measurements are not sufficient to provide the complete information about the structure and composition, SAXS and anomalous SAXS (ASAXS) experiments will be performed in the frame of this work.

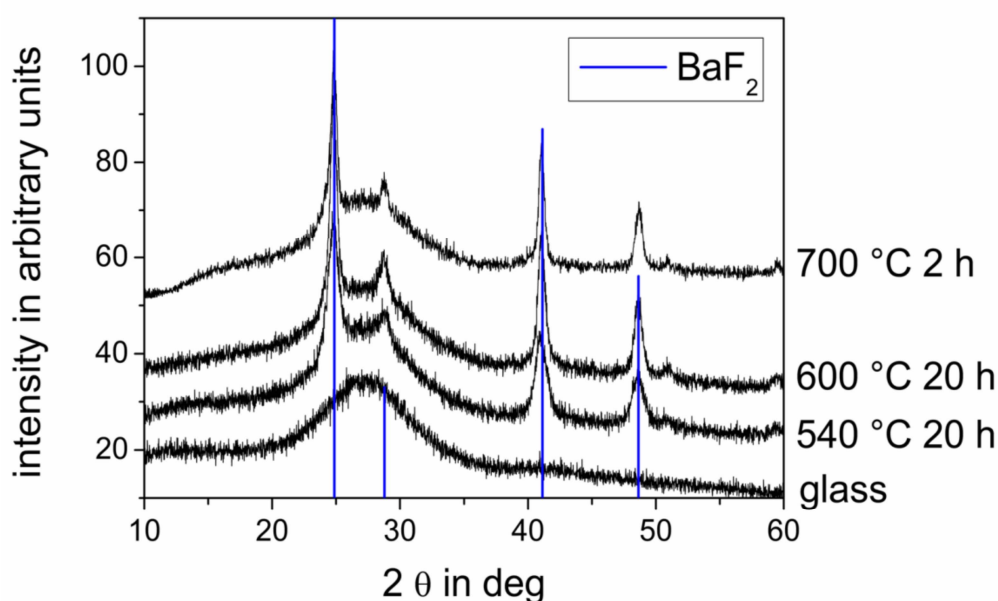


**Figure 6.5:** XRD-patterns of sample annealed at various temperatures and times. The peaks marked by blue line are all attributed to cubic BaF<sub>2</sub> crystals (JCPDS Nr. 4-452) [10].

Earlier, by applying energy filtering transmission electron microscopy (EFTEM) and electron energy-loss spectrometry (EELS) spot analysis techniques on these samples provide evidence for the formation of core shell like nanostructures, where the shell region is enriched with silica and the core region is of BaF<sub>2</sub> nanocrystals [12]. In order to summarize these pre-investigations, it has to be pointed out that a formation of BaF<sub>2</sub> takes place and a SiO<sub>2</sub> enriched shell region could be revealed. This shell region seems to hinder the diffusion and increases the viscosity. The aim of my SAXS and ASAXS investigations is a direct structural evidence of these findings of a core shell structure and a quantitative analysis of nanostructure and compositions.

## 6.4 SAXS Results

In order to investigate the effect of heat treatment on the shape, size, volume fraction and distribution of particles in the glass matrix, the samples were studied by SAXS and the composition of the particles will be determined by analysing the ASAXS curves. For the SAXS measurements at BESSY II, X-ray energy of 4900eV which is sufficiently below the Ba L<sub>3</sub> X-ray absorption edge (5247eV) was used. The samples were measured under vacuum conditions (10<sup>-3</sup>mbar) conditions to reduce air scattering. The samples were measured at both long and short distance of the detector, in order to achieve wide  $q$  range. Figure 6.6 show SAXS curves calibrated to differential scattering cross sections for as prepared and annealed samples at various temperatures and time scales. As seen from the Figure the as prepared sample show a small hump at  $q=0.8\text{nm}^{-1}$ , which refers to the presence of small particles. In Figure 6.6 slope of the scattering curve for as prepared sample approached a  $q^{-4}$  behavior at lower  $q$  values, which implies for the smooth surface of the particles.

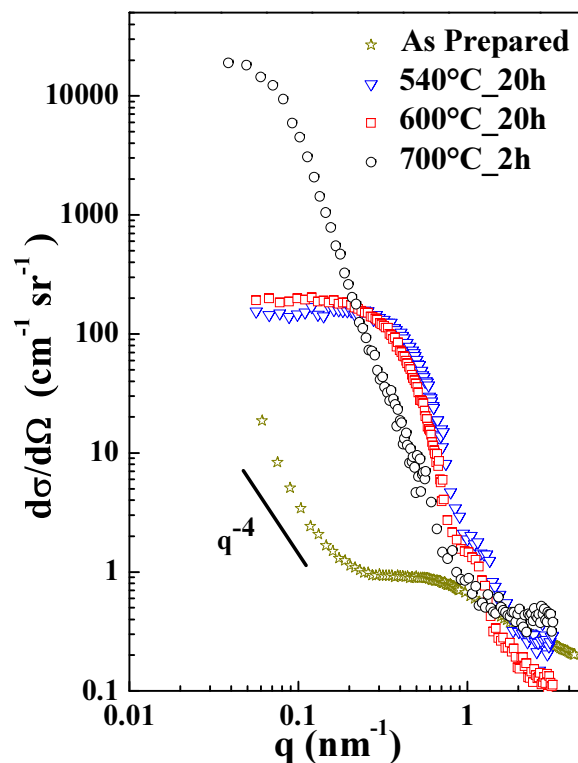


**Figure 6.6:** SAXS curves measured at 4900eV for the as prepared and annealed samples at 7TMPW SAXS beamline BESSY II.

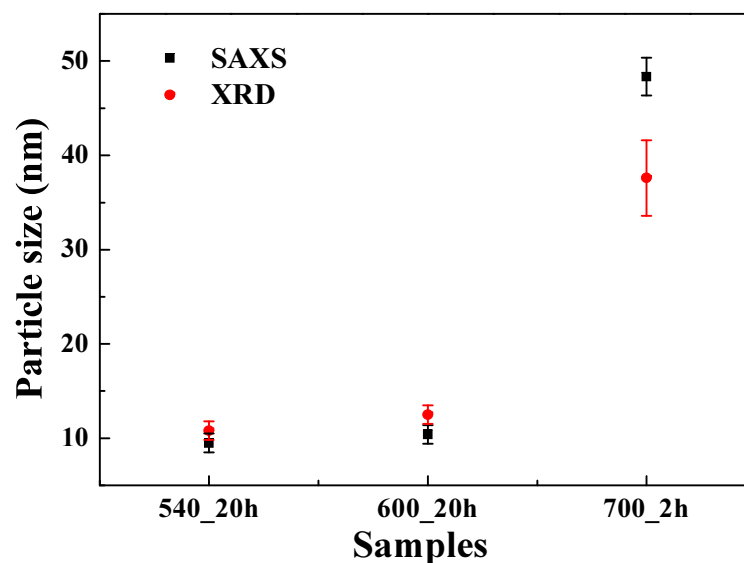
The shoulder in the SAXS curves for the heat treated sample at 540°C and 600°C were shifted towards the lower  $q$  values which indicates an increase in the size of particles with the annealing temperature. The sample annealed for 700°C for 2h shows a higher intensity which

is due to the larger size of the particles as compared to the other three samples. In order to extract the structural information from the scattering curves. The curves were further processed by fitting them using the SASfit program [62]. On the basis of pre-investigations in section 6.3 a core shell structure has to be assumed. For fitting, spherical core-shell model and on the basis of TEM analysis a Gaussian distribution for the particles has to be taken into account [10]. Table 6.2 shows the parameters obtained after fitting of the SAXS curves for the annealed samples. Structural parameters reveal that the size of the particles increases with the annealing temperature. Furthermore, the thickness of the layer decreases notably with increasing temperature.

**Table 6.2:** Parameters for the SAXS measurement assuming a Gauss distribution of particles for the samples annealed at 540°C and 600°C for 20h and 700°C for 2h.

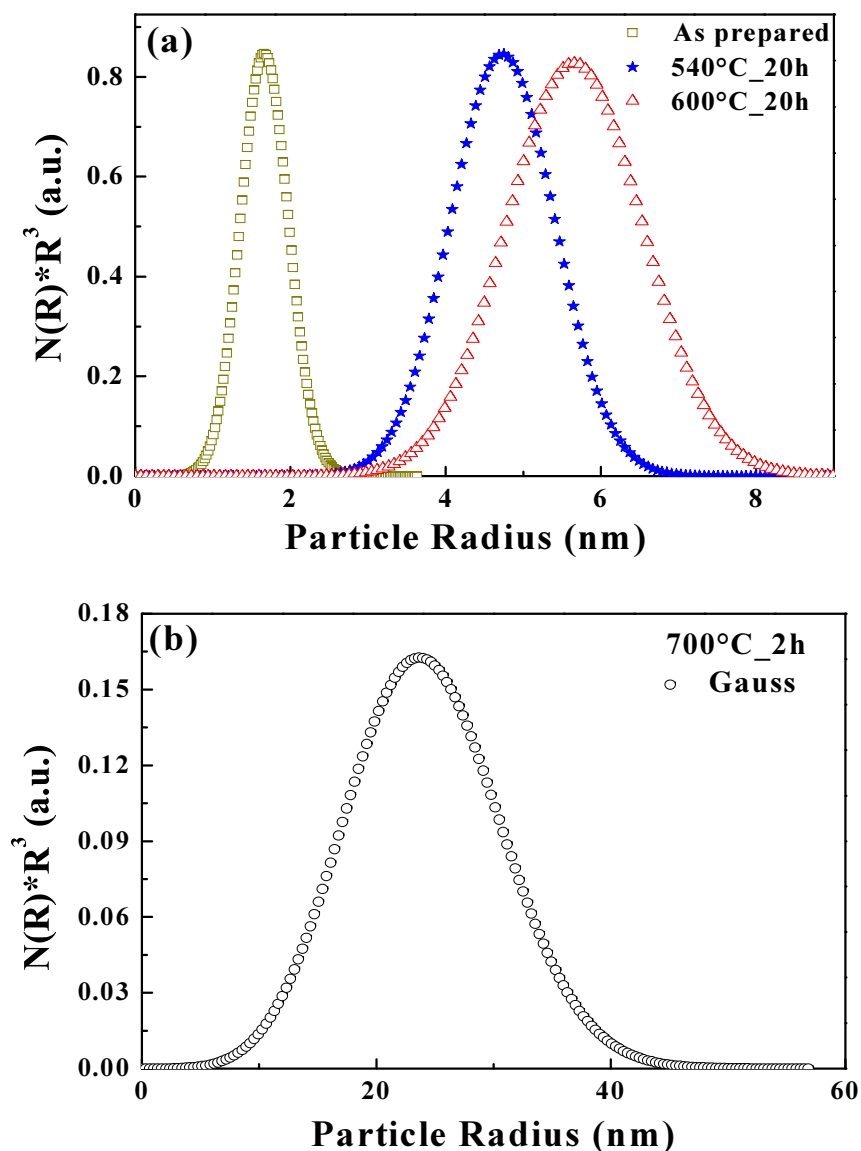
Parameters	540°C 20h	600°C 20h	700°C 2h
Radius Particle (nm)	4.75 ± 0.5	5.20 ± 0.5	24.2 ± 1.0
Shell Thickness (nm)	2.35 ± 0.1	2.13 ± 0.1	1.82 ± 0.1

Figure 6.7 shows the comparison of the size parameters evaluated by XRD and SAXS. The mean crystallite sizes calculated by XRD are in good agreement with the mean sizes calculated after fitting of SAXS curves for the samples annealed at 540 and 600°C, while the sample annealed at 700°C shows the larger size as compare to XRD. As prepared glass samples contains already particles of very small size of 3nm with a narrow size distribution. This is a new result that could not be determined by XRD measurements.



**Figure 6.7:** Comparison of the average diameter from SAXS and the XRD size parameter given by Scherrer equation.

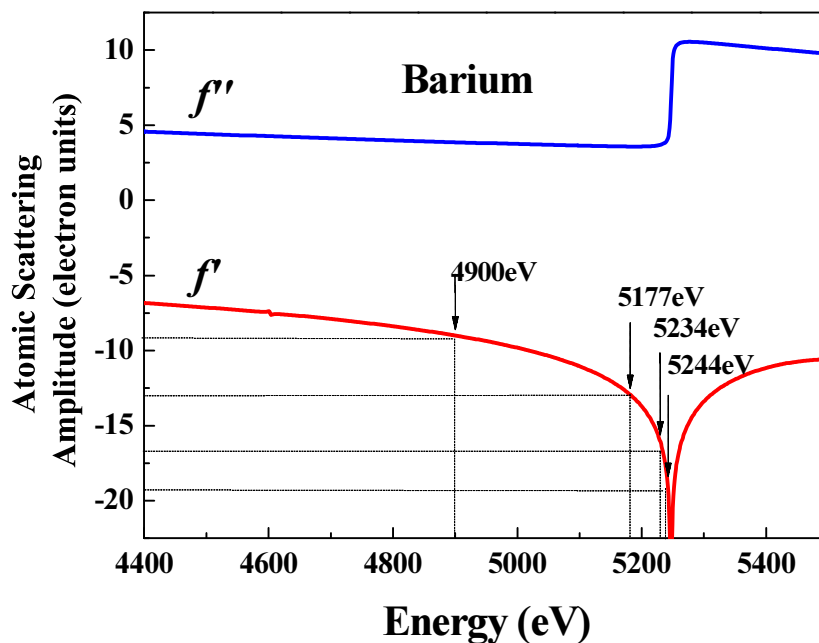
The core structure for the samples annealed at 540°C and 600°C have nearly the same shaped size distributions as shown in Figure 6.8 (a) with maxima at 4.7 and 5.5nm, respectively. The sample treated at 700°C for 2h shows a remarkable larger size as shown in Figure 6.8 (b). From the SAXS measurements alone it is not possible to evaluate the composition of the shell surrounding the nanoparticles. ASAXS experiment in the next section provides the possibility to validate the composition of the nanocrystals and to investigate the composition of the shell surrounding the particles.



**Figure 6.8:** Size distributions of the particles obtained after fitting of the SAXS curves. (a) Gauss distribution for the as prepared and two heat treated sample at 540 and 600°C for 20h. (b) Gauss distribution of the sample heat treated at 700°C for 2h.

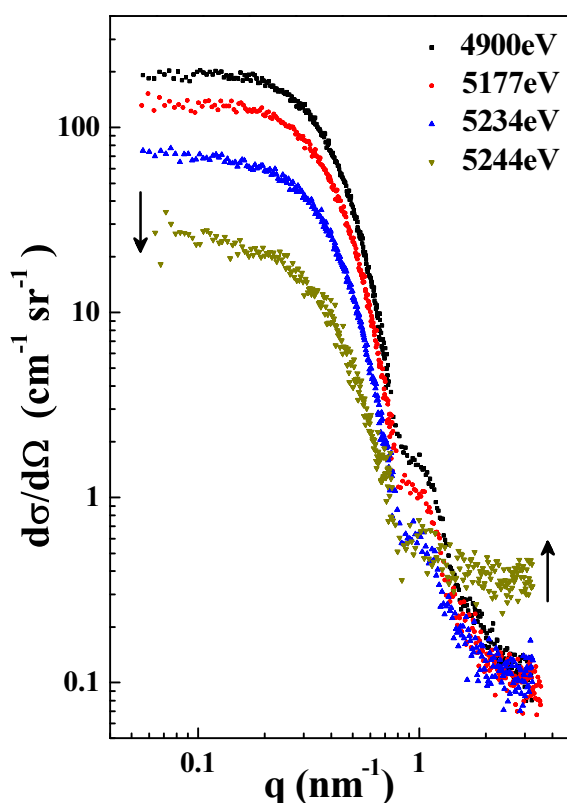
## 6.5 ASAXS studies

Figure 6.9 shows the variation of the atomic scattering amplitude for the Ba L<sub>3</sub> X-ray absorption edge (5247eV). For ASAXS measurement four different energies were chosen near L<sub>3</sub> X-ray absorption edge of Barium. The arrows in Figure 6.9 shows the energies used for the ASAXS measurement. The scattering curves were corrected and finally obtained the differential scattering cross sections as a function of the magnitude of the scattering vector  $q$ .



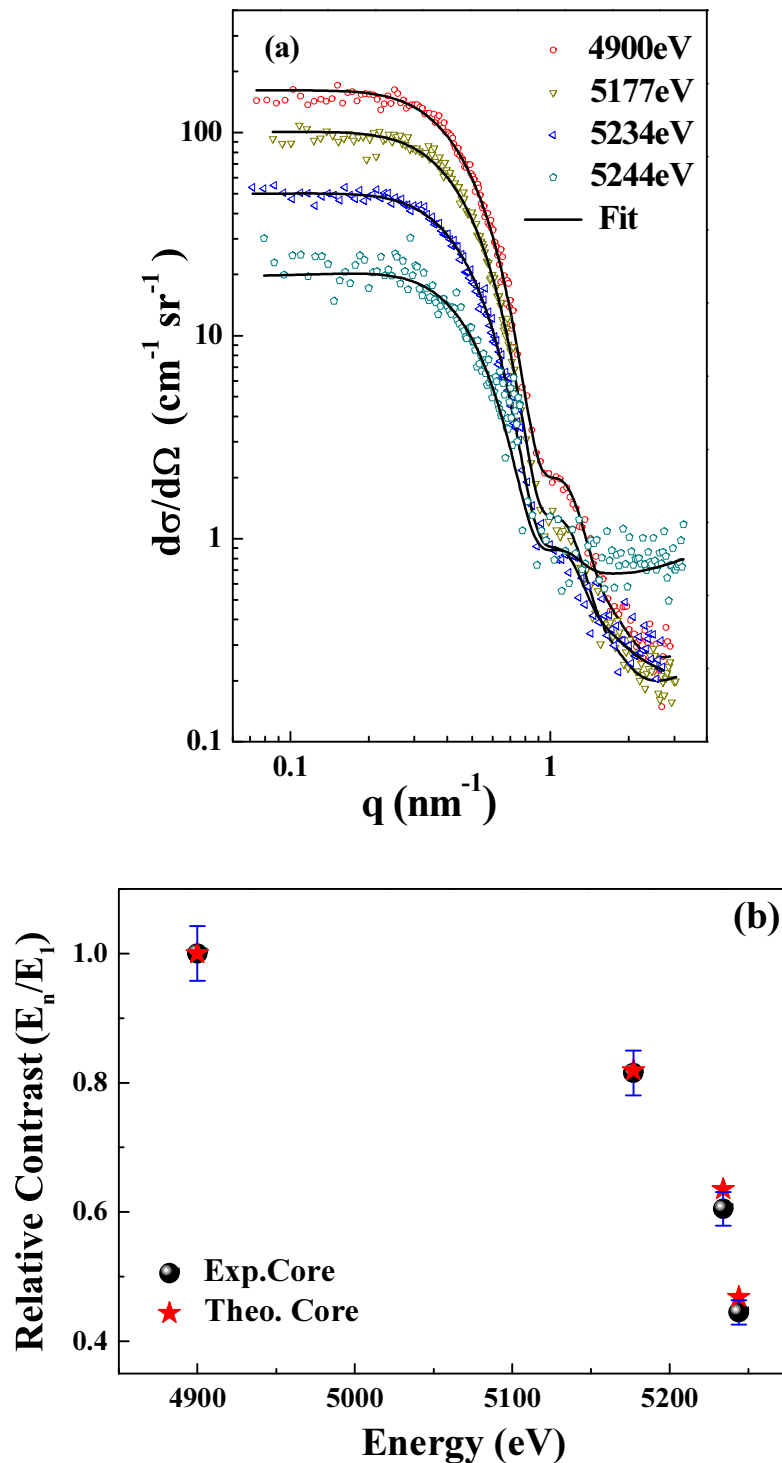
**Figure 6.9:** Atomic scattering amplitude of Ba atoms at the Ba L<sub>3</sub> absorption edge (5247eV) and the X-ray energies used for the measurement.

Figure 6.10 shows the ASAXS curves measured at four energies for the sample annealed at 600°C for 20h. A large variation (decrease) of the scattered intensity at the lower  $q$  values while as moving towards the energy close to X-ray absorption edge, while for the higher  $q$  region at the energy close to absorption edge varies in the upward direction, which is due to the upcoming resonant Raman scattering. Also all the other samples show significant ASAXS effects near the Ba absorption edge including the as prepared sample.



**Figure 6.10:** ASAXS curves measured at four different energies near the absorption edge of Ba for the sample annealed at 600°C for 20h

In order to extract information from the ASAXS curves, each set of curves were fitted by SASfit program. While fitting all the structural determining parameters such as particle number, and the size distributions are kept constant and only the contrast between the particles with respect to the matrix varies as a free variable. The three samples annealed at different temperature and times were fitted by assuming the spherical core shell model with the Gauss distribution of particles. Figure 6.11 (a) shows fitted curves of the sample heat treated at 540°C for 20h that model the measurement in a very good quality. Form the fitting procedure; one can obtain four different values of experimental contrasts for the core of particles. To calculate the composition and density of the phases (shell and matrix), the experimental contrasts values were further fitted with the theoretically calculated contrast as discussed in section 3.4. During the distribution of atoms in core, shell and matrix, the total number of atoms for each element was conserved. During fitting we had assumed the bulk density of BaF<sub>2</sub> (4.89g/cm<sup>3</sup>), since there is no shifting of the peaks positions in XRD investigations.



**Figure 6.11:** (a) ASAXS fitted curves measured at four energies near the absorption edge of the Ba (5247 eV) for the samples 550°C 20 h. (b) Comparison of the experimental and theoretical relative contrast variation.

Figure 6.11(b) show the comparison of the theoretically calculated and experimentally evaluated relative contrast of the sample annealed at 540°C for 20h. Table 6.3 shows the parameters obtain after fitting routines for all the three samples. The respective parameters lead to a density of layer and matrix of around  $2.2 \pm 0.1\text{g/cm}^3$  and  $2.55 \pm 0.03\text{g/cm}^3$ ,

respectively. Parameters show that the particle volume fraction increases from 0.025 to 0.044 with the annealing temperature.

**Table 6.3:** Resulting parameters for a SAXS as well as ASAXS curves assuming the Gauss distribution of particles for the samples annealed at 540 and 600°C for 20h and 700°C for 2h.

Parameters	540°C 20h	600°C 20h	700°C 2h
Radius Particle (nm)	4.75 ± 0.5	5.20 ± 0.5	24.18 ± 1.0
Shell Thickness (nm)	2.35 ± 0.1	2.13 ± 0.1	1.82 ± 0.1
Density Core (g/cm <sup>3</sup> )	4.89	4.89	4.89
Density Shell (g/cm <sup>3</sup> )	2.20 ± 0.1	2.35 ± 0.1	2.2 ± 0.1
Density Matrix (g/cm <sup>3</sup> )	2.55 ± 0.03	2.58 ± 0.03	2.50 ± 0.03
Volume fraction particle	0.025	0.032	0.044
Volume Fraction Shell	0.049	0.045	0.01
Volume Fraction Matrix	0.926	0.923	0.946

Table 6.3 shows the composition evaluated after fitting experimental contrast with the theoretical contrast for all the annealed samples. Composition shows that the layer surround the core (BaF<sub>2</sub>) is enriched with low density SiO<sub>2</sub> and with other glass components in fewer amounts. After the formation of core and shell, remaining glass components forms the matrix composition.

**Table 6.4:** Composition calculated from ASAXS for the samples annealed at 540°C, 600°C for 20 h and 700°C for 2h.

Sample	Particle	Shell <sup>a</sup>	Remaining matrix Composition
540°C_20h	BaF <sub>2</sub>	SiO <sub>2</sub> (91%)	69.71SiO <sub>2</sub> -16.15K <sub>2</sub> O-7.99Al <sub>2</sub> O <sub>3</sub> -2.03Na <sub>2</sub> O-2.03BaF <sub>2</sub> -2.1BaO
600°C_20h	BaF <sub>2</sub>	SiO <sub>2</sub> (89%)	70.37SiO <sub>2</sub> -16.10K <sub>2</sub> O-7.93Al <sub>2</sub> O <sub>3</sub> -2.02Na <sub>2</sub> O-1.47BaF <sub>2</sub> -2.11BaO
700°C_2h	BaF <sub>2</sub>	SiO <sub>2</sub> (76%)	72.02SiO <sub>2</sub> -15.69K <sub>2</sub> O-7.84Al <sub>2</sub> O <sub>3</sub> -1.97Na <sub>2</sub> O- 0.40BaF <sub>2</sub> -2.08BaO

<sup>a</sup> SiO<sub>2</sub>+(Ba,Na,Al,O,K)

From the ASAXS curves one can also evaluate the distribution of particular element in the system by Stuhmann equation (3.20). By using this method pure resonant scattering contribution due to the distribution of Ba atoms in the samples annealed at different time and temperature has been separated from the total scattering SAXS curves.

Figure 6.12 shows the resonant curves fitted with the sphere model for the samples annealed at 540 to 700°C evaluated by using equation (3.20). From the resonant curves, the number density of the resonant atoms was calculated by equation (3.21). The number of Ba atoms in the crystalline phase was found for the sample annealed at 600°C is about 48% of the total Ba atoms in the system. The comparison of the atomic fraction of Ba atoms in nanoparticles calculated by ASAXS and the resonant curves are shown in Figure 6.13.

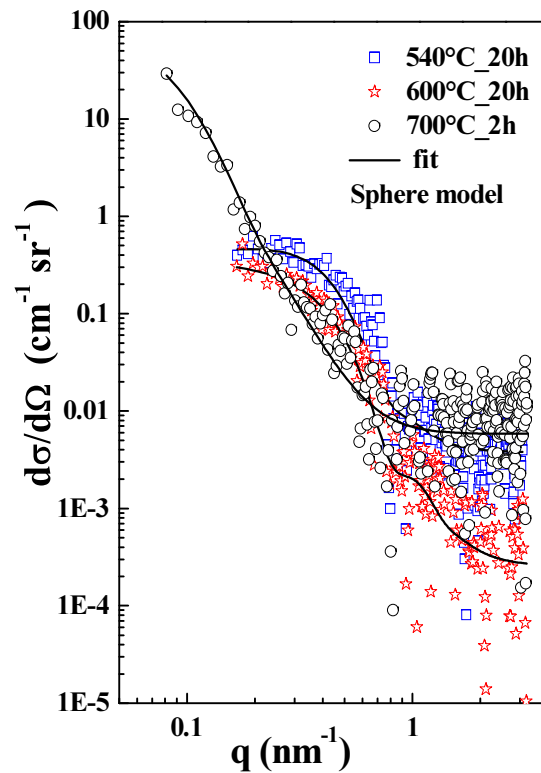


**Figure 6.12:** Resonant scattering curves for Barium calculated by the Stuhrmann method and fitted with sphere model.

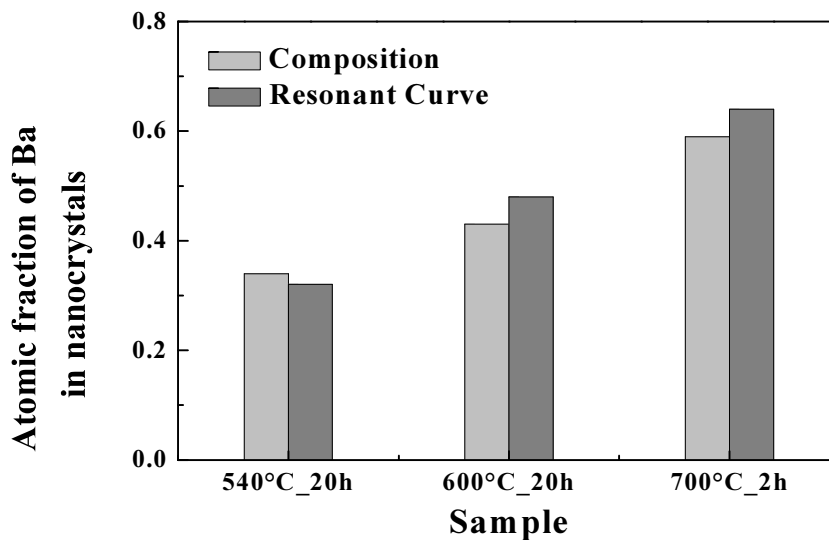


**Figure 6.13** Comparison of the atomic fraction of Ba atoms in nanoparticles calculated by resonant curve and from the composition calculated from the ASAXS curves.

The scattering intensity of as prepared sample is rather small due to very small particle size of 3nm as shown in Figure 6.6. Since both the sphere and spherical core shell model fits to the scattering curves, it is not sure whether a shell region is formed around the particles during glass preparations. ASAXS investigations on the sample shows noticeable contrast variation near the Ba absorption edge, which give an evidence for the presence of particles enriched with Barium. Figure 6.14 (a) and (b) show fitted ASAXS curves for both the spherical and spherical core shell models for the as prepared sample. Furthermore, it is not clear whether these particles are crystalline or amorphous, because these particles are not observed by XRD and TEM investigations. The particles region might be formed due to bonding between Ba and F atoms, but yet they are not crystalline as reported by NMR investigations [115].

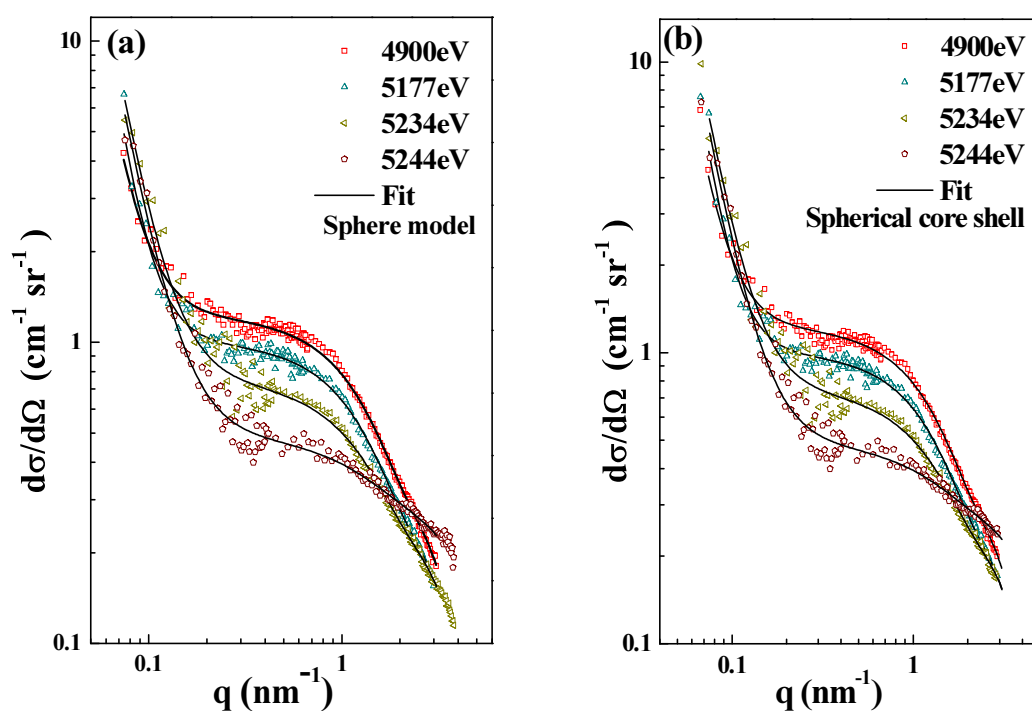


**Figure 6.14:** ASAXS fitted curves measured at four energies near the  $L_3$  absorption edge of the Ba (5247eV) for the as prepared. (a) Fit the sphere model (b) Spherical Core shell model.

## 6.6 Discussion of the structure model of BaF<sub>2</sub>

It was reported in refs. [10,116,117] that in a silicate glass of composition 69.6SiO<sub>2</sub>-7.5Al<sub>2</sub>O<sub>3</sub>-15.0K<sub>2</sub>O-1.9Na<sub>2</sub>O-4BaF<sub>2</sub>-2BaO containing BaF<sub>2</sub> nanoparticles are growing and, a SiO<sub>2</sub> enriched layer around the nanoparticles might be formed. This layer hinders further diffusion of Ba ions towards the particles and hence acts as a diffusion barrier, which inhibits further growth of crystals. Also an increase of the glass viscosity is reported.

ASAXS measurements at the Ba L<sub>3</sub> absorption edge provide information on the distribution of Ba atoms in the studied glass ceramics. The observed contrast variation is caused only due to the resonant Ba atoms. ASAXS measurements on the as prepared glass sample show already a prominent contrast variation close to the Ba edge, which provides a direct evidence for the formation of very small (3nm) Ba enriched particles or regions during melting and quenching the glasses. However, it cannot be said whether these particles are crystalline or amorphous. According to the NMR results it is more likely that these “particles” are due to regions where Ba is bonded with F but they are not yet crystalline [115]. As both spherical and spherical core shell models fits to ASAXS curves, yet it is not confirmed whether these particles were of spherical shape or the particles were already surrounded by a layer enriched in other components. These particles also have a very low volume fraction (<0.5 %).

The samples annealed at various temperatures and times, also show prominent ASAXS effect close to the Ba absorption edge and their scattering intensity is dramatically increased in comparison to the as prepared samples. Table 6.2 shows the parameters obtained after fitting the ASAXS curves with spherical core shell model for all heat treated samples. The parameters show that there is not much difference in the particle sizes (8-12nm) of samples annealed at 540 and 600°C. The particles in these samples are surrounded by a rather thick layer (2.35 - 2.13nm). Later on, for the sample annealed at 700°C, the crystals are larger (44nm) and surrounded by a rather thin layer (1.8nm). The density of the shell calculated by fitting the experimental contrasts is close to the density of amorphous SiO<sub>2</sub> (between 2.0 to 2.2g/cm<sup>3</sup>) which provides a further hint of the presence of SiO<sub>2</sub> enriched layer.

Table 6.3 shows the composition of the particles, the layer and the matrix evaluated after fitting the experimental contrasts. The calculation reveals the formation of BaF<sub>2</sub> particles and the layer surrounds the particles is predominantly composed of SiO<sub>2</sub>. The formation of particles surrounded by the layer (shell) revealed from the ASAXS curves analysis could be explained as; during annealing, nuclei are formed and start to grow, but due to large

differences in the diffusion coefficients of Ba and F ions (approximately two orders of magnitudes), the Ba ions diffuse slower than F ions [118,119]. Meanwhile, because of the formation of the crystals, the other components of the glass are enriched near the crystals. However, near the interface of crystal and matrix there will be a depletion layer of the crystal forming components Ba and F which leads to a rise in viscosity. This layer acts as a barrier for further diffusion of Ba and F ions towards the crystals. Due to this barrier, in the temperature range of 540 to 600°C, the particles grow slowly and do not exceed a certain sizes. But at higher temperatures (700°C) and increased diffusion rates this layer starts to dissolve in the matrix and becomes less important for the hindrance of the diffusion of ions. This results in a decrease of the shell thickness and in an increase in the size of particles. An increase in the volume fraction of the crystals with temperature resembles the growth of the particles. A Figure 6.13 show a bar chart of the percentage of Ba atoms presents in the core region as a crystalline BaF<sub>2</sub> phase and illustrates an increase of this percentage with the annealing temperature.

ASAXS technique does not only provide qualitative information, but also it gives quantitative information on the distribution of particular resonant atoms in the system. The extraction of the resonant curve of particular atoms from the SAXS curves shows that the Ba atoms are dominant in the particles. The atomic fraction of Ba atoms in the nanoparticles, calculated by using equation (3.21), shows that 30-60% of the Ba atoms are incorporated into the crystals, which is in agreement with the composition as calculated by ASAXS.



## 7. Summary and Outlook

In this work, the structure and averaged chemical composition of two different glass ceramic materials containing spherical core shell type nanocrystals were analyzed quantitatively by using small angle scattering methods: small angle neutron scattering (SANS) and especially the method of anomalous small angle X-ray scattering (ASAXS). The nanocrystals are formed during controlled heat treatments in two different types of silicate based glass ceramics. The common aspect of both ceramics is that the formation of a three phase system is occurring (a nanocrystalline core, a silica shell and the glass matrix).

First, I investigated the structure of magnetic nanocrystals ranging from magnetite to Jacobsite phases (generally composed of  $Mn_xFe_{3-x}O_4$ ) in a silicate glass ceramics. XRD investigations could only show the formation of  $Mn_xFe_{3-x}O_4$  phases which appeared as a mixed phase of Fe and Mn oxides. XRD gave no information about the Fe to Mn ratio. Composition and structural information evaluated by ASAXS analysis reveals that during crystallization a layer around the nanoparticles is formed. This layer is depleted in Fe and Mn and becomes enriched with other glass components, mainly with Si and O. Moreover, the amount of  $SiO_2$  increases in the layer with the annealing time. Depending on the viscosity of the layer, a  $SiO_2$  enriched layer may act as a diffusion barrier for further diffusion of Fe and Mn ions towards the nanoparticle core. Therefore, the further crystal growth is kinetically slowed down. Furthermore, ASAXS results show that the particles start to nucleate like magnetite ( $Fe_3O_4$ ). With an ongoing annealing time, Fe atoms are replaced by Mn in the crystal and the phase changes towards the pure Jacobsite ( $MnFe_2O_4$ ) phase due to the higher diffusion of Mn into the nanoparticles. SANS investigations with polarized neutrons clearly show that the particles are magnetic. However, they are surrounded with a thin magnetic dead layer followed by a nonmagnetic  $SiO_2$  enriched shell region.

Second, I studied  $BaF_2$  nanocrystals precipitated in an optically transparent silicate glass ceramics. Already during the preparation of glasses small Ba enriched particles of about 3nm in diameter are formed. These particles give a pronounced ASAXS effect for the as prepared samples. During further annealing,  $BaF_2$  nanocrystals grow in the glass matrix and a silicate enriched layer is formed. Previous investigations on these glasses by energy filtered TEM showed the formation of a  $SiO_2$  layer, which hinders the further growth of the  $BaF_2$  particles. Quantitative information about the structure and composition of the  $BaF_2$  nanoparticles evaluated by ASAXS provides direct structural evidence for the formation of a  $SiO_2$  enriched layer. This layer is formed during the crystallization of the particles and has a lower density

( $2.2\text{g/cm}^3$ ) than the host glass matrix ( $2.603\text{g/cm}^3$ ). Furthermore, for annealing temperatures at  $540^\circ\text{C}$  and  $600^\circ\text{C}$ , a thick layer enriched with  $\text{SiO}_2$  is formed, which hinders the further diffusion of Ba and F ions towards the particles. A further growth of these nanocrystals (diameter about  $12\text{nm}$ ) is effectively inhibited. At a higher temperature of  $700^\circ\text{C}$ , the diffusion rates increase and the layer begins to dissolve into the matrix. The layer becomes less important for the hindrance of the diffusing ions (Ba and F). As a result, the shell thickness decreases and the size of the  $\text{BaF}_2$  particles increase significantly (to about  $50\text{nm}$ , see Figure 6.7).

### *Outlook:* kinetic studies

For both investigated systems, time and temperature dependent results on the growth of the nanocrystals are derived in this thesis. It is known that a growth inhibition takes places in the  $\text{BaF}_2$  crystallizing glass ceramics. In chapter 5.7, a similar process was found in case of the magnetic glass ceramic. In situ SAXS and ASAXS investigations should be carried out in order to study the crystallization kinetics in more detail and the role of structural development of the diffusion barrier layers surrounding the nanocrystals. As known from in situ studies on the immiscibility in oxide glasses the role of the atmosphere should also be studied.

### *Outlook:* rare-earth-doped metal fluoride nanocrystals

It is known that rare-earth-doped metal fluoride nanocrystals feature enhanced fluorescence, luminescence and up-conversion. Therefore, the formation of  $\text{CaF}_2$  nanocrystals should be studied with respect to a formation of a  $\text{SiO}_2$  enriched diffusion barrier layer. This should be compared to the results in this thesis. Moreover, the segregation process of the rare-earth doped materials will be studied.

### *Outlook:* theoretical studies: how ASAXS distinguishes between structural models

First theoretical calculations show that the SAXS method alone is not able to distinguish between a mono-modal size distribution of core-shell structures and two different distributions of spherical particles. This result is also revealed experimentally in my thesis. The model calculations should be extended to the case of the contrast variation by ASAXS.

## **APPENDIX**

**A.1:** List of samples of composition 13.6Na<sub>2</sub>O-62.9SiO<sub>2</sub>-8.5MnO-15.0Fe<sub>2</sub>O<sub>3-x</sub> (mol %). The highlighted samples were used for the measurements using SAXS and ASAXS.

<b>Serial No.</b>	<b>Sample Name</b>	<b>Thickness (<math>\mu\text{m}</math>)</b>
1	As prepared	210.2 $\pm$ 0.9
2	540°C _180min	160.5 $\pm$ 1.5
3	550°C _5min	184.4 $\pm$ 4.5
4	550°C _10min	177.2 $\pm$ 3.27
5	550°C _20min	142.75 $\pm$ 0.24
6	550°C _40min	144.00 $\pm$ 2.0
7	550°C _60min	123.00 $\pm$ 1.87
8	550°C _120min	132.0 $\pm$ 4.3
9	550°C _180min	138.00 $\pm$ 8.15
11	560°C _20min	171.5 $\pm$ 0.50
12	560°C _40min	163.25 $\pm$ 5.36
13	560°C _60min	118.50 $\pm$ 8.50
14	560°C _120min	170.50 $\pm$ 9.39
15	560°C _180min	130.00 $\pm$ 6.52
16	580°C _20min	157.00 $\pm$ 1.73
17	580°C _40min	172.00 $\pm$ 9.11
18	580°C _60min	170.00 $\pm$ 10.56
19	580°C _180min	128.50 $\pm$ 5.0

**A.2:** List of samples of composition 13.6Na<sub>2</sub>O-62.9SiO<sub>2</sub>-8.5MnO-15.0Fe<sub>2</sub>O<sub>3-x</sub> (mol %). The highlighted samples were used for the measurements using SANS with polarized neutrons.

<b>Serial No.</b>	<b>Sample Name</b>	<b>Thickness (<math>\mu\text{m}</math>)</b>
1	As prepared	827.8 $\pm$ 5.31
2	540°C _180min	2175.2 $\pm$ 15.97
3	550°C _5min	836.2 $\pm$ 4.35
4	550°C _10min	843.6 $\pm$ 4.08
5	550°C _20min	913.0 $\pm$ 8.8
6	550°C _40min	803.8 $\pm$ 8.13
7	550°C _60min	833.4 $\pm$ 10
8	550°C _120min	2173.8 $\pm$ 7.78
9	550°C _180min	861.8 $\pm$ 4.49
11	560°C _20min	2225 $\pm$ 11
12	560°C _40min	2076 $\pm$ 23.26
13	560°C _60min	2106.2 $\pm$ 23.68
14	560°C _120min	887 $\pm$ 2.4
15	560°C _180min	2207.2 $\pm$ 5.6
16	580°C _20min	2172.8 $\pm$ 2.14
17	580°C _40min	2119.6 $\pm$ 9.39
18	580°C _60min	2145.0 $\pm$ 20.15
19	580°C _180min	756.4 $\pm$ 26.3

## REFERENCES

- [1] J.E. Shelby, *Introduction to Glass Science and Technology*, Royal Society of Chemistry, (1997).
- [2] J. Fu, J.M. Parker, P.S. Flower and R.M. Brown, *Eu<sup>2+</sup> ions and CaF<sub>2</sub>-containing transparent glass-ceramics* (2002), *Mater. Res. Bull.* **37**, 1843-1849.
- [3] S. Tanabe, H. Hayashi, T. Hanada and N. Onodera, *Fluorescence properties of Er<sup>3+</sup> ions in glass ceramics containing LaF<sub>3</sub> nanocrystals* (2002), *Opt. Mater.* **19**, 343-349.
- [4] M. Mortier, A. Monteville, G. Partache, G. Maze and F. Auzel, *New progresses in transparent rare-earth doped glass-ceramics* (2001), *Opt. Mater.* **16**, 255-267.
- [5] M.J. Dejneka, *The luminescence and structure of novel transparent oxyfluoride glass-ceramics*, (1998) *J. Non-Cryst. Solids* **239**, 149-155.
- [6] Y. Wang and J. Ohwaki, *New transparent vitroceramics codoped with Er<sup>3+</sup> and Yb<sup>3+</sup> for efficient frequency upconversion* (1993), *Appl. Phys. Lett.* **63**, 3268-3270.
- [7] A. Wiedenmann, *Small-angle neutron scattering investigation of magnetic nanostructure using polarized neutrons* (2000) *J. Appl. Cryst.* **33**, 428-432.
- [8] A. Wiedenmann, A. Hoell and M. Kammel, *Small-angle scattering investigations of cobalt-ferrofluids using polarized neutrons* (2002), *J. Magn. & Magn. Mater.* **252**, 83-85.
- [9] R. Harizanova, G. Völksch and C. Rüssel, *Crystallization and microstructure of glasses in the system Na<sub>2</sub>O/MnO/SiO<sub>2</sub>/Fe<sub>2</sub>O<sub>3</sub>* (2011), *Mater. Res. Bull.* **46**, 81-86.
- [10] C. Bocker, S. Bhattacharya, T. Höche and C. Rüssel, *Size Distribution of Nano Crystallites in Transparent Glass Ceramics* (2009), *Acta. Mater.* **57**, 5956-5963.
- [11] C. Bocker and C. Rüssel, *Self Organized Nano-Crystallisation of BaF<sub>2</sub> from Na<sub>2</sub>O/K<sub>2</sub>O/BaF<sub>2</sub>/Al<sub>2</sub>O<sub>3</sub>/SiO<sub>2</sub> Glasses* (2009), *J. Eur. Ceram. Soc.* **29**, 1221-1225.
- [12] S. Bhattacharyya, C. Bocker, T. Heil, J.R. Jinschek, T. Höche, C. Rüssel and H. Kohl, *Experimental evidence of self-limited growth of Nanocrystals in Glass* (2009), *Nano Lett.* **9**, 2493-2496.
- [13] R. Zallen, *The Physics of Amorphous Solids* (1983), New York: John Wiley.
- [14] N.E. Cusack, *The physics of structurally disordered matter: an introduction* (1987), University of Sussex press.
- [15] S.R. Elliot, *Physics of Amorphous Materials* (1984), Longman group ltd.
- [16] H. Scholze, *Glass – Nature, Structure, and Properties* (1991), Springer.
- [17] C.A. Harper, *Handbook of Ceramics and glass, Technology Seminars, Inc., Lutherville, Maryland* (2001), McGrawHill.
- [18] W.H. Zachariasen, *The atomic arrangements in glass* (1932), *J. Amer. Chem. Soc.* **54**, 3841-3851.
- [19] W. Michael, *Fundamentals of Ceramics* (1996) New York: McGraw-Hill.

- [20] W.D. Kingery, H.K. Bowen, D.R. Uhlmann, *Introduction to Ceramics* (1976), New York: Wiley.
- [21] E. Axinte, *Glasses as engineering materials: A review* (2011), Material and design.
- [22] P. Ball, *Made to Measure: New Materials for the Twenty-First Century* (1997), Princeton, NJ: Princeton University Press.
- [23] L.L. Hench, R.J. Spinter, W.C. Allen, T.K. Greenlee, *Bonding mechanism at the interface of ceramic prosthetic materials*, (1971) *J. Biomed. Mater. Res.* **2**, 117-141.
- [24] L.L. Hench, J. Wilson (Eds.), *An introduction to bioceramics* (1993), World Scientific, Singapore.
- [25] J. Wilson, G.H. Pigott, F.J. Schoen, L.L. Hench, *Toxicology and biocompatibility of Bioglass*. (1981), *J. Biomed. Mater. Res.* **15**, 805-817.
- [26] J.F. Shackelford, *Bioceramics: Applications of Glass and Ceramic Materials in Medicine*. (1998), Zurich: Trans-Tech Publications.
- [27] L.S. Bozadzhiev, G.T. Georgiev and R.L. Bozadzhiev, *A Glass ceramic Material for Fixation of Radioactive Waste* (2011), *Science of Sintering*, **43**, 225-229.
- [28] J.W. Matrin, *Concise Encyclopedia of the Structure of Materials* (2006), Elsevier Science, Oxford UK.
- [29] W.D. Richerson, *Modern Ceramic Engineering: Properties, Processes, and Use in Design*, (1992), 2nd edition, New York.
- [30] D. Marcel, W.D. Richerson, *The Magic of Ceramics* (2000), Westerville, OH: American Ceramic Society.
- [31] E.J. Smoke. *Ceramic compositions having negative linear thermal expansion* (1951), *Journal of the American Ceramic Society*, **34**, 87-90.
- [32] J.A. Savage and S. Nielsen, *Chalcogenide glasses transmitting in the infrared between 1 and 20  $\mu$  - A state of the art review* (1965), *Infrared Phys.* **5**, 195-204.
- [33] C.A. Angell, C. Liu, and H.G.K. Sundar, *Far IR transmitting Halide Glasses* (1985), *Mater. Sci. Forum* **5**, 189.
- [34] Z.J. Zhang, Z.L. Wang, B.C. Chakoumakos and J.S. Yin, *Temperature Dependence of Cation Distribution and Oxidation State in Magnetic Mn-Fe Ferrite Nanocrystals* (1998), *J. Am. Chem. Soc.* **120**, 1800-1804.
- [35] C. Phifer, *Ceramics, Glass Structure and Properties* (2000), Encyclopedia of chemical technology.
- [36] A.K. Varshneya, *Fundamentals of Inorganic Glasses* (1994), Academic Press.
- [37] L. Lichtenstein, C. Büchner, B. Yang, S. Shaikhutdinov, M. Heyde, M. Sierka, R. Włodarczyk, J. Sauer and H.J. Freund, *Die atomare Struktur eines metallgestützten glasartigen dünnen Silikafilms* (2012), *Angewandte Chemie* **124**, 416-420.
- [38] G.H. Beall, *Design and properties of glass-ceramics* (1992), *A. Rev. Mater. Sci.* **22**, 91-119.

- [39] G.H. Beall, *Glass-ceramics: recent development and application* (1993), *Ceramic Transactions Series, Westerville, Ohio: The American Ceramic Society* **30**, 241–266.
- [40] A. Marotta, A. Buri, F. Branda, *Nucleation in glass and differential thermal analysis* (1981), *J. Mater. Sci.* **16**, 341-344.
- [41] W. Höland, V. Rheinberger and M. Schweiger, *Control of nucleation in glass ceramics* (2003), *Phil. Trans. R. Soc. Lond. A* **361**, 575-58.
- [42] M. Volmer and A. Weber, (1926), *Z. Phys. Chem. (Leipzig)* **119**, 227.
- [43] L. Farkas, (1927), *Z. Phys. Chem. (Leipzig)* **125**, 236.
- [44] R. Becker and W. Döring, *Kinetische Behandlung der Keimbildung in übersättigten Dämpfern* (1935), *Ann. Phys.* **24**, 719-752.
- [45] D.C. Creagh, J.H. Hubbell, *International table for crystallography vol C* (1992), 189-206.
- [46] A. Guinier, G. Fournet, *Small Angle Scattering of X-Rays* (1955), Wiley publication.
- [47] O. Glatter, O. Kratky, *Small Angle X-Ray Scattering* (1982), Academic Press.
- [48] L A Feigin and D I Svergun, *Structure analysis by small angle X ray and neutron scattering* (1987) New York Plenum.
- [49] J S Pedersen, *Modeling of small angle scattering data from colloids and polymer systems Neutron, X-ray and Light* (2002) (Amsterdam: Elsevier), p 391.
- [50] J S Pedersen, *Analysis of small- angle scattering data from colloids and polymer solutions: modeling and least -squares fitting* (1997) *Adv. Colloid Interface Sci.* **70**, 171-210.
- [51] M. Kotlarchyk and S.-H. Chen, *Analysis of small angle neutron scattering spectra from polydisperse interacting colloids* (1983) *J. Chem. Phys.* **79**, 2461-2489,
- [52] J.S. Pedersen. *Determination of size distributions from small-angle scattering data for systems with effective hard-sphere interactions.* (1994) *J. Appl. Cryst.* **27**, 595-608.
- [53] J. K. Percus and G. J. Yevick *Analysis of classical statistical mechanics by means of collective coordinates.* (1958) *Phys. Rev.* **110**, 1-13.
- [54] A. Vrij. *Mixtures of hard spheres in the percus-yevick approximation. light scattering at finite angles.* (1979) *J. Chem. Phys.* **71**, 3267-3270.
- [55] C Kittle, *Introduction to solid state physics*, (1966) John Wiley and Sons, New York.
- [56] R W James, *The optical principles of the diffraction of X-rays* (1965) Cornell University Press, Ithaca, New York.
- [57] D.T. Cromer and D. Liberman, *Relativistic Calculation of Anomalous Scattering Factors for X-Rays* (1970), *J. Chem. Phys.* **53**, 1891-1898.
- [58] H.B. Stuhrmann, *Resonance scattering in macromolecular structure research* (1985), *Adv. Polym. Sci.* **67**, 123-163.
- [59] A. Hoell, D. Tatchev, S. Haas, J. Haug and P. Boesecke, *On the determination of partial structure functions in small-angle scattering exemplified by Al<sub>89</sub>Ni<sub>6</sub>La<sub>5</sub> alloy* (2009), *J. App. Cryst.* **42**, 323-325.

- [60] G. Goerigk, K. Huber and R. Schweins, *Probing the extent of the Sr<sup>2+</sup> ion condensation to anionic polyacrylate coils: A quantitative anomalous small-angle x-ray scattering study* (2007) *J. Chem. Phys.* **127**, 154908.
- [61] G. Goerigk, and N. Mattern, *Critical scattering of Ni–Nb–Y metallic glasses probed by quantitative anomalous small-angle X-ray scattering* (2009), *Acta Materialia* **57**, 3652-3661.
- [62] J. Kohlbrecher and I. Bressler, *SASfit, Software package for fitting small-angle scattering curves*. <http://kur.web.psi.ch/sans1/SANSSoft/sasfit.html>
- [63] J. Kohlbrecher, A. Wiedenmann and H. Wollenberger, *Magnetic coupling between the different phases in nanocrystalline Fe-Si-B studied by small angle neutron scattering* (1997), *Z. Phys. B* **104**, 1-4.
- [64] D. Tatchev, A. Hoell, R. Kranold and S. Armyanov, *Size distribution and composition of magnetic precipitate in amorphous Ni-P alloy* (2005), *Physica B* **369**, 8-19.
- [65] A. Hoell, I. Zizak, H. Bieder and L. Mokrani (2006), *DE Patent Specification* 10 2006 029 449.
- [66] K. Binnemans, R.V. Deun, B. Thijs, I. Vanwelkenhuysen and I. Geuens, *Structure and Mesomorphism of Silver Alkanoates* (2004), *Chem. Mater.* **16**, 2021-2027.
- [67] Further more information : <http://www.ill.eu/instruments-support/instruments-groups/instruments/d22/documentation/d22manual>
- [68] C. Dewhurst, <http://www.ill.eu/instruments-support/instruments-groups/groups/lss/grasp/>
- [69] B. Frankel, R.P. Blakemore, R.S. Wolfe, *Magnetite in Freshwater Magnetotactic Bacteria* (1979), *Science* **203**, 1355-1356.
- [70] A.P. Schmidt, *Evidence for the Small Polaron as the Charge Carrier in Glasses Containing Transition Metal Oxides* (1970), *J. Appl. Phys.* **39**, 3140-3149.
- [71] A.E. Owen, and W.E. Spear, *Electronic properties and localised states in amorphous semiconductors* (1976), *Phys. Chem. Glasses* **17**, 174-192.
- [72] M.I. Klinger, *Electrons in low-mobility and disordered semiconductors: theory of transport and related optical phenomena*, (1968), *Rep. Prog. Phys.* **31**, 225-304.
- [73] R.W. Siegel, *Nanostructure materials mind over matter* (1993), *Nanostruc. Mater.* **3**, 1-18.
- [74] J.M.D. Coey, *Whither magnetic materials?* (1999), *J. Magn. Magn. Matter.* **196**, 1-7.
- [75] R.D. Shull and L.H. Bennett, *Nanocomposite magnetic materials* (1992), *Nanostruc. Mater.* **1**, 83-88.
- [76] S. Gupta, R. Ranjit, C. Mitra, P. Raychaudhuri, and R. Pinto, *Enhanced room- temperature magnetoresistance in La<sub>0.7</sub>Sr<sub>0.3</sub>MnO<sub>3</sub>-glass composites* (2001), *Appl. Phys. Lett.* **78**, 362-364.
- [77] Y.-H. Huang, X. Chen, Z.-M. Wang, C.-S. Liao, C.-H. Yan, H.-W. Zhao and B.-G. Shen, *Enhanced magnetoresistance in granular La<sub>2/3</sub>Ca<sub>1/3</sub>MnO<sub>3</sub>/ polymer composites* (2002), *J. Appl. Phys.* **91**, 7733-7735.
- [78] X. Wang, Y. Li, *Monodisperse nanocrystals: general synthesis, assembly, and their applications* (2007), *Chem. Commun.* **28**, 2901-2910.

- [79] H. Si, C. Zhou, H. Wang, S. Lou, S. Li, Z. Du and L.S. Li, *Controlled synthesis of different types iron oxides nanocrystals in paraffin oil* (2008), *Journal of Colloid and Interface Science* **327**, 466–471.
- [80] W. Shi and N. Chopra, *Surfactant-free synthesis of novel copper oxide (CuO) nanowire–cobalt oxide (Co<sub>3</sub>O<sub>4</sub>) nanoparticle heterostructures and their morphological control* (2011), *J. Nanopart. Res.* **13**, 851-868.
- [81] T. Herranz, S. Rojas, M. Ojeda, F.J. Pérez-Alonso, P. Terreros, K. Pirola, and J.L.G. Fierro, *Synthesis, Structural Features, and Reactivity of Fe–Mn Mixed Oxides Prepared by Microemulsion* (2006), *Chem. Mater.* **18**, 2364-2375.
- [82] A. Hoell, A. Wiedenmann, U. Heyenb and D. Schüler, *Nanostructure and field-induced arrangement of magnetosomes studied by SANSPOLE* (2004), *Physica B* **350**, e309-313.
- [83] D. Schüler and E. Baeuerlein, *Iron-limited growth and kinetics of iron uptake in Magnetospirillum gryphiswaldense* (1996), *Arch. Microbiol.* **166**, 301-307.
- [84] K. Grünberg, C. Wawer, B.M. Tebo and D. Schüler, *A Large Gene Cluster Encoding Several Magnetosome Proteins Is Conserved in Different Species of Magnetotactic Bacteria* (2001), *Appl. Environ. Microbiol.* **67**, 4573-4582.
- [85] S. Woltz, R. Hiergeist, P. Görnert and C. Rüssel *Magnetite nanoparticles prepared by the glass crystallization method and their physical properties* (2006), *J. Magn. Magn. Mater.* **298**, 7-13.
- [86] S. Woltz and C. Rüssel, *Self organized nano crystallinity of magnetite precipitated from a 4.9Na<sub>2</sub>O 33.3CaO 17.1Fe<sub>2</sub>O<sub>3</sub> 44.7B<sub>2</sub>O<sub>3</sub> glass* (2004), *J. Non-Cryst. Solids* **337**, 226-231.
- [87] H.J.L. Trap, J.M. Stevels, (1963), *Phys. Chem. Glasses* **4**, 193-205.
- [88] R. Harizanova, G. Völksch and C. Rüssel, *Microstructures Formed During Devitrification of Na<sub>2</sub>O Al<sub>2</sub>O<sub>3</sub> B<sub>2</sub>O<sub>3</sub> SiO<sub>2</sub> Fe<sub>2</sub>O<sub>3</sub>* (2010), *J. Mater. Sci.* **45**, 1350-1353.
- [89] R. Harizanova, R. Keding, G. Völksch and C. Rüssel, *Effect of Thermal History on the Conductivity in the System Na<sub>2</sub>O/CaO/SiO<sub>2</sub>/Fe<sub>2</sub>O<sub>3</sub>* (2008), *Eur. J. Glass Sci. Technol. B* **49**, 177-181.
- [90] G. Völksch, R. Harizanova, C. Rüssel, S. Mitsche and P. Pöhl, *Crystallisation in High Iron Containing Silicate Glasses - Electron Microscopy Investigation* (2004), *Glastech. Ber. Glass Sci. Technol.* **77C**, 438-441.
- [91] S.P. Gubin, Y.A. Koksharov, G.B. Khomutov, G.Y. Yurkov, *Magnetic nanoparticles: preparation, structure and properties* (2005), *Russian Chemical Reviews* **74**, 489-520.
- [92] C.H. Yan, Z.-G. Xu, T. Zhu, Z.-M. Wang, F.-X. Cheng, Y.-H. Huang, and C.S.Liao, *A large low field colossal magnetoresistance in the La<sub>0.7</sub>Sr<sub>0.3</sub>MnO<sub>3</sub> and CoFe<sub>2</sub>O<sub>4</sub> combined system* (2000), *J. Appl. Phys.* **87**, 5588-5590.
- [93] R. Harizanova, I. Gugov, C. Rüssel, D. Tatchev, V.S. Raghuwanshi and A. Hoell, *Crystallization of (Fe, Mn)-based nanoparticles in sodium silicate glasses* (2011), *J. Mater. Sci.* **46**, 7169-7176.

- [94] S. Hass, *Nanochemische Zusammensetzungsanalyse mittels anomaler Röntgenkleinwinkelstreuung (ASAXS): Erbium und Ytterbium dotierte Oxyfluorid-Glaskeramiken* (2010), Humbolt-Universität zu Berlin, Berlin.
- [95] K.L. Sahoo, M. Wollgarten, J. Haug and J. Banhart, *Effect of La on the crystallization behaviour of amorphous  $Al_{94-x}Ni_6La_x$  ( $x=4-7$ ) alloys* (2005), *Acta Materialia* **53**, 3861-3870.
- [96] U. Lembke, A. Hoell, R. Kranold, R. Müller, W. Schüppel, G. Goerigk, R. Gilles and A. Wiedenmann, *Formation of magnetic nanocrystals in a glass ceramic studied by small-angle scattering* (1999), *J. App. Phy.* **85**, 2279-2286.
- [97] J. Haug, H. Kruth, M. Dubiel, H. Hofmeister, S. Haas, D. Tatchev and A. Hoell, *ASAXS study on the formation of core-shell Ag/Au nanoparticles in glasses* (2009), *Nanotechnology* **20**, 505705.
- [98] D. Tatchev, *Multiphase approximation for small-angle scattering* (2010), *J. Appl. Cryst.* **43**, 8-11.
- [99] A. Bota, Z. Varga, *Structural description of the nickel part of a Raney-type catalyst by using Anomalous small angle X ray scattering* (2008), *J. Phys. Chem. C* **112**, 4427-4429.
- [100] R. Würth and C. Rüssel, *The crystallization of (Pb, Yb, Er) $F_x$  nano particles from glasses with the composition  $20 SiO_2 \cdot 13.5 B_2O_3 \cdot 6 Al_2O_3 \cdot 10 PbO \cdot 6.6 CdO \cdot 20 PbF_2 \cdot 13.3 CdF_2 \cdot 10 YbF_3 \cdot 0.5 ErF_3$*  (2011), *Solid State Science* **13**, 1132-1136.
- [101] R. Würth, F. Munoz, M. Müller, and C. Rüssel, *Crystal growth in a multicomponent lithia aluminosilicate glass* (2009), *Mater. Chem. Phys.* **116**, 433-437.
- [102] M. Dittmer, M. Müller, and C. Rüssel, *Self-organized nanocrystallinity in MgO–Al<sub>2</sub>O<sub>3</sub>–SiO<sub>2</sub> glasses with ZrO<sub>2</sub> as nucleating agent* (2010), *Mater. Chem. Phys.* **124**, 1083-1088.
- [103] K. Naito, Y. Benino, T. Fujiwara, and T. Komatsu, *Judd- O felt parameters in Er<sup>3+</sup> in transparent TeO<sub>2</sub>-based nanocrystallized glasses* (2004), *Solid State Communications* **131**, 289-294.
- [104] J.E. Sipe and R.W. Boyd, *Nanocomposite materials for nonlinear optics based on local field effects* (2002), *Topics Applied Physics* **82**, 1-19.
- [105] B.N. Samson, J. Wang, N.F. Borrelli, G.H. Beall, and L.R. Pinckney, *Nickel-doped nanocrystalline glass-ceramic fiber* (2002), *Optics Letters* **27**, 1309-1311.
- [106] P.A. Tick, N.F. Borrelli, L.K. Cornelius, and M.A. Newhouse, *Transparent glass ceramics for 1300nm amplifier applications* (1995), *J. Appl. Phys.* **78**, 6367-6374.
- [107] S. Tanabe, H. Hayashi, T. Hanada and N. Onodera, *Fluorescence properties of Er<sup>3+</sup> ions in glass ceramics containing LaF<sub>3</sub> nanocrystals* (2002), *Opt. Mater.* **19**, 343-349.
- [108] A.C. Yanes, J. Del-Castillo, J. Méndez-Ramos, V.D. Rodríguez, M.E. Torres, J. Arbiol *Luminescence and structural characterization of transparent nanostructured Eu<sup>3+</sup>-doped LaF<sub>3</sub>–SiO<sub>2</sub> glass–ceramics prepared by sol–gel method* (2007), *Opt. Mater.* **29**, 999-1003.
- [109] M.J. Dejneka, *The luminescence and structure of novel transparent oxy fluoride glass-ceramics* (1998), *J. Non-Cryst. Solids* **239**, 149-155.

- 
- [110] A. Biswas, G.S. Maciel, C.S. Friend, P.N. Prasad, *Upconversion properties of a transparent Er<sup>3+</sup>-Yb<sup>3+</sup> co-doped LaF<sub>3</sub>-SiO<sub>2</sub> glass-ceramics prepared by sol-gel method* (2003), *J. Non-Cryst. Solids* **316**, 393-397.
- [111] Z. Hu, Y. Wang, F. Bao, W. Luo, *Crystallization behavior and microstructure investigations on LaF<sub>3</sub> containing oxyfluoride glass ceramics* (2005), *J. Non-Cryst. Solids* **351**, 722-728.
- [112] C. Koch, *Structural nanocrystalline materials - Fundamentals and applications* (2007), Cambridge: Cambridge Univ. Press.
- [113] C. Rüssel, *Nano crystallization of CaF<sub>2</sub> from Na<sub>2</sub>O/K<sub>2</sub>O/CaO/CaF<sub>2</sub>/Al<sub>2</sub>O<sub>3</sub>/SiO<sub>2</sub>* (2005), *Chem. Mater.* **17**, 5843-5857.
- [114] G. Pietzka and P. Ehrlich, *Fluor-Bestimmung mit Destillation als H<sub>2</sub>SiF<sub>6</sub> unter Kreislaufführung des Wassers* (1953), *Angew. Chem.* **65**, 131-135.
- [115] C. Bocker, F. Munoz, A. Duran and C. Rüssel, *Fluorine sites in glasses and transparent glass-ceramics of the system Na<sub>2</sub>O/K<sub>2</sub>O/Al<sub>2</sub>O<sub>3</sub>/SiO<sub>2</sub>/BaF<sub>2</sub>* (2011), *J. Solid State Chem.* **184**, 405-410.
- [116] C.S. Jayanth and P. Nash, *Factors affecting particle-coarsening kinetics and size distribution* (1989), *J. Mater. Sci.* **24**, 3041-3052.
- [117] R.P.F. de Almeida, C. Bocker, C. Rüssel, *Size of CaF<sub>2</sub> Crystals precipitated from Glasses in the Na<sub>2</sub>O/K<sub>2</sub>O/CaO/CaF<sub>2</sub>/Al<sub>2</sub>O<sub>3</sub>/SiO<sub>2</sub> System and Percolation Theory* (2008), *Chem. Mater.* **20**, 5916-5921.
- [118] C. Bocker, I. Avramov and C. Rüssel, *Viscosity and diffusion of barium and fluoride in Na<sub>2</sub>O/K<sub>2</sub>O/Al<sub>2</sub>O<sub>3</sub>/SiO<sub>2</sub>/BaF<sub>2</sub> glasses* (2010), *Chem. Phys.* **369**, 96-100.
- [119] I. Avramov, C. Rüssel, N. Kolkovska and I. Georgiev, *Crystallization kinetics and network rigidity* (2008), *J. Phys. Condens. Matter* **20**, 335203.



## ABBREVIATIONS

<b>ASAXS</b>	Anomalous Small Angle X-ray Scattering
<b>BESSY II</b>	Berliner Elektronen Speichering für Synchrotronstrahlung II
<b>CCD</b>	Charge Coupled Device
<b>ILL</b>	Institute of Laue Langevin
<b>7T-MPW-SAXS</b>	7 Tesla Multipole Wiggler SAXS beamline
<b>MWPC</b>	Multi Wire Proportional Counter
<b>SANS</b>	Small Angle Neutron Scattering
<b>SASREDTOOL</b>	Small Angle Scattering Reduction Tool
<b>SAXS</b>	Small Angle X-ray scattering
<b>TEM</b>	Transmission Electron Microscopy
<b>WAXS</b>	Wide Angle X-ray Scattering
<b>XAFS</b>	X-ray Absorption Fine Structure
<b>XANES</b>	X-ray Absorption Near Edge Structure
<b>XRD</b>	X-ray Diffraction
<b>XRF</b>	X-ray Fluorescence analysis



## PUBLICATIONS

1. **Vikram Singh Raghuwanshi**, Armin Hoell, Christian Bocker, Christian Rüssel: *Experimental evidence of a diffusion barrier around BaF<sub>2</sub> nano crystals in a silicate glass system by ASAXS*: **CrystEngComm** **14** (2012) **5215-5223**.  
*DOI: 10.1039/c2ce06544d*
2. **Vikram Singh Raghuwanshi**, Dragomir Tatchev, Ruzha Harizanova, Sylvio Haas, Armin Hoell, Ivailo Gugov, Christian Rüssel: *Structural analysis of ferromagnetic nanocrystals embedded in silicate glasses by ASAXS*: **Journal of Applied Crystallography** **45** (2012) **644-651**.  
*DOI: 10.1107/S002188981202064X*
3. Ruzha Harizanova, Ivailo Gugov, Christian Rüssel, Dragomir Tatchev, **Vikram Singh Raghuwanshi**, Armin Hoell: *Crystallization of (Fe, Mn) –based nanoparticles in sodium –silicate glasses*: **Journal of Material Science** **46** (2011) **7169-7176**.  
*DOI: 10.1007/s10853-011-5840-x*
4. Ruzha Harizanova **Vikram Singh Raghuwanshi**, Dragomir Tatchev, Ivailo Gugov, Armin Hoell, Christian Rüssel: *Synthesis and Phase composition of Fe/Mn containing Nanocrystals in Glasses from the system Na<sub>2</sub>O/MnO/SiO<sub>2</sub>/Fe<sub>2</sub>O<sub>3</sub>*: **NATO Science for peace and security series B: Physics and Biophysics, Nanotechnological Basis for Advanced Sensors, Part 7** (2011) **249-254**.  
*DOI: 10.1007/978-94-007-0903-4\_28*
5. **Vikram Singh Raghuwanshi**, Sylvio Haas, Dragomir Tatchev, Ruzha Harizanova, Charles Dewhurst, Christian Rüssel, Armin Hoell,: *Structural analysis of ferromagnetic nanocrystals embedded in silicate glasses by SANS (in preparation)*
6. Armin Hoell, Zoltan Varga, **Vikram Singh Raghuwanshi**, Christian Bocker, Christian Rüssel: *Characterization of CaF<sub>2</sub> nanoparticles embedded in silicate glass matrix by ASAXS. (in preparation)*



## ACKNOWLEDGEMENT

I am grateful to all peoples who help me in achieving my PhD work. I am grateful to my supervisor **Prof. Dr. John Banhart** for his encouragement, guidance, and financial support throughout this study.

I would like to express my great appreciation to my advisor **Dr. Armin Hoell**. I wish to thank him for his valuable technical advice and supervision. His observations, comments and incisive reviewing of my thesis helped me to establish the overall direction of the research and to move forward with investigation in depth. I am grateful to him for always being kind and patient with his suggestions and constantly forced me to remain focused on achieving my goal. I also appreciated his open mind and confidence, allowing me to propose and develop my own ideas.

I would like to express my deep sense of gratitude towards **Prof. Dr. Christoph Genzel** for extending me the opportunity and for giving his precious time and continuous guidance to accomplish the present work.

I am heartily thankful to **Dr. Dragomir Tatchev**, for providing advice, guidance and encouragement, particularly during my work and his support from the initial to the final level enabled me to develop an understanding of the subject. I am grateful to him for helping me with the measurements and precious suggestions at crucial junctures during my thesis work.

I am heartily thankful to **Dr. Sylvio Haas**, whose encouragement, guidance and support for the programming skills and helped me in doing the measurements. I am grateful to him for always being kind and providing me valuable advice for improvement of my work.

Additionally, I am grateful to **Dr. Ruzha Harizanova** from Bulgaria and **Dr. Christian Bocker** from Jena for their efforts in preparations of the samples and providing the sample at the time of need. The valuable suggestions that I have received from them were indispensable in the completion of the thesis.

I am heartily thankful to **Dr. Rodrigo Coelho** for helping me adjust to the life of a PhD student in a new environment and atmosphere. The valuable suggestions that I have received from him were indispensable in the completion of the thesis. Sincere thanks to him for his encouraging remarks and positive attitude that always brought me back to a sensible mood during hard times

Appreciation is extended to my colleagues at BESSY for sharing a stimulating and fun environment in which to learn and grow was an unforgettable experience. Particular thanks go to **Dr. Manuela Klaus, Daniel Apel, Diana Thomas, Tillman Fuß, Matthias Meixner,**

***Shrawan and Tirupathai Setti.*** They were always available when I needed advice or just someone to talk to, but most of all, I consider them cherished friends.

Special thanks to ***Klaus Efland*** for supporting me with the instrumentation of the experimental ASAXS setup.

Also I would like to give thanks to the group from HMI (Wannse), mainly ***Manas, Cynthia, Jatin, Amit, and Prashanth*** for providing me the friendly environment. I am grateful to ***Dr. Pankaj & Archana Sagdeo, Ram Janay, Shilpa, Pravin Siwach, Parasmani, Ram prakash, Sanjay, Sunil, Abhijeet, Anupam, Ashim, Kaustav, Tirtha, Swati, Trupti, Zoltan, Karthick, Anil, Manoj*** for their moral support.

I would like to thank to my family supporting me spiritually throughout my life.

## **DECLARATION**

I declare that, except where otherwise stated this PhD dissertation is the result of my own work and includes nothing that is the outcome of others. No part of this dissertation has submitted at Technical University Berlin or any other University for a degree or diploma or other qualifications.

Ich erkläre an Eides Statt, dass die vorliegende Dissertation in allen Teilen von mir selbständig angefertigt wurde und die benutzten Hilfsmittel vollständig angegeben worden sind. Weiter erkläre ich, daß ich nicht schon anderweitig einmal die Promotionsabsicht angemeldet oder ein Promotionsverfahren beantragt habe.

Date: 29.02.2012

Place: Berlin, Germany

(Vikram Singh Raghuwanshi)